Title
Submesoscale Currents on the Continental Shelf

Author
Dauhajre, Daniel Patrick

Publication Date
2019

Peer reviewed|Thesis/dissertation

UNIVERSITY OF CALIFORNIA
Los Angeles

Submesoscale Currents on the Continental Shelf

A dissertation submitted in partial satisfaction
of the requirements for the degree
Doctor of Philosophy in Atmospheric and Oceanic Sciences

by

Daniel Patrick Dauhajre

2019

Abstract of the Dissertation

Submesoscale Currents on the Continental Shelf

by

Daniel Patrick Dauhajre
Doctor of Philosophy in Atmospheric and Oceanic Sciences
University of California, Los Angeles, 2019
Professor James C. McWilliams, Chair

The study of oceanic submesoscale dynamics, currents with spatial-scales of 0.1 - 1 km and time-scales of hours to days, is a rapidly growing branch of physical oceanography due to their prevalence in most regions of the ocean and importance to a growing list of oceanic processes (*e.g.,* setting the stratification of the upper ocean). Previous investigations of submesoscale currents focus primarily in the open-ocean, where the preferred structures of the submesoscale (fronts, filaments, and vortices) exist in the surface boundary layer, well above the sea floor. However, recent, high-resolution regional simulations of the coastal ocean reveal a continental shelf populated with analogous submesoscale coherent structures. The revelation of nearshore submesoscale currents alters historical conceptions of continental shelf circulation that do not predict submesoscale variability in the nearshore.

This dissertation explores the coastal submesoscale regime from multiple perspectives. A phenomenological overview demonstrates that submesoscale fronts, filaments, and vortices are ubiquitous on the shelf, that local bathymetry can control spatial orientation, and that irregular coastal topography can generate submesoscale structures on the shelf. The local circulation of shallow-water fronts and filament is generally consistent with their open-ocean counterparts, defined by strong surface convergence, downwelling, and cyclonic shear that can be described by a diagnostic momentum balance between rotation, pressure gradient force, and vertical eddy diffusion (known as Turbulent Thermal Wind or TTW). Discovery of a previously unknown diurnal

cycle in front or filament circulations (that is not predicted by the TTW balance) further extends understanding of submesoscale currents. Creation and analysis of an idealized model that adds acceleration to the TTW balance allows exploration of this diurnal variability. This idealization elucidates controlling one-dimensional (1-D) Ekman layer dynamics on the diurnal phasing. The isolation of the controlling 1-D mechanism motivates the formulation of a simple 1-D model that can accurately predict the phasing of front and filament circulations around the globe.

Simulation of Lagrangian trajectories in high-resolution coastal simulations reveals that submesoscale currents play an important role in the fate and transport of nearshore material. The ageostrophic secondary circulations of ephemeral shelf fronts and filaments can laterally trap and downwell surface material in less than a day. Failure to represent these currents in a simulation of coastal transport will result in a strongly retentive bias to along-shore transport and an under-representation of vertical transport. The results of this work are applicable to any biophysical study of the coastal ocean that require accurate representation of nearshore material fluxes.

The dissertation of Daniel Patrick Dauhajre is approved.

Kyle C. Cavanaugh

Marcelo Chamecki

Andrew L. Stewart

James C. McWilliams, Committee Chair

University of California, Los Angeles

2019

Table of Contents

List of Figures

List of Tables

Acknowledgments

First, I would like to thank my Ph.D. advisor, James C. McWilliams for giving an opportunity to a curious biomedical engineer who knew next to nothing about physical oceanography or computational fluid dynamics. Above all, Jim has instilled in me an appreciation for the art of scientific storytelling. My growth as a researcher and scientific communicator is overwhelmingly due to his advisement where he has encouraged me to explore independently and perennially scout for new dynamical behaviors, while always providing useful commentary and advice when needed.

I also thank my dissertation committee: Andrew L. Stewart, Marcelo Chamecki, and Kyle C. Cavanaugh for providing insightful commentary on this dissertation and thesis proposal. I would like to thank Andrew for helping me grow my scientific communication skills while I was a Teaching Assistant in his undergraduate course and giving me the opportunity to guest lecture on the California Current System for a separate course.

I want to thank the many researchers and post-docs involved with the ROMS group at UCLA: Yusuke Uchiyama for initial technical advisement; Jeroen Molemaker for extremely useful, constant discussion of this research, and convincing me to make an early switch to Python; Jonathan Gula for initial guidance on ROMS analysis techniques; Alexander Shchepetkin for consistent advisement on ROMS functionality and use as well as guidance on the numerics in Chapter 3; Roy Barkan for discussion of the work in Chapter 3; Kaushik Srinivasan for the parent grid of the SWPAC ROMS solution in Chapter 3 and discussion of the Lagrangian model in Chapter 4; Cigdem Akan for guidance on the setup of the Santa Barbara Channel simulations in Chapters 3 and 4; Faycal Kessouri for the R1km grid in Chapter 4; and Delphine Hypolite for constructive comments on earlier versions of Chapter 4.

Additionally, I want to thank the faculty at USC who offered me undergraduate research opportunities: Myrna Jacobson Meyers, Julien Emile-Geay, and Burton Jones. I would also like to thank Diana McWilliams for helping me with logistical needs through my graduate career and careful

proofreading of all manuscripts and fellowship applications.

I thank all the graduate students in AOS who have made departmental life very enjoyable. I thank Neil Berg and Baird Langenbrunner for perpetual Python discussions. Also, I thank the students who have discussed this research with me or given critical commentary of oral presentations: Wu Sun, Dilhara Ranasinghe, Aviv Solodoch, Julia Hazel, Ken Zhao, Jordyn Moscoso, Yi-Hung Ko, Danny McCoy, and Daniel Clements.

This work is partially supported by the NSF LTER UCSB Graduate Student Fellowship and all computational simulations here benefited from XSEDE Computing at NSF. Chapter 2 is an adapted version of [*Dauhajre et al.*, 2017] and is supported by the NSF (Grant OCE-1355970) and ONR (Grant ONR N00014-14- 1-0626 at UCLA). The work in Chapter 3 is an adapted version of [*Dauhajre and McWilliams*, 2018] and is supported by the ONR (Grant N000141410626) and NSF (Grant OCE-1355970). Finally, Chapter 4 is an adapted version of a recently submitted manuscript [*Dauhajre and McWilliams*, 2019] and is supported by the NOAAA (Grant 0471-2015:04), ONR (Grant N00014-15-1-2645), and NSF (Grant OCE-1355970).

Finally, I thank the immeasurable support of my family. My brother, Abraham, who is an example to look up to as a passionate and determined worker in his own field and has supported me in whatever way I needed in my graduate career. I owe my curiosity about nature to my father, Abraham, who with stories that translated (among other physics) general relativity to a 10 year old, ingrained a scientific outlook in my brother and I from a young age. I owe my dedication to following a passion to my mother, Yasmin, who has always encouraged me to chase the things in life that matter most to me and not to take the easy routes out.

Daniel Patrick Dauhajre

Los Angeles, California, USA

January 2019

Vita

2014	M.S. Atmospheric and Oceanic Sciences, UCLA
2011	B.S. Biomedical Engineering, University of Southern California
2012–2018	Graduate Student Researcher Department of Atmospheric and Oceanic Sciences, UCLA
2015, 2016	Teaching Assistant (Spring Quarters) Department of Atmospheric and Oceanic Sciences, UCLA
2014–2017	Santa Barbara Coastal LTER Graduate Student Fellowship (Summer Quarters)
2014	Brian Bosart Award, UCLA: *for service to students and the department*
2018	Best Student Talk, Eastern Pacific Ocean Conference
2018	Jacob A. Bjerknes Memorial Award, UCLA: *for innovative discoveries of submesoscale currents on continental shelves and superior communication of results*
2014-2016	President, Scientific Outreach Coordinator Chi Epsilon Pi Department of Atmospheric and Oceanic Sciences, UCLA
2018	Climate Committee Leader Surfrider Foundation, Los Angeles Chapter

Publications

Dauhajre, D. P. & McWilliams, J C. (2019), Nearshore Lagrangian Connectivity. (submitted to *J. Geophys. Res: Oceans*).

Bracco, A., Sun, D., Barkan, R., Choi, J., Liu, G., **Dauhajre, D. P.**, Berta, M., Molemkaer, J., McWilliams, J C. & Griffa, A. Diurnal Cycling of Submesoscale Dynamics: Lagrangian Implications in Model Simulations of the Northern Gulf of Mexico. (submitted to *J. Phys. Ocean.*).

Dauhajre, D. P. & McWilliams, J C. (2018), Diurnal Evolution of Submesoscale Front and Filament Circulations. *J. Phys. Ocean.* **48**. 2343–2361, doi:10.1175/JPO-D-18-0143.1.

Dauhajre, D. P., McWilliams, J C., & Uchiyama, Y. (2017), Submesoscale Coherent Structures on the Continental Shelf. *J. Phys. Ocean.* **47**. 2949–2976, doi:10.1175/JPO-D-16-0270.1.

CHAPTER 1

Introduction

Discovery and investigation of oceanic submesoscale dynamics, currents with spatial scales of 0.1 – 1 km, time scales of hours to days, and strong vertical velocities ($O(10^{-3})$ ms^{-1}), has exploded in the last ten to fifteen years [*Thomas et al.*, 2008; *McWilliams*, 2016]. These currents, a hybrid of geostrophic and ageostrophic dynamics, are important to a variety of oceanic processes: they partially fill the spectral gap between the mesoscale and microscale to provide a forward route to energy dissipation [*Barkan et al.*, 2015; *Capet et al.*, 2008a; *D'Asaro et al.*, 2011], influence density stratification in the surface layer [*Boccaletti et al.*, 2006], affect the fate and transport of material in the ocean [*Uchiyama et al.*, 2014; *Gula et al.*, 2014; *Romero et al.*, 2013], and exert control on ecosystem functioning [*Mahadevan*, 2016; *Levy et al.*, 2012]. Previous investigations study these dynamics in mainly open-ocean settings, where submesoscale fronts, filaments, and vortices reside in the weakly stratified surface boundary layer [*Gula et al.*, 2014; *Nagai et al.*, 2006; *Capet et al.*, 2008b], well above the sea floor (overviewed in Chapter 2).

The existence of submesoscale currents on the continental shelf, where boundary layers can be depth-filling, is expected [*Kirincich*, 2016; *Romero et al.*, 2013; *Uchiyama et al.*, 2014; *Capet et al.*, 2008c], but not yet thoroughly investigated. Many introductory questions remain unanswered: frequency of occurrence, formation mechanisms, behavior relative to shallow topography, controlling momentum balance relations in finite depth, and the degree of control on the fate and transport of nearshore material. This dissertation investigates these questions, primarily with the exploration of realistic, high-resolution ($\Delta x \sim O(10 \text{ - } 100 \text{ m})$) coastal ocean simulations ca-

pable of resolving submesoscale dynamics on the shelf. Overall, this work shows the prevalence of submesoscale currents on the shelf and adds this regime to the inventory of continental shelf variability (Chapter 2), extends the understanding of (and predictive capability for) front and filament circulations (Chapter 3), and uncovers the important role of submesoscale currents in the transport of nearshore material (Chapter 4).

Chapter 2 (adapted from *Dauhajre et al.* [2017]) gives a phenomenological overview of submesoscale currents on the shelf in a regional simulation. Historical paradigms for continental shelf dynamics (reviewed in Chapter 2) do not predict a shelf populated with ephemeral submesoscale structures. However, a high-resolution simulation of the Southern California Bight illustrates that submesoscale fronts, filaments, and vortices are ubiquitous in the nearshore. In this chapter, there is demonstration of bathymetric control on the spatial orientation and generation mechanisms of the nearshore submesoscale regime. Local analysis of isolated shelf fronts and filaments tests the applicability of a momentum balance between rotation, pressure gradient, and vertical eddy diffusion (known as the Turbulent Thermal Wind balance, or TTW, [*McWilliams et al.*, 2015]) in describing a local submesoscale circulation. Additionally, quantification of vertical heat fluxes over a front or filament lifecycle allows comparison relative to breaking internal waves on the shelf that are commonly implicated in setting nearshore stratification.

In Chapter 2 there is discovery of a non-trivial diurnal phasing of front and filament circulations that is not predicted by the TTW diagnostic. Chapter 3 (adapted from *Dauhajre and McWilliams* [2018]) investigates this previously unknown diurnal variability with an idealized two-dimensional (2-D) model (named the Transient Turbulent Thermal Wind System). Analysis of the idealized model elucidates the controlling dynamics on the diurnal oscillation of front and filament circulations. This analysis leads to the creation of a simple one-dimensional model that can predict the diurnal phasing of front and filament circulations in various realistic, primitive equation simulations in different geographical locations.

Chapter 4 (adapted from [*Dauhajre and McWilliams*, 2019]) explores the control on the fate and

transport of material transport by submesoscale currents on the shelf. A hierarchy of simulations of the Santa Barbara Channel investigates the differences in coastal connectivity and nearshore transport pathways at different model resolutions. Specifically, the important role of ephemeral shelf fronts and filaments in rapid material transport highlights previously unresolved routes of vertical transport. Finally, Chapter 5 summarizes work to date and presents questions and prospects for future investigations of continental shelf variability.

CHAPTER 2

Submesoscale Coherent Structures on the Continental Shelf

2.1 Introduction

Paradigms for continental shelf dynamics have been developed from observational networks ($\Delta x \sim O(1 \text{ km})$) [*Hickey et al.*, 2003; *Cudaback and Washburn*, 2005; *Lentz and Winant*, 1986; *Dever*, 1996; *Kirincich et al.*, 2009; *Bassin and Washburn*, 2005; *Feddersen et al.*, 1998], numerical simulations [*Ganju et al.*, 2011; *Romero et al.*, 2013; *Uchiyama et al.*, 2014; *Kumar et al.*, 2015, 2016] ($\Delta x \sim [O(10 \text{ m}) - O(1 \text{ km})]$), and idealized models [*Chapman*, 1986, 1987; *Chapman and Lentz*, 2005; *Lentz and Fewings*, 2012; *Austin and Lentz*, 2002; *Tilburg*, 2003]. Recently, downscaling techniques [*Mason et al.*, 2010] applied to coastal regions have led to numerical simulations of the shelf with horizontal resolutions of $O(10 - 100 \text{ m})$ embedded in the regional circulation [*Romero et al.*, 2013; *Uchiyama et al.*, 2014; *Kumar et al.*, 2015, 2016; *Romero et al.*, 2016]. These high-resolution simulations of coastal waters have revealed a dynamically more diverse and heterogeneous shelf than previously known, although the full variability present in these solutions remains incompletely explored. That is, there is more to shelf currents than tides, wind, internal waves, and buoyant coastal currents as well as wave-driven currents (Section 2.2). The newly exposed shelf dynamics are primarily manifested in submesoscale coherent structures (repeatedly arising, preferred $O(0.1 - 10 \text{ km})$ spatial patterns that are immune to swift advective deformation): fronts, filaments, and vortices [*Gula et al.*, 2014; *Capet et al.*, 2008b; *Mahadevan and Tandon*, 2006a; *Nagai et al.*, 2006; *Bracco et al.*, 2016; *Capet et al.*, 2008c]. These motions are a hybrid of geostrophic and

ageostrophic dynamics and are defined by $O(1)$ Rossby ($\mathrm{Ro} = V/fL$) and Froude ($\mathrm{Fr} = V/NH$) numbers , where V represents a horizontal velocity; f the Coriolis parameter; L and H, horizontal and vertical length scales, respectively; and $N = \sqrt{\frac{-g}{\rho}\frac{\partial \rho}{\partial z}}$, the stratification. The occurrence of these phenomena in numerical solutions is a direct consequence of increasing grid resolution to finer than O (1 km) [*Capet et al.*, 2008d]. Observational platforms (*e*.g., boats, planes, gliders) are currently incapable of adequately sampling the three-dimensional evolution of short-lived and seemingly spontaneously formed submesoscale structures over multiple-day life-cycles. At present, high-resolution numerical models provide the richest realizations and the most feasible route for discovery and explanation of submesoscale dynamics in a variety of oceanographic settings.

Analysis and interpretation of submesoscale currents (reviewed in Section 2.3) has primarily been approached in an open-ocean context where submesoscale currents most commonly reside in the surface boundary layer of relatively deep water columns $O(100 - 5000\ \mathrm{m})$. Some evidence of submesoscale phenomena in the nearshore waters on the shelf is the subject of previous work. *DiGiacomo and Holt* [2001], *Bassin and Washburn* [2005], and *Kirincich* [2016] provide observational evidence of submesoscale eddies in the Southern California Bight (SCB) and Martha's Vineyard Shelf, respectively. *Romero et al.* [2013], *Uchiyama et al.* [2014], and *Romero et al.* [2016] show the occurrence of submesoscale activity on the SCB shelf through numerical simulations, and *Capet et al.* [2008c] does so for the Argentinian shelf. These modeling studies are primarily concerned with metrics of material lateral dispersion.

This study investigates the phenomenology of submesoscale variability on the continental shelf with a numerical simulation of the SCB with a resolution of $\Delta x = 75$ m (Section 2.4) that resolves coastal ocean physics deep within the submesoscale range. The numerical realization motivates the following questions: (1) do submesoscale currents exist on the shelf? (2) what are the similarities and differences between open-ocean and shelf submesoscale dynamics? (3) how does the coastal submesoscale regime phenomenologically compare with other shelf dynamics? The existence of submesoscale currents on the shelf is not necessarily surprising given the numerous,

recent studies uncovering processes that drive submesoscale motions (ambient lateral buoyancy gradients, surface mixed layers, and mesoscale straining flows), which exist in some form on the shelf. Thus, a portion of the analysis is analogous to previous work relative to the offshore submesoscale regime [*e.g.*, *Gula et al.*, 2014] that investigates formation mechanisms and dynamical balances of cold filaments as well as the ability of individual submesoscale structures to laterally organize dissolved materials. In addition, however, we analyze the unique features of coastal submesoscale variability: how do the shape of the coastline, vertically overlapping boundary layers, and contact of flow with the bottom influence the distribution, formation, local circulation, and evolution of submesoscale structures on the shelf? Furthermore, we contextualize certain aspects of submesoscale phenomenology with other shelf currents: *e*.g., how do the vertical heat fluxes induced by an individual submesoscale front or filament compare with vertical heat fluxes due to an internal wave? How do the density gradients on the shelf associated with submesoscale currents differ from density gradients due to shelf-break or tidal-mixing fronts? Because submesoscale currents preferentially are manifested in coherent structures, much of the analysis focuses on isolated structures (a single front, filament, or vortex). We supplement the analysis of individual submesoscale structures with statistical metrics to contextualize and strengthen interpretations.

This study is an intersection of two scientific communities: shelf circulation and submesoscale variability (reviewed in Sections 2.2 and 2.3, respectively). The purpose of the study is two-fold: to introduce submesoscale variability to the coastal community and to investigate the degree of control by unique aspects of the shelf (*e*.g., its shallow depth) on submesoscale currents not previously explored in open-ocean studies [*Gula et al.*, 2014; *Capet et al.*, 2008d; *Shcherbina et al.*, 2013]. Our goals are to provide evidence for and to characterize the shallow-water submesoscale regime and highlight its potential importance in contributing horizontal and vertical material fluxes near the coast in the context of the more familiar dynamics of open-ocean submesoscale currents and other types of currents on the continental shelf.

2.2 Background: Types of Shelf Circulation

To provide context for submesoscale processes on the shelf, we give an overview of the common dynamical paradigms for shelf circulation. We restrict our attention to paradigms relevant to the ROMS solutions for the SCB (Section 2.4); these solutions contain no surface gravity waves and lack significant freshwater input from the shoreline.

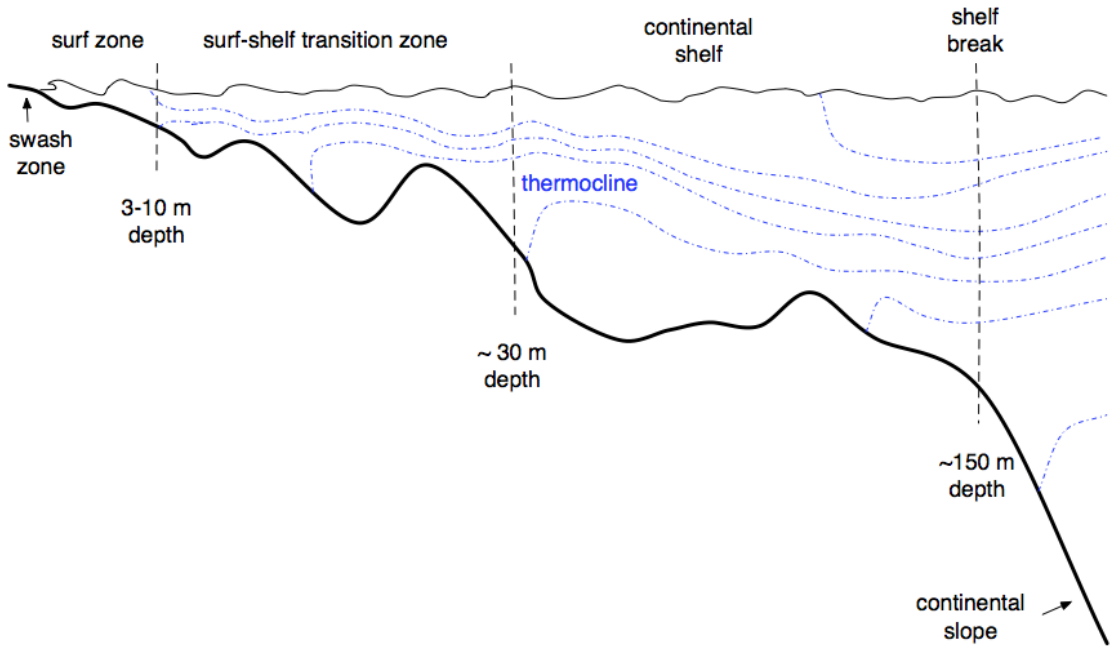

Figure 2.1: An illustration of the cross-shore partitioning of the stratified coastal ocean: Surface waves break and drive littoral currents in the surf-zone that extends seaward to the edge of the surf-shelf transition zone (SSTZ). The SSTZ (the 'inner-shelf' of *Lentz and Fewings* [2012]) is characterized by overlapping surface and bottom boundary layers and extends to the offshore point where surface and bottom boundary layers separate (continental shelf). The continental shelf has surface and bottom boundary layers separated by a stratified interior and extends to the shelf-break. Strong along-slope currents and mesoscale variability are common on the continental slope.

2.2.1 Coastal geography: defining the shelf partitions

Before we overview the types of shelf circulation germane to the SCB shelf, we present a cross-shore partitioning of the coastal ocean to define terms, partly because the terminology varies in previous literature. Our partition of the coastal ocean regions along a cross-shore axis is in Figure 2.1 and its caption. We highlight two regions in Figure 2.1: the surf-shelf-transition-zone (SSTZ) and the continental shelf. The SSTZ (commonly referred to as the 'inner-shelf'[1]) is defined as the region seaward of the surf-zone where surface and bottom boundary layers (SBL and BBL) overlap. The continental shelf intersects the SSTZ where SBL and BBL separate, inshore of the shelf break and continental slope. This study describes submesoscale variability mainly inshore of the shelf break; boundary layer overlap is thus spatio-temporally variable in the domain of interest.

2.2.2 Tidal circulation

The interaction of tidal flows with non-uniform topography can generate residual tidal flow patterns (*e*.g., tidal eddies) that are quasi-permanent dynamical features on a shelf [*Maddock and Pingree*, 1978; *Robinson*, 1981; *Geyer and Signell*, 1990; *Ganju et al.*, 2011]. We note the presence of such tidal eddies in our simulations that qualify as submesoscale in size (briefly discussed in Section 2.5.1 relative to Figure 2.4), however analysis of their dynamics is not necessarily pertinent to this study of more advectively dominated submesoscale structures. *Buijsman et al.* [2012] investigates the internal tide (Section 2.2.4) variability of the SCB with a similar ROMS simulation.

Tides can also be responsible for setting up long-lived lateral density gradients on the shelf, known as tidal-mixing fronts [*Simpson and Hunter*, 1974; *Loder et al.*, 1993; *Hill et al.*, 1993]. These fronts represent a persistent transition zone from vertically mixed to stratified waters on the

[1] The name 'inner-shelf' lacks dynamical specificity hence we choose the name surf-shelf-transition-zone because it is more dynamically relevant.

shelf and result from a competition between vertical mixing induced by the tide and stratification induced by surface heat flux (or river discharge) [*Simpson and Hunter*, 1974]. They have been observed, *e.g.*, on the northwest European shelf [*Simpson and Hunter*, 1974; *Simpson*, 1981] and more recently in the Middle Atlantic Bight [*Loder et al.*, 1993; *Dale et al.*, 2003; *Ullman et al.*, 2003; *Chen et al.*, 2003]. The density gradients associated with these fronts have along-shore geostrophic jets as well as a cross-shore secondary circulations across the density gradient that exhibit surface convergence along the geostrophic jet [*Chen et al.*, 2003].

2.2.3 Wind-driven circulation

Taking the viewpoint of a relatively unstratified shelf, depth-averaged momentum balances [*Lentz and Winant*, 1986; *Lentz and Fewings*, 2012; *Feddersen et al.*, 1998] are frequently used to interpret along-shelf variability. A common yet simple reduction of the along-shore, depth-averaged momentum balance assumes a balance among acceleration, the along-shore pressure gradient, and surface and bottom stresses [*Lentz and Fewings*, 2012]; this reduced momentum balance has been used to describe along-shore current variability in the SCB [*Lentz and Winant*, 1986; *Hickey et al.*, 2003; *Kumar et al.*, 2015]. *Hickey et al.* [2003] in an analysis of an observational network in the SCB draws the conclusion that wind stress (local or remote) drives half of the subtidal velocity variance on the SCB shelf with local winds driving more variance in the spring than summer. Remote wind forcing is primarily thought to locally manifest as poleward propogating coastal trapped waves (CTWs) [*Chapman*, 1987; *Kim et al.*, 2013].

The vertical structure of shelf flows (along- and cross-shelf) has mainly been understood through wind-forced models [*Lentz and Chapman*, 2004; *Tilburg*, 2003; *Austin and Lentz*, 2002; *Federiuk and Allen*, 1996] with stratification playing a large role in dictating the dynamics. Cross-shelf flow is primarily viewed as a two-layer structure with an onshore(offshore) flow at the surface and compensating offshore(onshore) return flow in the bottom (due to the coastal boundary condition of no flow through the boundary). The cross-shelf flow is dictated by the depth of the SBL (partially

a function of stratification) relative to the full depth as well as wind direction (along- or cross-shelf). Along-shelf winds will drive a cross-shelf Ekman flow with the cross-shore extent of the location of maximum cross-shelf convergence dictated by the stratification and wind-direction [*Austin and Lentz*, 2002; *Lentz and Chapman*, 2004]. If the SBL intersects the bottom, and surface gravity wave forcing is weak, cross-shelf winds can drive cross-shelf flow [*Tilburg*, 2003; *Lentz and Fewings*, 2012; *Cudaback and Washburn*, 2005] due to a reduction of the along-shore transport by the bottom stress with a cross-shelf pressure gradient forming to balance the cross-shelf wind-stress.

In the SCB, diurnal band baroclinic motions (with period $T \in [18, 33]$ hrs) can be directly forced by the diurnal sea-land breeze despite being above the critical latitude ($\sim 30°$) necessary for a resonant response to the diurnal wind due to modulation of the "effective" Coriolis parameter by subtidal vorticity [*Federiuk and Allen*, 1996; *Lerczak et al.*, 2001; *Nam and Send*, 2012; *Kumar et al.*, 2016]. The resonant response, characterized by an upward propagation of cross-shelf flow, has been observed [*Nam and Send*, 2012; *Lerczak et al.*, 2001], reproduced in a linear model [*Lerczak et al.*, 2001; *Federiuk and Allen*, 1996], and diagnosed in ROMS [*Kumar et al.*, 2016]. We also see these motions in our ROMS solutions (Section 2.4) but do not show them here.

2.2.4 Internal waves

The propagation of internal waves across the shelf [*Lerczak et al.*, 2003] can be responsible for lateral cross-shelf transport [*Noble et al.*, 2009] and substantial vertical heat flux across the pycnocline [*Shroyer et al.*, 2010] that acts to mix the water column. From a geographical standpoint, internal wave generation sites in the SCB are mainly a function of the magnitude of the slope $|\nabla_h h|$ (Figure 6 in *Buijsman et al.* [2012]) and the barotropic tide. Internal waves are seen in our ROMS solutions, specifically near the Santa Monica Bay shelf break as isotherm undulations co-incident with cross-shore velocity signals emanating from the shelf-break. However, because of the hydrostatic approximation and limited grid resolution, the nearshore ROMS solutions do not contain a full realization of the internal wave regime, specifically with respect to bore formation

and wave-breaking.

2.2.5 Shelf-break fronts

Analogous to submesoscale fronts and filaments, shelf-break fronts are characterized by large horizontal density gradients (that can drive $O(0.1$ m/s) geostrophic velocities) . However, unlike the ephemeral submesoscale shallow-water fronts and filaments shown in this study, shelf-break fronts exist on long-time scales (seasonal/yearly), despite being subject to external perturbations [*Chapman*, 2000]. These cross-shore density gradients are generally thought to form and exist over gently sloped continental shelves, though they can form on steep slopes through interaction with tidal currents [*Chen and Beardsley*, 1995]. They have mainly been studied on the Middle Atlantic Bight shelf [*Chapman and Beardsley*, 1989; *Linder and Gawarkiewicz*, 1998; *Chen and He*, 2009], but are known to exist on other shelves in east Greenland, the east Bering Sea, and the Celtic Sea [*Zhang and Gawarkiewicz*, 2015] and are not expected to be prevalent on the steep SCB shelf.

Chapman and Lentz [1994] (and later *Chapman* 2000) suggest a "frontal-trapping" mechanism to explain the formation and maintenance of shelf-break fronts. An along-shore, coastal current generates offshore transport in the BBL that leads to the formation of a full-depth density gradient due to advection of the fresher water offshore. The front becomes trapped at the depth where the near-bottom geostrophic along-shelf flow changes sign with the result that the BBL Ekman transport converges. [2]

[2] *Chapman* [2000] shows that the frontal trapping depth is actually independent of the shelf-break depth in an idealized setting. *Benthuysen et al.* [2015] investigate the dynamical importance of the shelf-break in light of *Chapman* [2000] results and show that, for an upwelling front, the shelf-break slope induces a weaker cross-shelf transport (relative to the shelf) and can move BBL convergence offshore of the shelf-break.

2.2.6 Ephemeral submesoscale currents

The submesoscale shelf fronts and filaments analyzed in the remainder of this paper are ephemeral (*i*.e., with life-cycles that span several days), are characterized by very high Rossby number Ro (equal to the peak vertical vorticity ζ divided by the Coriolis frequency f), and can be created by ambient mesoscale straining flows and/or interaction with the coastline. In this regard, they represent a different type of lateral density gradient on the shelf relative to the spatially confined, long-lived, lower Ro shelf-break and tidal-mixing fronts discussed above. Further, they are consistently straddling the intersection of the SSTZ and continental shelf (*i*.e., the transverse axis of the features spans regions of boundary layer overlap and boundary layer separation), and often extend even further into deep water. Strong vertical mixing is central to their maintenance and gives rise to substantial vertical structure in their circulation. The local circulation associated with these structures (Section 2.5.5) does not fit any of the dynamical paradigms discussed in this section. Our view is that shallow-water submesoscale currents should be recognized as an important type of shelf variability.

2.3 Background: Submesoscale Dynamics

The submesoscale regime [*McWilliams*, 2016] has recently drawn much attention from the perspective of its role in the turbulent cascade of energy [*Capet et al.*, 2008d; *Barkan et al.*, 2015]; characterization of its coherent structures [*Munk et al.*, 2000; *Mahadevan and Tandon*, 2006a; *Nagai et al.*, 2006; *Gula et al.*, 2014; *McWilliams et al.*, 2015], and influence on density stratification in the surface layer [*Boccaletti et al.*, 2006]; and its potential ecosystem controls [*Mahadevan*, 2016; *Levy et al.*, 2012]. Submesoscale motions fill the spectral gap between the inverse energy cascading quasi-geostrophic mesoscale and forward energy cascading microscale by providing a forward route to energy dissipation through loss of balance [*D'Asaro et al.*, 2011; *Capet et al.*, 2008a; *Barkan et al.*, 2015].

Submesoscale currents consistently reside in the weakly stratified SBL and have the form of 'coherent structures' with preferred spatial patterns of fronts, filaments, and vortices on spatial scales of $L \sim 0.1 - 10$ km and $H \sim 0.01 - 1$ km. Previous studies [*Nagai et al.*, 2006; *Mahadevan and Tandon*, 2006a; *Gula et al.*, 2014; *Capet et al.*, 2008b] show that the individual structures (*e*.g., fronts and filaments) manifested on the submesoscale consist of a mixture of geostrophic and ageostrophic dynamics characterized by high Rossby number ($\mathrm{Ro} = \zeta/f >> 1$), strong vertical velocity ($w \sim O(10^{-3}$ ms$^{-1})$, and large horizontal buoyancy gradients ($O(10^{-4}$ kgm$^{-4})$). A dynamical signature of submesoscale structures in the surface layer are lines and curves of strong, cyclonic surface vorticity (indicative of longitudinal (along-front) geostrophic flow set up by a transverse (cross-front) buoyancy gradient) and surface convergence (indicative of an ageostrophic transverse secondary circulation that produces large, downwelling vertical velocity).

Three mechanisms are commonly invoked to describe the formation of submesoscale coherent structures: generation of "mixed layer eddies" by a form of baroclinic instability in surface mixed layer that can exhibit an unstable linear mode with a horizontal length scale of the mixed layer deformation radius $l \sim Nh_{sbl}/f \sim O(1$ km) due to the weak stratification ($N \sim 10^{-3}$ s^{-1}) and shallow depth ($h_{sbl} \sim 100$ m) [*Boccaletti et al.*, 2006; *Callies et al.*, 2016]; frontogenesis (rapid sharpening of buoyancy or velocity gradients) by a favorably aligned deformation flow that elongates a buoyancy gradient by strain [*Hoskins*, 1982; *McWilliams et al.*, 2009a,b; *Shakespeare and Taylor*, 2013]; and frontogenesis in a turbulent boundary layer by a mixing-induced transverse secondary circulation that rapidly sharpens existing gradients by advection [*McWilliams et al.*, 2015]. A coherent structure can rapidly form, maintain its shape for hours to days while being advected by larger-scale flows fields, and ultimately be destroyed by its own instabilities (or parameterized diffusion) or by shredding from other strong flows [*Gula et al.*, 2014; *McWilliams*, 2016]. Submesoscale fronts, filaments, and vortices are dynamically distinct ($\mathrm{Ro} >> 1$) and relatively ephemeral (O(hours − days)) compared to geostrophically balanced ($\mathrm{Ro} << 1$) mesoscale eddies that often exist for O(weeks).

A steady-state approximate momentum balance combining geostrophic, Ekman, and hydrostatic dynamics has been used to diagnose and describe front and filament circulation [*Gula et al.*, 2014; *McWilliams et al.*, 2015; *Wenegrat and McPhaden*, 2016a]. The balance, referred to as Turbulent Thermal Wind (TTW), is applied under the assumption that the spatial configurations are quasi-steady (*i*.e., fronts and filaments after generation and precluding destruction) and thus lacks time-tendency and advection terms. The TTW balance in horizontal momentum is given by

$$f\hat{\boldsymbol{z}} \times \boldsymbol{u}_h = -\nabla_h \phi + \frac{\partial}{\partial z}\left(\kappa_v \frac{\partial \boldsymbol{u}_h}{\partial z}\right), \tag{2.1}$$

where the x-axis is the longitudinal (along-front/filament) axis and the y-axis is the transverse (cross-front/filament) axis. The horizontal velocity vector is $\boldsymbol{u}_h = u\hat{i} + v\hat{j}$, ϕ is the pressure normalized by a reference density ($\phi = p/\rho_0$), and κ_v is the vertical eddy viscosity coefficient (usually associated with boundary layer turbulence and modeled by a vertical mixing parameterization in ROMS discussed in Section 2.4). With hydrostatic vertical momentum balance, ($\partial\phi/\partial z = -g\rho/\rho_0$), knowledge of the density structure and turbulence in the boundary layer ($\kappa_v(y, z)$) can be used to obtain a diagnostic estimate of the submesoscale coherent structure circulation by (2.1).

The TTW diagnostic balance when applied to ROMS solutions in *Gula et al.* [2014] has proven the more successful (relative to other diagnostics [*Garrett and Loder*, 1981; *Nagai et al.*, 2006]) in diagnosing the ageostrophic secondary circulations associated with submesoscale fronts and filaments. Equation (2.1) gives a scaling estimate for the strength of the transverse overturning streamfunction, [*McWilliams*, 2017]:

$$\Phi \sim \frac{\kappa_v \nabla_h b}{f^2}, \tag{2.2}$$

where the buoyancy $b = -g\rho/\rho_0$, where ρ is the density. Equation (2.2) states that the presence of a strong buoyancy gradient and a turbulent boundary layer are necessary to produce an ageostrophic overturning cell in the transverse plane. The neglect of an acceleration term in (2.1) is made with the assumption that mid-lifecycle submesoscale fronts or filaments will undergo relatively slow changes in κ_v or $\nabla_h b$ and that acceleration and advection are relatively small. We investigate the validity of the TTW balance for shelf fronts and filaments in Section 2.5.5.

The strong restratification flux [*Boccaletti et al.*, 2006] induced by submesoscale vertical velocities has been invoked as a mechanism that can aid phytoplankton growth by trapping nutrients in a newly stratified euphotic zone [*Mahadevan*, 2016; *Levy et al.*, 2012], and the secondary circulations can scour nutrients from below the boundary layer. Horizontal heterogeneity of submesoscale coherent structures at the surface can thus impart structure onto signals of primary productivity and partially control ecosystem functioning.

Finite-depth influences on submesoscale currents are unexplored because most of the literature is focused on the open-ocean regime. Submesoscale currents on the shelf are often influenced by local bathymetry. Contact with the sea floor has the potential to influence local front or filament circulation due to bottom drag and vertical mixing in the BBL. The mesoscale activity contributing to the ambient straining fields commonly implicated in the formation of open-ocean submesoscale coherent structures (*e.g.*, the deformation flow mechanism of *Hoskins* [1982]) may be dampened on shelves that are narrower and shallower than a typical mesoscale eddy size; however, the instability and mixing-induced frontogenesis formation mechanisms are still available there.

2.4 Simulation Set-up

The model used is the Regional Oceanic Modeling System (ROMS; *Shchepetkin and McWilliams* [2005]). The model solves the hydrostatic Primitive Equations and uses a K-Profile Parameterization (KPP; *Large et al.* [1994]) for vertical mixing. The 3D circulation of Santa Monica and San Pedro Bays (Figure 2.2b) is simulated with $\Delta x = 75$ m horizontal resolution. This fine resolution is achieved through a one-way grid nesting technique [*Mason et al.*, 2010]. The details of the computational time periods, grid-resolution, boundary conditions, atmospheric and tidal forcing are summarized in Table 2.1. The nesting hierarchy is as follows: an outer domain of $\Delta x = 5$ km (L0) for the entire U.S. West Coast, $\Delta x = 1$ km for the SCB (L1), $\Delta x = 250$ m (L2) for central area of the

Bight, and $\Delta x = 75$ m (L3) encompassing Santa Monica and San Pedro Bays. The L2 and L3 nests are shown in Figure 2.2a, and the L3 domain is shown in Figure 2.2b. The L3 nest is atmospherically forced (winds, surface heat, and freshwater fluxes) by a 6 km Weather Research and Forecast Model (WRF; *Michalakes et al.* [1998]) simulation within the NCEP North American Regional Reanalysis (32 km resolution). The TPXO 7.1 global tidal prediction model [*Egbert et al.*, 1994] provides the tidal amplitude and phases for ten tidal constituents (M_2, S_2, N_2, K_2, K_1, O_1, P_1, M_f, and M_m) that are used in the forcing of the L1 solution at the side boundaries. The tidal variability in L1 is passed onto L2 through the lateral boundary condition, which serves as the boundary condition for the L3 solution. More specific details of the nesting procedure for the L3 solutions can be found in *Uchiyama et al.* [2014] and *Romero et al.* [2013].

Table 2.1: Configuration of ROMS nest for the SCB

	L0	L1	L2	L3
computational period	01/2007-12/2008	10/2007-04/2008	11/2007 - 04/2008	12/2007 - 04/2008
horizontal resolution	5 km	1 km	250 m	75 m
vertical levels	40	40	40	32
boundary conditions	SODA (5-day)	L0(daily)	L1(2-hourly)	L2(2-hourly)
barotropic tide	-	TPXO7.1	-	-
wind forcing	WRF(18 km)	WRF(6 km)	WRF(6 km)	WRF(6 km)

Various regions within the L3 domain that are later referred to are labeled in Figure 2.2b. Specifically, we refer to Santa Monica Bay and San Pedro Bay as SMB and SPB, respectively. The L3 hindcast spans December 1, 2007 - April 29, 2008. The majority of the analysis presented is based on 2-hour averaged output of the L3 solutions. There are two analyses that utilize higher-frequency output. The first is the analysis of Filament1 in Section 2.5.3 based on 30 min. averaged output of L3 solutions, and the second is the 15 min. snapshots for offline Lagrangian particle simulations in Section 2.5.7.

Numerical simulations begin to resolve submesoscale coherent structures (fronts, filaments, vortices) with horizontal grid resolutions of about 1 km [*Capet et al.*, 2008d; *Gula et al.*, 2014; *Romero*

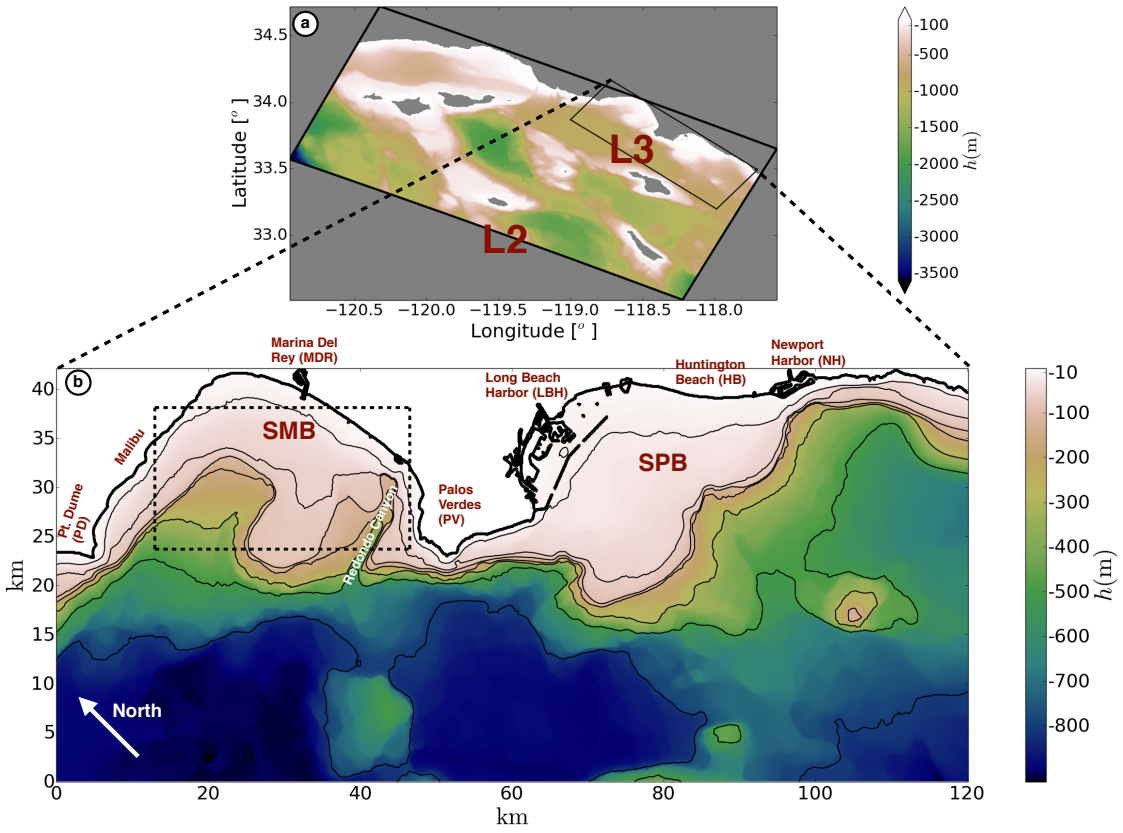

Figure 2.2: (a): L2 and L3 ROMS nests with bathymetry contoured. (b): L3 domain. Santa Monica Bay (SMB) and San Pedro Bay (SPB) are indicated as well as various along-coast locations to orient the reader. The dashed, black box in SMB is used for the analysis in Section 2.5.5 (Figure 2.12).

et al., 2013; *Uchiyama et al.*, 2014]. Surface velocity data from high-frequency radar has been used to hint at the existence of submesoscale eddies on the shelf [*Bassin and Washburn*, 2005]; however, the resolution provided by the radars ($\Delta x \sim 2$ km) is not necessarily fine enough to capture the full regime (nor sample the vertical structure). High-resolution surface images (*e.g.*, SST, color, SAR) have provided the most extensive validations of the simulated submesoscale patterns [*Munk et al.*, 2000; *DiGiacomo and Holt*, 2001; *D'Asaro et al.*, 2011; *McWilliams*, 2016]. The BBL exerts a degree of control on the shallow-water dynamics in the L3 solution. Submesoscale structures on the shelf span the full $\sim 10 - 100$ m water column and may be in contact with the bottom. The bottom stress in the L3 solution is computed as a bottom-layer quadratic drag law,

$$\boldsymbol{\tau}^b = \frac{\rho_0 k^2 |\boldsymbol{u}_b| \boldsymbol{u}_b}{\ln(z_b/z_0)^2}\,, \tag{2.3}$$

where $\boldsymbol{u}_b$ is the velocity vector of the lowest sigma level; $k = 0.41$ is von Karman's constant, z_b is the height above the bottom (mid-point of the bottom grid cell), and z_0 is a roughness length (10^{-2} m).

The BBL thickness (h_{bbl}) and its associated vertical mixing in the L3 solution is parameterized with KPP. The BBL KPP scheme is analogous to the SBL scheme that determines the boundary layer depth (h_{sbl} or h_{bbl}) based on turbulent shear, stratification, and rotation [*Durski et al.*, 2004; *McWilliams et al.*, 2009c; *Lemarie et al.*, 2012]; the vertical mixing is then determined from the boundary layer depth, a non-dimensional shape function that matches the interior mixing to vertical edges of the boundary layer, and a turbulent velocity scale [*Large et al.*, 1994]. While open questions remain on the skill KPP has relative to rapidly changing time-scales (O(minutes)) and its lack of dependency on horizontal gradients, *McWilliams et al.* [2009c] and *Durski et al.* [2004] find that KPP is suitable for diurnal forcing and coastal application, respectively.

Submesoscale motions may potentially exhibit non-hydrostatic effects in the real-ocean and our solutions lack internal wave breaking on the shelf. However, our solutions are somewhat slowly evolving and scale anisotropic ($H/L << 1$, where H and L are vertical and horizontal length scales, respectively) and we do not expect non-hydrostatic effects to be important to the submesoscale structures we investigate. *Mahadevan and Tandon* [2006b] provides a direct comparison of hydrostatic and non-hydrostatic submesoscale realizations. The study was unable to find categorical differences between the realizations, however, the comparison is made up to a resolution of $\Delta x = 250$ m. Important non-hydrostatic processes may arise at higher resolution, though this remains an open question. While non-hydrostatic effects may have some relevance in the $\Delta x = 75$ m L3 domain, the scope of our study does not include processes where non-hydrostatic effects cause the largest differences (*e*.g., evolution of baroclinic instability generating submesoscale features or internal wave breaking).

This study focuses on submesoscale structures that arise on or near the continental shelf of the L3 domain. The $\Delta x = 75$ m grid in the L3 solution (Figure 2.2b) resolves the O (0.3 − 30 km)

spatial scales of submesoscale coherent structures as well as detailed features of the coastline that influence nearshore circulation. In *Kumar et al.* [2015] these L3 solutions are used as the boundary conditions for a slightly finer grid (HB06 L4 with $\Delta x = 50$ m), whose solutions are compared to mid- to inner-shelf observations off Huntington Beach. That validation study shows that the nearshore ROMS solutions well simulate subtidal dynamics on the shelf, so we do not do further model validation here.

2.5 Submesoscale Coherent Structures on the Shelf

A portion of the analysis in this section will focus on individual shelf fronts and filaments. We provide a summary of the names, locations, times, and relevant figures pertaining to these features in Table 2.2 to orient the reader. First we present a realization of the submesoscale regime on the shelf with a picture of a 2-hour average to motivate the rest of the study. Figure 2.3 illustrates the abundance of ephemeral submesoscale coherent structures on the shelf in the ROMS simulation of Santa Monica and San Pedro Bays. [3]

Spatially heterogeneous coherent structures are evident inshore of and extending past the shelf-break (roughly coincident with the 110 m isobath) as straight lines, curves, and spirals of strong cyclonic relative vorticity. The large, cyclonic ($\zeta / f >> 1$) associated with these structures, their non-uniform instantaneous spatial distribution, and corresponding advective evolution (seen in the SI animation) identify these currents as submesoscale and differentiate them from lower Ro, spatially-fixed tidal-mixing and shelf-break fronts. Coincident with these vorticity structures are surface convergence structures (Figure 2.3c) as well as large surface buoyancy gradients (Figure 2.3b,d). By continuity, the strong surface convergence indicates strong downwelling. The surface convergence and associated downwelling is a signature of the ageostrophic secondary circulations of these features (Section 2.5.5). The buoyancy gradients can be classified as fronts (trans-

[3] An animation is available (https://youtu.be/STJ4PMKUj5g) to provide the reader visual evidence of the ubiquity of these features.

Table 2.2: Isolated submesoscale features analyzed in the study. Indicated in the table are the name, the type of buoyancy structure (front or filament), the general location (see Figure 2.2), the date(s), time(s) (PST hour) of feature analysis, and the figures corresponding to each feature. For Filament1, Filament2, Filament4, and Front2 the analysis spans multiple days, so “multiple" is listed for the Time(s) column, with exact hours given in the text and figures as needed.

Name	Structure	Location	Date(s)	Time(s)	Figure(s)
Filament1	filament	SPB	12/31/2007 - 1/1/2008	multiple	2.6
Filament2	filament	SMB	2/3/2008 - 2/6/2008	multiple	2.7
Filament3	filament	SMB	12/14/2007	03:00	2.8, 2.9
Filament4	filament	SMB	1/3/2008 - 1/5/2008	multiple	2.8, 2.11,2.13
Front1	front	SPB	3/21/2008	04:00, 10:00	2.8, 2.10
Front2	front	SPB	12/13/2007 - 12/15/2007	multiple	2.3, 2.13

verse steps in buoyancy) or filaments (transverse extrema in buoyancy). Dense (cold) filaments are more prevalent than light (warm) filaments due to the direction and effect of the secondary circulation on maintaining the surface buoyancy gradient: the secondary circulation of a cold filament acts to strengthen the surface buoyancy gradient with convergence and downwelling at its center, whereas the secondary circulation associated with a warm filament inhibits strengthening of the surface buoyancy gradient with divergence and upwelling at its center [*McWilliams et al.*, 2009a].

We highlight three diverse types of structures indicated by the boxed regions in Figure 2.3b (from left to right): dense-core vortices with cross-shore extending filaments, a mid-shelf front that runs roughly parallel to local bathymetry (referred to as Front2, Table 2.2), and a cross-isobath oriented dense filament connected to a “fork" of two fronts intersecting the shoreline. All of the isolated features (in Figure 2.3 and in the rest of the study) are identified as submesoscale structures by their strong cyclonic vorticity, strong surface convergence and associated downwelling, extreme lateral buoyancy gradients, and an O(hours – days) life cycle; the advective evolution of the submesoscale coherent structures distinguishes them from inertia-gravity waves emitted

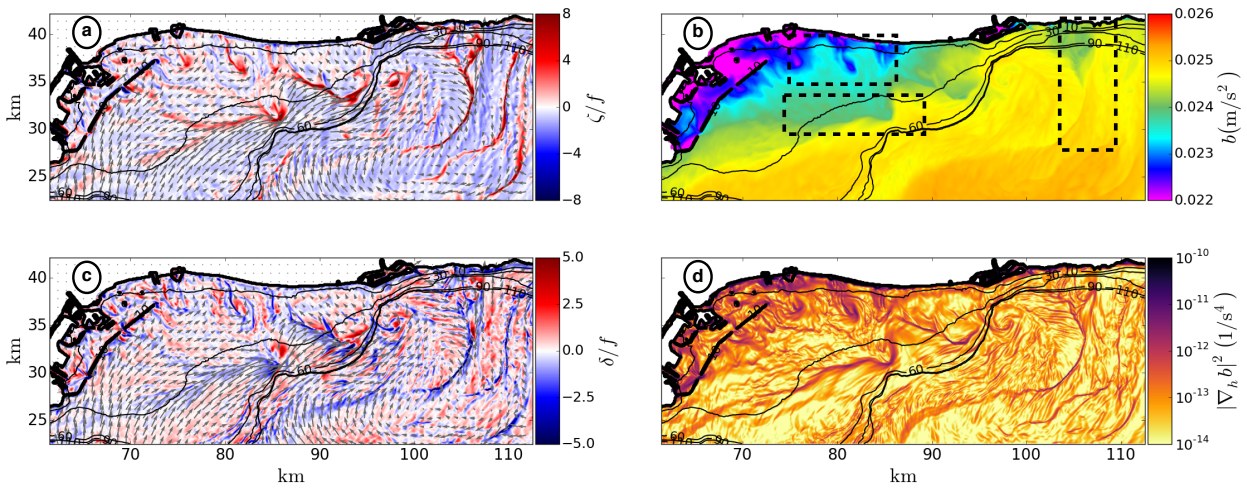

Figure 2.3: 2-hour average of surface fields in San Pedro Bay on Dec. 14, 2007 13:00 PST from the L3 ROMS simulation. (a): surface relative vorticity normalized by the Coriolis frequency (colors) and surface horizontal velocity vectors (arrows). (b): surface buoyancy ($b = -g\rho/\rho_0$). (c): surface divergence normalized by the Coriolis frequency (colors) and surface horizontal velocity vectors (arrows). (d) surface horizontal buoyancy gradient magnitude (squared) (log color-scale). Solid black lines indicate bathymetry. Dashed boxes in (b) highlight certain features discussed in the text. Specifically, the mid-shelf front running parallel to the shoreline is referred to as Front2 in Section 2.5.6

in the L3 solution that also exhibit large relative vorticity and divergence values.

The particular 2-hour averaged realization in Figure 2.3 shows a somewhat isotropic orientation of the fronts and filaments whose longitudinal axis can be either parallel and perpendicular to isobaths. In the subsequent Section 2.5.2, we show that there is a preference of orientation of fronts and filaments relative to isobaths; a preference that is more strongly expressed closer to shore.

2.5.1 Regional heterogeneity

We investigate the regional distribution of submesoscale activity by analyzing metrics for submesoscale-indicating fields at the surface: relative vorticity ($\zeta = \frac{\partial v}{\partial x} - \frac{\partial u}{\partial y}$) and divergence ($\delta = \frac{\partial u}{\partial x} + \frac{\partial v}{\partial y}$). Strong signals in any of the latter variables are indicative of submesoscale coherent structures (fronts, filaments, vortices) (Figure 2.3). Specifically, metrics that reveal imprints of strong cyclonic surface vorticity and surface convergence are indicative of the more persistent downwelling fronts and filaments.

Spatial heterogeneity (primarily through topographic control) is revealed in the variance maps for both fields ($\zeta/f, \delta/f$) in Figure 2.4a,b. The strongest variance (most strikingly for ζ/f) is at the headlands and inside of Long Beach Harbor due to vortical wakes generated by flow through the breakwaters. On the shelf, there is a clear tendency for submesoscale variance to trace isobaths, with most of the activity occurring in between the 20 and 100 m isobaths. The tendency of vorticity variance to follow isobaths is broken in Redondo Canyon in SMB (Figure 2.2b) where a roughly cross-shore signal extends from the shelf all the way offshore; potentially a pathway for strong vorticity structures to exit the SMB shelf. Relative to offshore regions, the shelf clearly has stronger variance and spatial heterogeneity. However, a relatively quiet nearshore region does exist on the broad SPB shelf, just southeast of Long Beach Harbor and near Marina Del Rey on the SMB shelf.

Skewness maps for vorticity and divergence (Figure 2.4c,d) show the spatial distribution of the the asymmetry of the PDFs for ζ/f or δ/f calculated at each grid-cell for all time-points (1,812 samples). A positive ζ/f (δ/f) skewness value indicates a preference for cyclonic (divergent) motion and vice versa. The spatial distribution of skewness in the domain is made up of many near-grid scale bands of large skewness magnitude. Our interpretation is that these bands indicate the repeated passage of multiple like-signed, high-magnitude vorticity (*e*.g., $\zeta/f >> 1$) and divergence (*e*.g., $\delta/f << -1$) structures over neighboring grid-cells. Offshore of the shelf-break, these patterns are rather isotropic in orientation and nearshore there is more evidence of

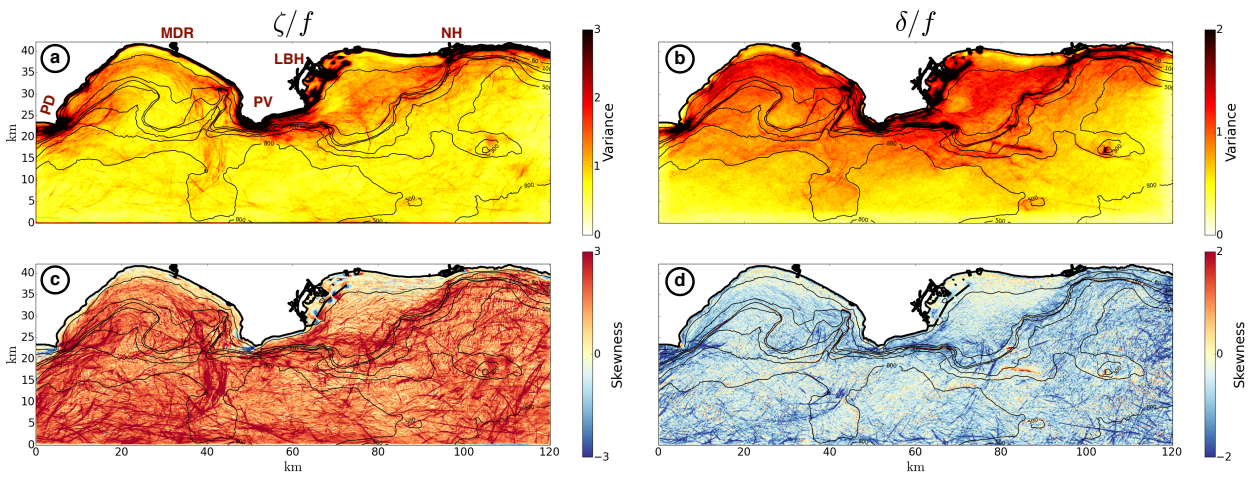

Figure 2.4: Variance (top row) and skewness (bottom row) for surface relative vorticity (left) and divergence (right) normalized by the Coriolis parameter (f). Variance and skewness are calculated at each grid cell from 151 days of velocity output averaged at 2 hour intervals (1812 total time points). Solid black lines indicate bathymetry. The variance color bar is over-saturated near the shoreline. Marina Del Rey (MDR), Long Beach Harbor (LBH), Newport Harbor (NH), and the Point Dume (PD) and Palos Verdes (PV) headlands are denoted in (a) to orient the reader.

topographic control. Overall, the maps show a cyclonic (positive ζ/f skewness) and convergent (negative δ/f skewness) preference at the surface as expected from the standard view of fronts and filaments [*McWilliams*, 2016].

Negative vorticity skewness is present on the northwestern side of each headland (Palos Verdes and Point Dume). The anticyclonic vorticity generation at these headlands is most likely due to the mean along-shore current located offshore (counter to the equatorward California Current) that generally advects warm water to the north and west along the coast in the SCB. Also, the harbors on the shoreline exhibit cyclonic and anticyclonic vorticity generation (most strikingly at Long Beach Harbor in the gaps of the breakwater), partly due to tidal vorticity generation. The positive vorticity skewness on the SPB shelf is diminished near the shoreline (roughly shoreward of the 20 m isobath), and there is non-negligible anticyclonic skewness in that region potentially related to the generation of anticyclonic structures in Long Beach and Newport Harbors. Apart from the nearshore topographic influences on the skewness maps of vorticity and divergence, the

spatial distribution of skewness in the regions offshore of the shelf-break exhibit a collage of near-grid scale cyclonic (Figure 2.4c, red shading) or convergent (Figure 2.4d, blue shading) bands or zones. An exception to this offshore isotropy is the Redondo Canyon streaks that extend offshore from the shelf (Figure 2.4c). *Shcherbina et al.* [2013] gives observational evidence of the cyclonic, convergent skewness in submesoscale resolving measurements of open-ocean surface currents, but the interpretations of spatial distribution given in Figure 2.4c,d have not been applied to an open-ocean setting.

Buijsman et al. [2012] show that there is an active internal wave field in the SCB, and we expect such activity in the L3 solution. Internal waves can provide a source of large vorticity and divergence in the L3 solution and may dilute the signals in Figure 2.4 interpreted as indicative of submesoscale dynamics. However, the SI animation of the surface flow fields shows a dominance of the largest vorticity and divergence signals under advective evolution (*i*.e., submesoscale coherent structures) while capturing tidal variability (a primary driver of internal wave generation); the metrics of Figure 2.4 are obtained from 2-hour averaged surface fields and will predominantly capture these advectively dominated surface dynamics with some, but not overwhelming, dilution by the internal wave field, which will be more expressed in the interior.

2.5.2 Spatial orientation of fronts and filaments

The variance maps in Figure 2.4a,b indicate a shallow-water preference for high vorticity variance to align parallel to isobaths (most strongly in SMB). We investigate this cross-shelf preference of submesoscale structures further by examining the angle of extreme density gradients (strongly indicative of strong fronts and filaments) relative to depth (indicating cross-shore location). Probability Density Functions (PDFs) of surface density gradient vector magnitude ($|\nabla_h \rho|$) and angle $\left(\theta_{\nabla_h \rho}\right)$ are calculated for all 151 days of simulation (1,812 temporal data points) and organized relative to the bottom depth of the sampling location. PDFs are obtained from 300 (x, y) sampling locations along a specific isobath. The sampling locations are chosen to span the longest

along-shore contour of an isobath; that is, sampling locations are not placed on small closed contour areas (*e*.g., a seamount). We use 90 isobaths in our analysis spanning $h \in [10, 900]$ m at 10 m intervals.

The density gradient vectors are rotated into a local coordinate frame relative to the bathymetric gradient (analogous to the coordinate transformation in *Romero et al.* [2013]). The transformation is made such that the cross-shelf axis (x') is parallel to the bathymetric gradient and the along-shelf axis (y') is oriented 90° counterclockwise to the cross-shelf axis. Using the bathymetric unit gradient vector $\boldsymbol{h}_g = \nabla h/|\nabla h| = \hat{h_x} + i\hat{h_y}$, the density gradient vector is decomposed into along- and cross-shelf components:

$$\begin{aligned} \frac{\partial \rho}{\partial x'} &= \frac{\partial \rho}{\partial x}\hat{h_x} + \frac{\partial \rho}{\partial y}\hat{h_y} \\ \frac{\partial \rho}{\partial y'} &= \frac{\partial \rho}{\partial y}\hat{h_x} - \frac{\partial \rho}{\partial x}\hat{h_y}\,, \end{aligned} \tag{2.4}$$

where x and y represent the horizontal geographical axes of the model domain in Figure 2.2b. The direction of the density gradient relative to bathymetric gradient is given by

$$\theta_{\nabla_h \rho} = \tan^{-1}\left[\frac{\partial \rho/\partial y'}{\partial \rho/\partial x'}\right]. \tag{2.5}$$

$\theta_{\nabla_h \rho} = -\pi, 0, \pi$ translates to a density gradient pointing across isobaths, with $\theta_{\nabla_h \rho} = 0$ implying a density gradient pointing in the same direction as the bathymetric gradient (i.e, offshore).

Figure 2.5a shows the PDF of density gradient magnitude at each isobath. There is a clear difference in the breadth of the PDFs for shallow and deep water. In shallower-water ($10 - 100$ m), PDFs of $|\nabla_h \rho|$ are broader relative to the PDFs in deeper water (> 100 m). This dependency in PDF shape as a function of depth implies that there are stronger density gradients in the nearshore, potentially due to the combination of the weaker stratification and stronger velocity gradients (*i*.e., stronger ζ/f, δ/f variance in the nearshore in Figure 2.4a,b).

Figure 2.5b shows the PDFs of the orientation angle $\left(\theta_{\nabla_h \rho}\right)$ for each isobath. We isolate the front and filament density gradients (*i*.e., strongest gradient magnitudes) by conditionally sampling

the gradient vectors that exceed 5 times the RMS of the density gradient magnitude relative to data points along each isobath; the curves in Figure 2.5b give a metric of preferred alignment of surface fronts and filaments relative to depth. Analogous to the strength of $|\nabla_h \rho|$, there is a clear dichotomy in preferred horizontal orientation between the shallow and deep regimes. Strong density gradients in shallow-water preferentially point across-isobaths directed towards deeper water $\left(\theta_{\nabla_h \rho} = 0\right)$. This implies a front or filament that has its longitudinal axis aligned parallel to isobaths. This preference is diminished as depth increases (flattening of the PDFs in darker colors). Analogously, there is a clear inhibition of nearshore fronts and filaments aligned across isobaths $\left(\theta_{\nabla_h \rho} = -\pi/2, \pi/2\right)$.

These results corroborate the interpretations from the variance maps in Figure 2.4a,b; there is more extreme submesoscale activity (velocity and density horizontal gradients) closer to shore with the alignment and regional distribution of structures closer to shore controlled by regional bathymetry. Typically, the strongest flows associated with fronts and filaments is a (mainly) geostrophic longitudinal shear flow (demonstrated in Section 2.5.5). On the shelf, this flow can extend to or near the bottom due to the weak stratification and strong vertical mixing (Section 2.5.5). Shelf bathymetry can orient fronts and filaments by steering the associated longitudinal flow along isobaths. Another, perhaps secondary, degree of control lies in the interaction of the shape of the coastline with mean flows. The bay-wide regions of high vorticity and divergence variance show even larger variance at the headlands (Figure 2.4a,b). Background along-shore flows associated with vorticity generation at headlands could continually favor along-isobath alignment of headland-rooted submesoscale coherent structures.

2.5.3 Frontogenetic tendencies

In the realistically complex situation in our simulation, all of the submesoscale generation processes (Section 2.3) are likely to occur. Rather than attempt to untangle these three different mechanisms, we investigate the processes responsible for frontogenesis, *i*.e., what causes $|\nabla_h b|^2$

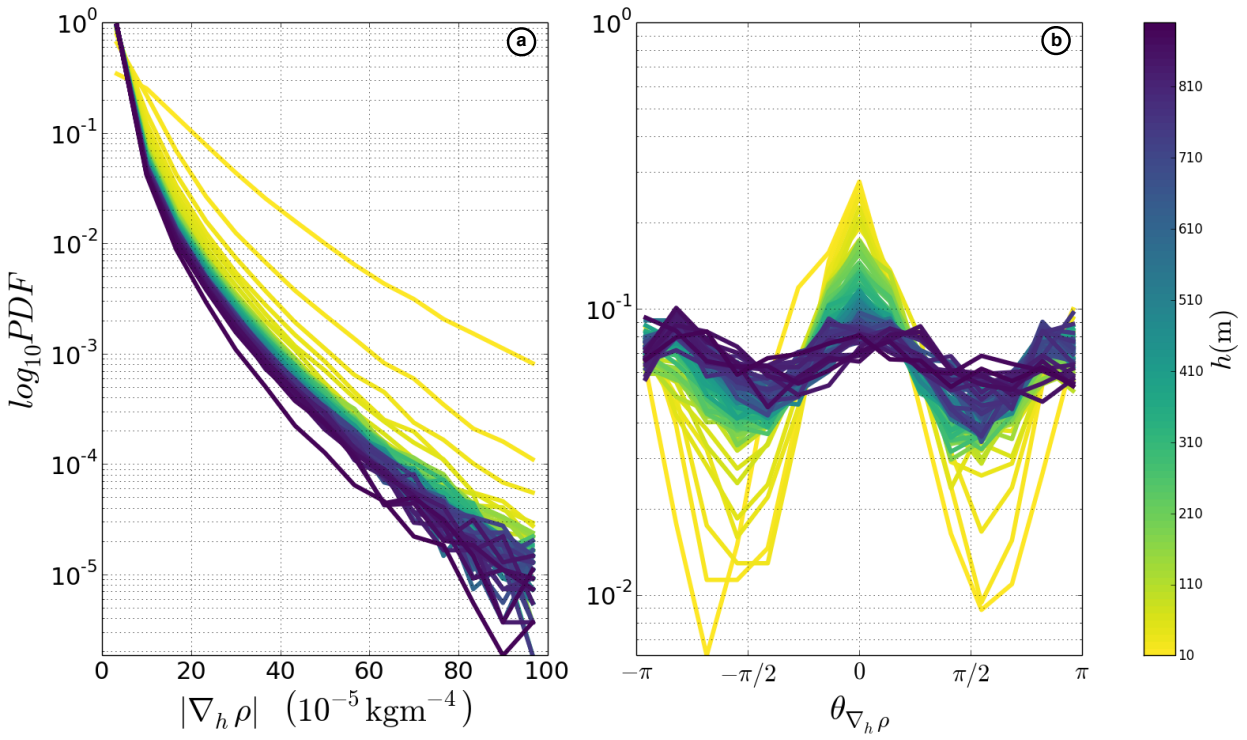

Figure 2.5: PDFs (log_{10}) of surface density gradient vector magnitude (a) and angle (b) relative to different isobaths (colors). Each PDF of surface density gradient magnitude $|\nabla_h \rho|$ is calculated from 300 points along each isobath for all 151 days of simulation. The PDFs of the density gradient angles $\theta_{\nabla_h \rho}$ are obtained from density gradient vectors in which the magnitude exceeds 5 times the RMS value of $|\nabla_h \rho|$ (RMS is relative to data points along a specific isobath). Angle conventions are such that $\theta_{\nabla_h \rho} = -\pi, 0, \pi$ correspond to the density gradient vector pointing across isobaths. Note, depth h is indicated as a positive value here (opposite to the convention in Figure 2.2)

and $|\nabla_h \boldsymbol{u}|^2$ in submesoscale structures on the shelf. Does the formation of shelf coherent structures mirror the formation of open-ocean analogs, or does the topographic control on spatial distribution and alignment exert itself in the formation process as well?

To aid our interpretation in “catching" the precise moment of formation a shelf filament, we use 30 min. averaged output of L3 solutions over a period of two days during a cold filament’s lifecycle. The rapid growth and elongation of this cold filament is shown as it forms near Newport Harbor in Figure 2.6a-d. We refer to this filament as Filament1. We illustrate the formation of

the filament in SST, noting that there is an analogous signal in SSS. A cold, salty (relative to its surroundings) cyclonic vortex exists on the very narrow shelf off of Newport Harbor. In the sequence, there is a clear stretching and elongation of the cold patch just off of the shelf-break; the result of the horizontal strain field acting on the buoyancy gradient.

We quantitatively diagnose the specific processes responsible for front or filament formation through the frontal tendency equations. The usual practice is to decompose the terms responsible for amplification of the buoyancy gradient in time $\frac{1}{2}\frac{D|\nabla_h b|^2}{Dt}$ as in *Hoskins* [1982]; *Capet et al.* [2008b]; and *Gula et al.* [2014]. However, for filament frontogenesis it is informative (and more striking visually) to look at the evolution of the velocity gradient $\frac{1}{2}\frac{D|\boldsymbol{\nabla}_h(u,\, v)|^2}{Dt}$ (following *McWilliams et al.* [2015]):

$$\frac{1}{2}\frac{D}{Dt}\begin{pmatrix}|\boldsymbol{\nabla}_h u|^2\\ |\boldsymbol{\nabla}_h v|^2\end{pmatrix} = \sum_i \begin{pmatrix}T_{i,u}\\ T_{i,v}\end{pmatrix} = \sum_i \begin{pmatrix}\boldsymbol{Q}_{i,u}\cdot\boldsymbol{\nabla}_h u\\ \boldsymbol{Q}_{i,v}\cdot\boldsymbol{\nabla}_h v\end{pmatrix}, \tag{2.6}$$

where $T_{i,u}, T_{i,v}$ represent individual frontogenetic tendency terms that account for a physical process inherent in the momentum equation (i = horizontal advection, vertical advection, vertical mixing, etc.) that can contribute to amplification ($T_i > 0$, frontogenetic) or reduction ($T_i < 0$, frontolytic) of the velocity gradient ($|\boldsymbol{\nabla}_h u|^2$ or $|\boldsymbol{\nabla}_h v|^2$). For this analysis we present the frontogenetic tendency for the velocity gradient T_i as the sum of the tendencies for the individual u and v gradients ($T_i = T_{i,u} + T_{i,v}$) where individual processes contributing to frontogenetic or frontolytic behavior are accounted for by the $\boldsymbol{Q}_i$ vector. These processes are horizontal advection ($\boldsymbol{Q}_{adv}$), vertical advection ($\boldsymbol{Q}_w$), Coriolis conversion $\left(\boldsymbol{Q}_f\right)$, pressure gradient $\left(\boldsymbol{Q}_\phi\right)$, vertical mixing ($\boldsymbol{Q}_{dv}$),

and horizontal diffusion ($\boldsymbol{Q}_{dh}$). They are defined as follows (written as (u, v) components):

$$\left(\boldsymbol{Q}_{adv,u}, \boldsymbol{Q}_{adv,v}\right) = \left(-u_x \boldsymbol{\nabla}_h u - u_y \boldsymbol{\nabla}_h v,\ -v_x \boldsymbol{\nabla}_h u - v_y \boldsymbol{\nabla}_h v \right), \tag{2.7a}$$

$$\left(\boldsymbol{Q}_{w,u}, \boldsymbol{Q}_{w,v}\right) = \left(-u_z \boldsymbol{\nabla}_h w,\ -v_z \boldsymbol{\nabla}_h w\right), \tag{2.7b}$$

$$\left(\boldsymbol{Q}_{f,u}, \boldsymbol{Q}_{f,v}\right) = \left(f \boldsymbol{\nabla}_h v + v \boldsymbol{\nabla}_h f,\ -f \boldsymbol{\nabla}_h u - u \boldsymbol{\nabla}_h f \right), \tag{2.7c}$$

$$\left(\boldsymbol{Q}_{\phi,u}, \boldsymbol{Q}_{\phi,v}\right) = \left(\boldsymbol{\nabla}_h \left(-\phi_x\right),\ \boldsymbol{\nabla}_h \left(-\phi_y\right) \right), \tag{2.7d}$$

$$\left(\boldsymbol{Q}_{dv,u}, \boldsymbol{Q}_{dv,v}\right) = \left(\boldsymbol{\nabla}_h \left(\frac{\partial}{\partial z} \left(\kappa_v \frac{\partial u}{\partial z} \right) \right),\ \boldsymbol{\nabla}_h \left(\frac{\partial}{\partial z} \left(\kappa_v \frac{\partial v}{\partial z} \right) \right) \right), \tag{2.7e}$$

$$\left(\boldsymbol{Q}_{dh,u}, \boldsymbol{Q}_{dh,v}\right) = \boldsymbol{\nabla}_h (D_{hu},\ D_{hv}). \tag{2.7f}$$

In Figure 2.6e-i (and later Figure 2.7h-l), the tendency term for horizontal diffusion T_{dh}, is not shown knowing that it is always frontolytic in ROMS due to the implicit hyper-diffusion D_h associated with the upstream advection operator [*Gula et al.*, 2014]. Similarly, we do not show T_f, which represents an exchange between the u and v components and will sum to zero except for a small term $\propto \beta = df/dy$. For a purely geostrophic flow, T_ϕ and T_{adv} are each zero. At higher order in Rossby number, the pressure field is often closely related to horizontal momentum advection, so we choose to show a combined $T_{adv} + T_\phi$ (as opposed to each individually) to interpret horizontal advective effects; we note that T_ϕ is similar in structure and lesser in magnitude than T_{adv} for the cases shown. Analysis of the terms controlling the buoyancy gradient frontogenetic tendency, $\frac{1}{2}\frac{D|\nabla_h b|^2}{Dt}$ (not shown), leads to similar conclusions about the relevant processes.

The total frontogenetic tendency is shown at $z = -5$ m in Figure 2.6e corresponding to Filament1 at the time in Figure 2.6a. There is a clear positive frontogenetic tendency indicative of a drastic increase in velocity gradient. The separate terms that contribute to this tendency are shown for a cross-section at the same time in Figure 2.6f-l. Horizontal advection $T_{adv}(+T_\phi)$ contributes the most to the frontogenesis. T_w, T_{dv} are frontolytic around the center of the filament.

The strong frontogenetic horizontal advective tendency, confined to a $\sim$ 10 m thick surface layer (Figure 2.6g), indicates that the surface layer horizontal flow structures surrounding the filament are responsible for its growth (rapid amplification of $|\nabla_h \boldsymbol{u}|^2$, Figure 2.6e). Offshore of the 100 m

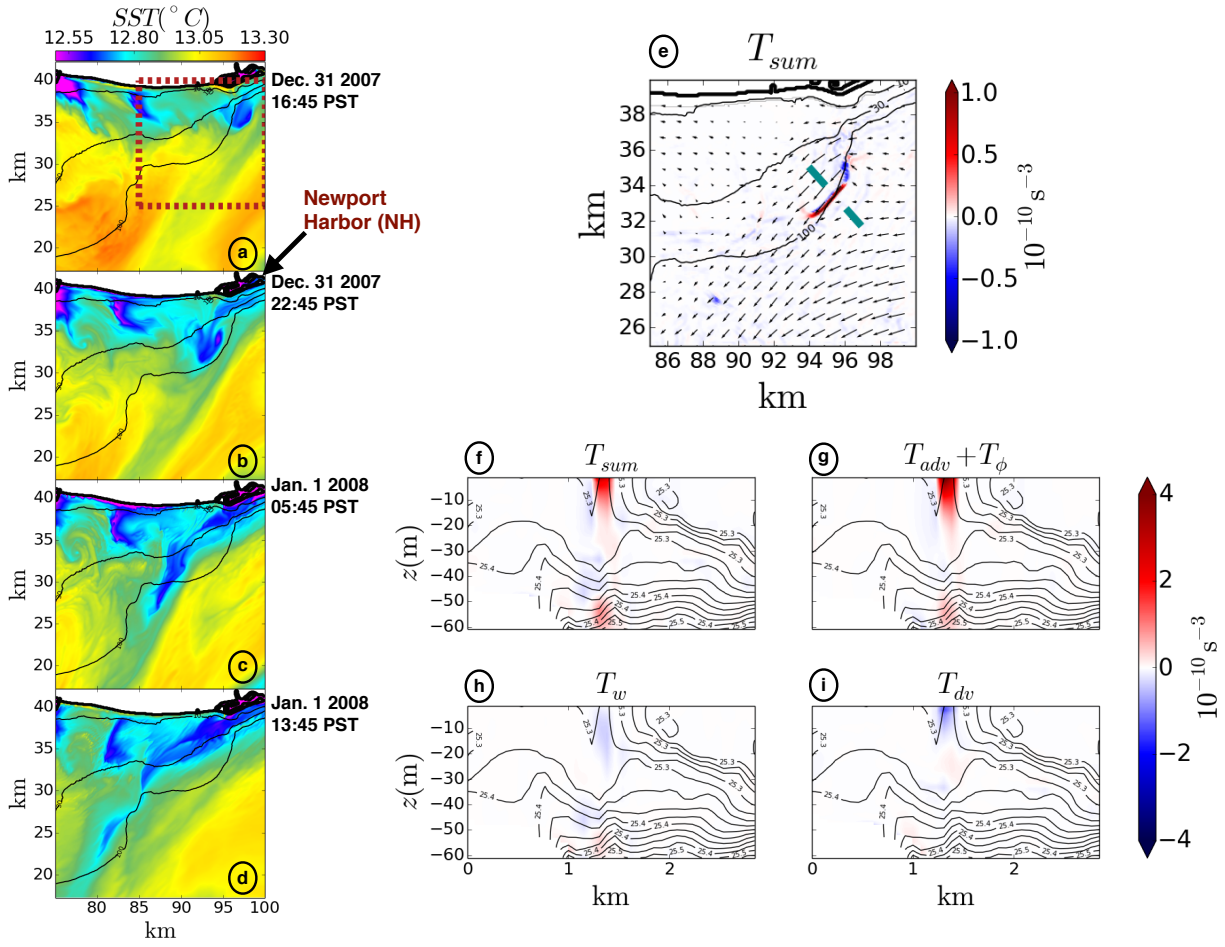

Figure 2.6: Frontogenesis of filament Filament1. (a) - (d): 30-min. averages of SST beginning on Dec. 31 2007 16:45 Pacific Standard Time (PST), separated by 8 hour intervals. (e): Total velocity gradient frontogenetic tendency for the region in the red dashed box in (a) at $z = -5$ m. (f) - (i): Separate frontogenetic terms for the transverse cross-section with end-points denoted by the cyan hashmarks in (e). Black vectors in (e) denote horizontal velocity at $z = -5$ m and black contours in (f) - (i) denote density.

isobath, a convergent flow pushes the nascent filament into shallower water. Inshore of the 100 m isobath, the large-scale flow strains the filament along-isobath to the southwest. The convergence by the offshore flow and strain by the inshore flow act to elongate and amplify both the velocity and buoyancy gradient in a mixture of the *Hoskins* [1982] deformation flow and *McWilliams et al.* [2015] convergent secondary circulation mechanisms of frontogenisis. The relatively large submesoscale activity (Figure 2.4a,b) and large horizontal strain $\left(S = \sqrt{(u_x - v_y)^2 + (v_x + u_y)^2}\right)$ variance (not shown) near Newport Harbor indicate that the formation of submesoscale density

gradients, driven by the favorable alignment of flows off- and inshore of the 100 m isobath (Figure 2.6e), is not an anomalous event in this region. The orientation of the local bathymetry and coastline surrounding Filament1 may topographically steer large-scale flow fields in a way that favors repeated generation of submesoscale structures in this area near the shelf-break.

The general picture from Figure 2.6 is filament formation driven mainly by frontogenetic horizontal advection with simultaneous but weaker frontolytic vertical advection and vertical mixing; it generally agrees with Gulf Stream filament formation analyzed in *Gula et al.* [2014]. However, the orientation of the shelf bathymetry relative to the coastline exerts some control on the frontogenetically favorable ambient flow configurations, and the shallow depth can lead to non-trivial frontogenetic tendencies near the bottom. The surface-driven, advectively dominated formation mechanism of this submesoscale density gradient is distinct from the BBL-associated formation mechanisms for shelf-break and tidal-mixing fronts. It is distinct from both the "frontal trapping" formation mechanism of shelf-break fronts [*Chapman and Lentz*, 1994] and the formation of tidal mixing fronts that fundamentally involves tidally-induced vertical mixing [*Simpson and Hunter*, 1974].

2.5.4 Influence of the coastline: a headland wake event

The formation of Filament1 is essentially controlled by the surface flow field and is somewhat analogous to formation of open-ocean filaments [*Gula et al.*, 2014]. However, the ambient-flow frontogenesis for Filament1 seems to be controlled by the interaction of large-scale flows and the orientation of the shelf bathymetry relative to the coastline. As revealed by the metrics in Figures 2.4 and 2.5, the shape of the coastline and bathymetry are important influences on the regional heterogeneity of submesoscale processes on the shelf. Specific areas along the coastline can act as formation sites for submesoscale structures (*e*.g., headlands and breakwaters).

A striking illustration of the influence of the coastline is shown in the simultaneous formation

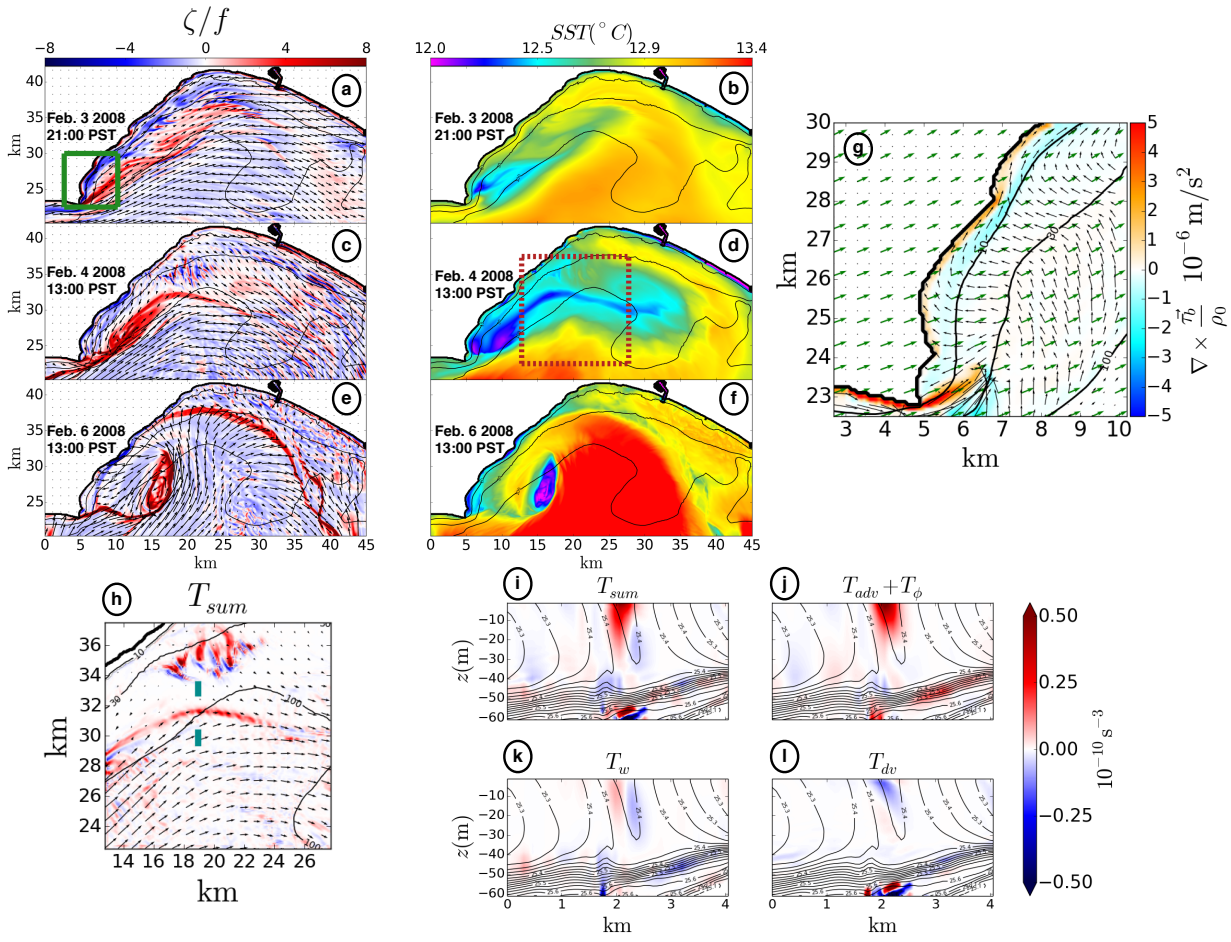

Figure 2.7: Headland wake frontogenesis of filament Filament2. 2-hour averages of surface relative vorticity (a), (c), (e) and SST (b), (d), (f) are shown for three separate times (rows, beginning on Feb. 3, 2008 21:00 PST) (note uneven times between second and third rows). (g) Curl of the bottom stress (colors), surface wind stress (green vectors) and, bottom velocity (black vectors) of the green-region in (a). (h): Total velocity gradient frontogenetic tendency for the region in the red dashed box in (d) at $z = -5$ m. (i) - (l) Separate frontogenetic terms for the transverse cross-section with end-points denoted by the cyan hashmarks in (h). Black vectors in (a), (c), (e) denote surface horizontal velocity and in (h) denote horizontal velocity at $z = -5$ m. Black contours in (i) - (l) denote density.

of a cold-core vortex and cold filament in Figure 2.7, at the Point Dume headland (referred to as Filament2) . The sequence of events in this figure is a combination of the following processes: shallow-water wake formation due to horizontally varying bottom drag (Figure 2.7g), upwelling

due to wind-stress curl, and filament frontogenesis mainly driven by horizontal advection (Figure 2.7i - l). The initial cyclonic vorticity in Figure 2.7a can primarily be explained by highly localized vertical vorticity generation due to bottom drag ($\nabla \times \boldsymbol{\tau}_b > 0$), which is due to strong mean flow past the headland (Figure 2.7g). The upwelling of cold, salty water at the headland is in part due to upwelling-favorable wind-stress curl. The wind-stress is shown in green arrows in Figure 2.7g, and the upwelling is also indicated by the on-shore bottom flow (black arrows Figure 2.7g) intersecting the coastal boundary. The cyclonic vorticity created by the bottom drag fits the mechanism invoked in shallow-water island wake formation [*Wolanski et al.*, 1984; *Tomczak*, 1988; *Furukawa and Wolanski*, 1998] and in the flow along a sloping bottom [*Molemaker et al.*, 2015]. The horizontal shear created by the eastward flow in contact with the headland, the upwelling of denser water in the lee of the headland, and topographic steering within SMB gives rise to the fully-evolved coherent structures of a cold-core vortex and a cold-filament that roughly traces out bay-wide bathymetry (Figure 2.7c-f). Notice the detachment of the vortex from the headland and the separation of the filament from the vortex in Figure 2.7e,f. While Filament2 is an example of a cyclonic coherent structure, the surface vorticity skewness map in Figure 2.4c shows small patches of anticyclonic vorticity generation to the west of both headlands, associated with episodes of westward flow.

The frontogenetic tendencies of Filament2 are analyzed in Figures 2.7h - l. Analogous to the result for Filament1, horizontal advection $T_{adv}(+T_{\phi})$ is positive and dominates the sum of the frontogenetic tendency. Cross-sections of the separate terms (Figures 2.7i - l) show that T_{dv} is mainly frontolytic, with a very weak frontogenetic tendency on the inshore side of the filament nearest the surface. T_w is sign-symmetric around the center of the filament. Overall, horizontal advection takes over the frontogenetic sequence after the initial cyclonic vorticity creation which is fundamentally controlled by the shape of the coastline. This sequence of events is unique to coastal submesoscale density gradients and has no analog in the open-ocean surface layer.

2.5.5 Front and filament circulations

Here we present both the success and limitation of the TTW balance (2.1) in diagnosing the circulations associated with fronts and filaments on the shelf. Motivated by an example of the failure of the TTW diagnostic, we investigate the transient evolution of secondary circulations and raise questions regarding the steady-state assumption inherent in the TTW diagnostic.

For the finite-depth shelf, we impose the following boundary conditions on (2.1):

$$\kappa_v \frac{\partial \boldsymbol{u}_h}{\partial z} = \frac{\boldsymbol{\tau}^s}{\rho_0} \qquad \text{at } z = 0\,, \qquad \kappa_v \frac{\partial \boldsymbol{u}_h}{\partial z} = \frac{\boldsymbol{\tau}^b}{\rho_0} \qquad \text{at } z = -h\,. \tag{2.8}$$

The inclusion of a bottom stress ($\boldsymbol{\tau}_b$) is specific to shelf fronts and filaments that are commonly in contact with the bottom due to the combination of the shallow-depths ($O(10$ m $)$) and low stratification induced by the strong mixing that sets up and maintains the secondary circulations. $\boldsymbol{\tau}_b$ is computed from the L3 solution bottom sigma-level velocity using the bottom-layer quadratic drag law given by (2.3).

The TTW longitudinal (u) and transverse (v) velocities can be calculated from ROMS output with knowledge of the density (ρ), vertical mixing (κ_v), surface wind stress ($\boldsymbol{\tau}_s$) and, on the shelf, the bottom velocity ($\boldsymbol{u}_b$). Discretization of (2.1) results in a tridiagonal system and can be solved by a simple matrix inversion if the coefficient matrix is diagonally dominant. The discretization is analogous to that of *McWilliams et al.* [2015]) with here the inclusion of a bottom stress in the bottom boundary condition.

Examples of TTW balance: To investigate this mechanism for shallow-water fronts and filaments in contact with the bottom, we isolate 3 submesoscale features shown in Figure 2.8: Filament3, Filament4 and Front1. The input fields for the calculation ($\kappa_v, \boldsymbol{\tau}^s, \boldsymbol{\tau}^b, \rho$) are obtained by isolating the submesoscale feature at the locations denoted by the black hashmarks in Figure 2.8. Front1 is shown in Figure 2.8 at two times (bottom two rows) to show an example of diurnal

evolution discussed in the next subsection. The TTW input fields and solutions (Figures 2.9, 2.10, 2.11) are shown as longitudinal averages in the transverse-depth (y, z)-plane.

The first case, Filament3, is a cold filament (isolated at 03:00 PST) located just offshore of Manhattan Beach roughly between the 10 and 50 m isobaths (top row Figure 2.8). In the nearshore, the filament is oriented at roughly a 45°angle to the 10 m isobath and bends to a more along-isobath parallel orientation further offshore and towards the south (to the right along the horizontal axis). It has a sharp temperature gradient with strong cyclonic vorticity and convergence at the surface. Figure 2.9a,b shows transverse-depth structure (longitudinally averaged) of potential density ($\rho(y, z)$) and parameterized vertical mixing ($\kappa_v(y, z)$). The two main ingredients for the TTW circulation are apparent: a strong horizontal density gradient (not explicitly shown) across the transverse axis (roughly uniform from the surface down to ~ -35 m depth) and strong $O(10^{-2}\ \mathrm{ms}^{-2})$ vertical mixing. Of note is the trend in κ_v to decrease in strength in shallower water. This is a general statistical cross-shore trend explained by the influence of the decreasing depth; the magnitude of κ_v (produced by KPP) is primarily controlled by boundary layer depth (here interpreted as depth of the water column). We also note that this filament occupies both the continental shelf (separate SBL and BBL) and the SSTZ (overlapping SBL and BBL) of Figure 2.1.

Velocities for Filament3 are shown in Figure 2.9c,d after being rotated into a filament frame of reference. The circulation is characterized by a cyclonically-sheared longitudinal flow and a transverse circulation that is convergent at the surface and divergent at depth (the secondary circulation). Geostrophic balance ($u_g = -\phi_y/f, v_g = \phi_x/f$) fails to reproduce the complete structure of this transverse flow (Figure 2.9e,f), and also does not fully capture the extent of vertical mixing of the longitudinal flow. The ageostrophic secondary circulation is better captured by the TTW balance ($u_{\mathrm{TTW}}, v_{\mathrm{TTW}}$) (Figure 2.9g,h). This result is analogous to the TTW success for open-ocean filaments in *Gula et al.* [2014] and provides a validation of the TTW balance in shallow water with overlapping boundary layers.

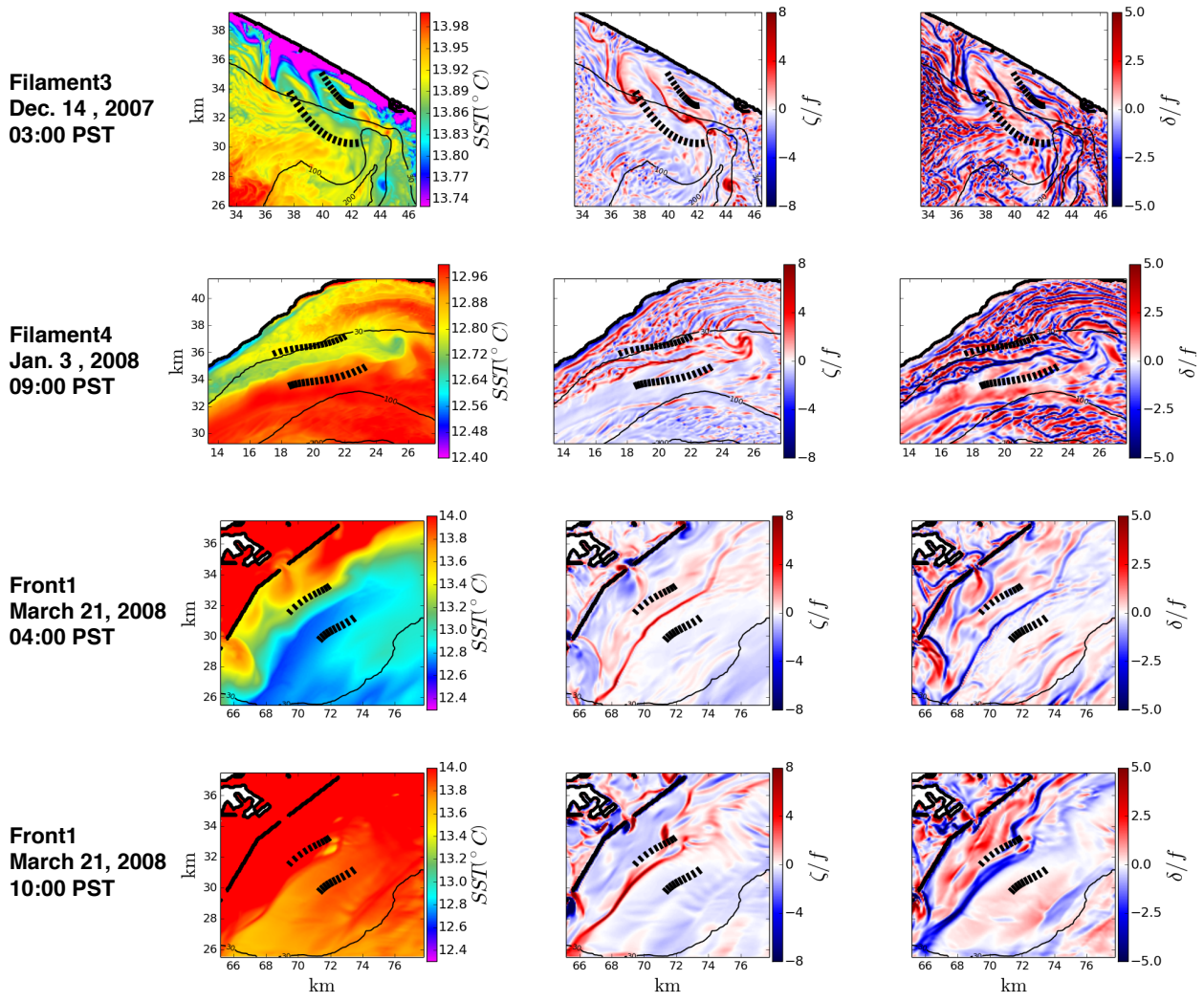

Figure 2.8: Surface fields for the fronts and filaments (rows) used for TTW diagnostic calculation. SST (left), relative vorticity (middle) and divergence (right). The features are isolated by fitting a polynomial curve to the shape of the cyclonic vorticity line indicating the front or filament. Transverse cross-sections 3 km in length are taken between the end-points indicated by the black hash-marks and centered on the fitted curve. Velocities and stresses are then rotated into a frame of reference of the feature (x, y pertaining to longitudinal and transverse axes, respectively).

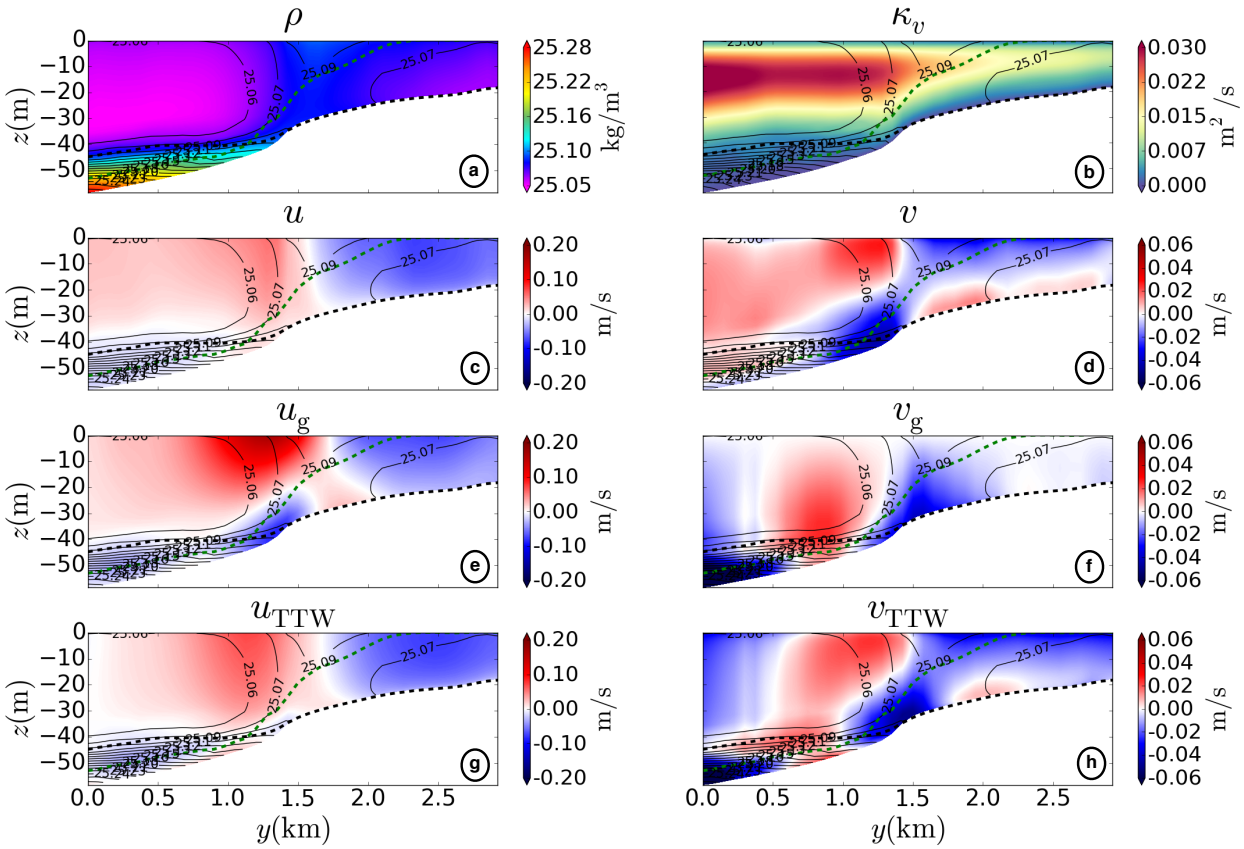

Figure 2.9: Longitudinally averaged of fields for Filament3 cross-sections: Density (a), vertical mixing (b). Longitudinal velocity u and transverse velocity v are shown in 3 components: raw(c),(d), geostrophic (e),(f) and TTW(g),(h). Black contours denote density, dashed lines denote surface (black) and bottom (green) boundary layer depths. Bottom boundary layer depth is plotted relative to the bottom (*i*.e., vertical extent of bottom boundary layer). Sign conventions are such that positive u is out of the page and positive v is to the right along the horizontal axis. For the TTW calculation itself, the pressure gradient in the longitudinal direction ($\partial\phi/\partial x$) is modified to exclude the effect of larger scale processes. This is done by setting the free surface height (η) gradient in that direction to zero ($\partial\eta/\partial x = 0$) and calculating pressure with this modified free surface. There is also some spatial smoothing done to the transverse pressure gradient ($\partial\phi/\partial y$). TTW velocities are computed for each horizontal cross-section with the longitudinal composite of individual cross-sections shown here; that is, we assume longitudinal uniformity of the front or filament circulation.

Front1 is a shelf front located off of Long Beach Harbor in SPB (isolated at 04:00 PST) (third row Figure 2.8)). The front is characterized by colder water offshore and warmer water onshore, with very well-defined lines of cyclonic vorticity and surface convergence coincident with the location of maximum temperature gradient. The TTW diagnostic is moderately successful (relative to Filament3) in recreating the longitudinal shear flow as well as the ageostrophic secondary circulation (Figure 2.10). There are some differences between the raw and TTW transverse velocity profiles. Notably, there is a patch of negative transverse velocity on the far-side of the $y-$axis in the TTW profile. This coincides with (and is potentially the result of) both an increase in stratification, a decrease in κ_v, and decrease in $\partial\phi/\partial y$ (*i*.e., the ingredients for TTW).

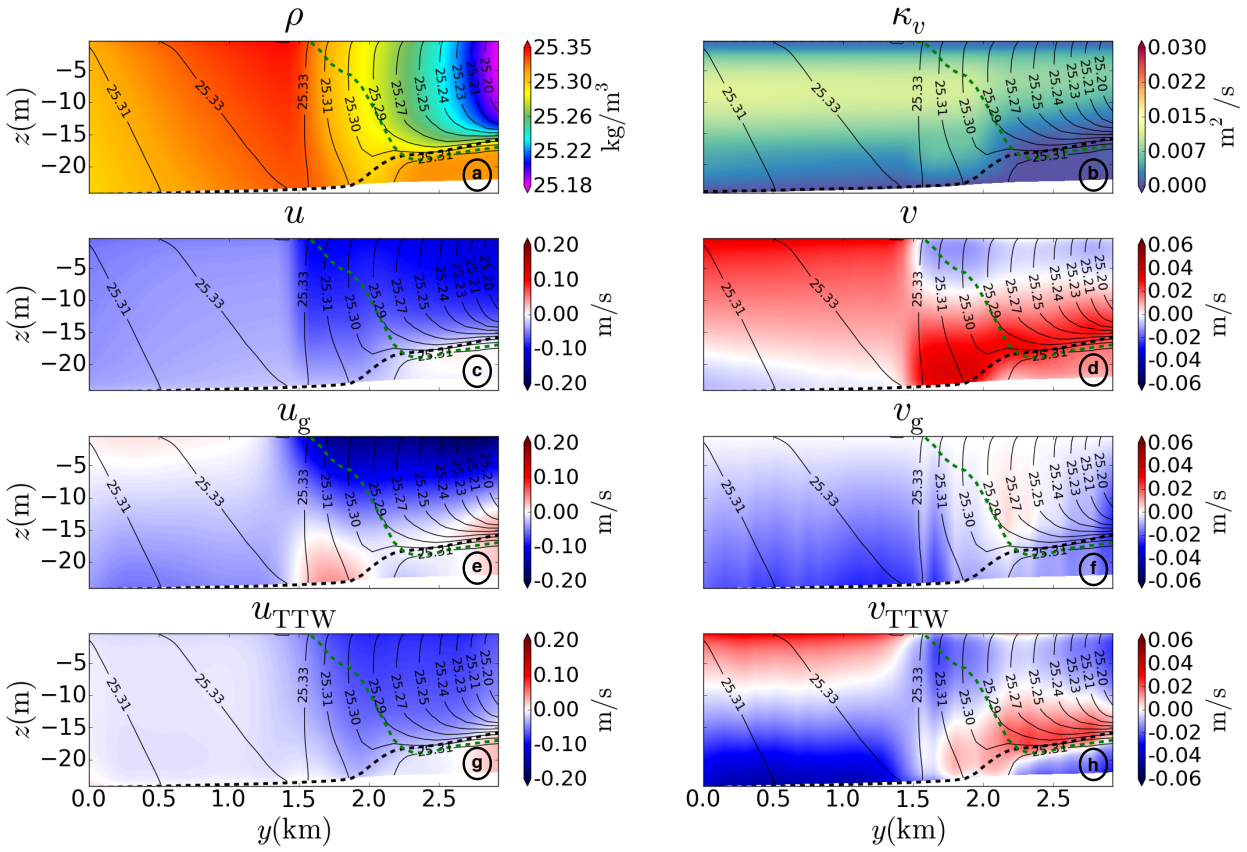

Figure 2.10: As in Figure 2.9 for Front1 in Figure 2.8

Filament4 appears as a shelf front [4] (isolated at 09:00 PST) in SMB offshore of Malibu (second row Figure 2.8) oriented roughly parallel to the local isobaths. There are two notable aspects of

[4] Filament4 exhibits a frontal structure at this time, however its time-mean (Figure 2.13) resembles a cold-filament and thus we name it Filament4.

this case to mention relative to Filament3 and Front1. First, the vertical mixing shape (Figure 2.11b) is markedly different for this case (at this point in time in the front's life-cycle) than the previous two cases discussed (Filament3 and Front1). Secondly, the TTW balance does not (as) convincingly reproduce the very strong and apparent secondary circulation (Figure 2.11d) associated with this front. The vertical mixing structure is weak at the surface due to increased stratification (Figure 2.11a) caused by a positive solar heat flux associated with the daytime hour (09:00) of the feature isolation. BBL mixing is present on the inshore side of the filament where it comes in contact with the bottom with a reduced stratification on this inshore side.

This case is of interest because the raw transverse flow exhibits a clear and very strong secondary circulation (Figure 2.11d). However, the TTW diagnostic is not reproducing the strength and complete geometry of this secondary circulation (Figure 2.11h). The presence of a strong secondary circulation coincident with relatively weak vertical mixing presents a conundrum for the diagnostic view of (2.1). Next, we investigate the transient evolution of submesoscale indicating fields to show that the diurnal cycle in vertical mixing (presumably forced by solar heat flux or wind) induces a transient response of front and filament circulation that is apparently not captured by the steady-state TTW balance.

Diurnal evolution of secondary circulation: We illustrate the diurnal evolution of secondary circulation (as it relates to cycling of κ_v) with a 4-day time series of multiple fields in Figure 2.12. The time-series in Figure 2.12 are spatial RMS values (normalized by their respective standard deviations in time) of fields at $z = -7$ m for a region indicated by dashed-black lines in Figure 2.2b; Q_s is plotted as a spatial mean. The diurnal cycling of κ_v is apparent in Figure 2.12. It is representative of the surface layer KPP response: KPP enhances vertical mixing at the surface via both a surface cooling ($Q_s < 0$) and/or a strong surface stress ($|\boldsymbol{\tau}_s| > 0$). κ_v has a diurnal cycle characterized by sustained mixing in the night-time hours (17:00-07:00) followed by an abrupt transition to a low mixing regime during the day (09:00-15:00). The stratification (N^2) diurnally evolves consistent with changes in κ_v: stronger stratification with weaker mixing and vice versa

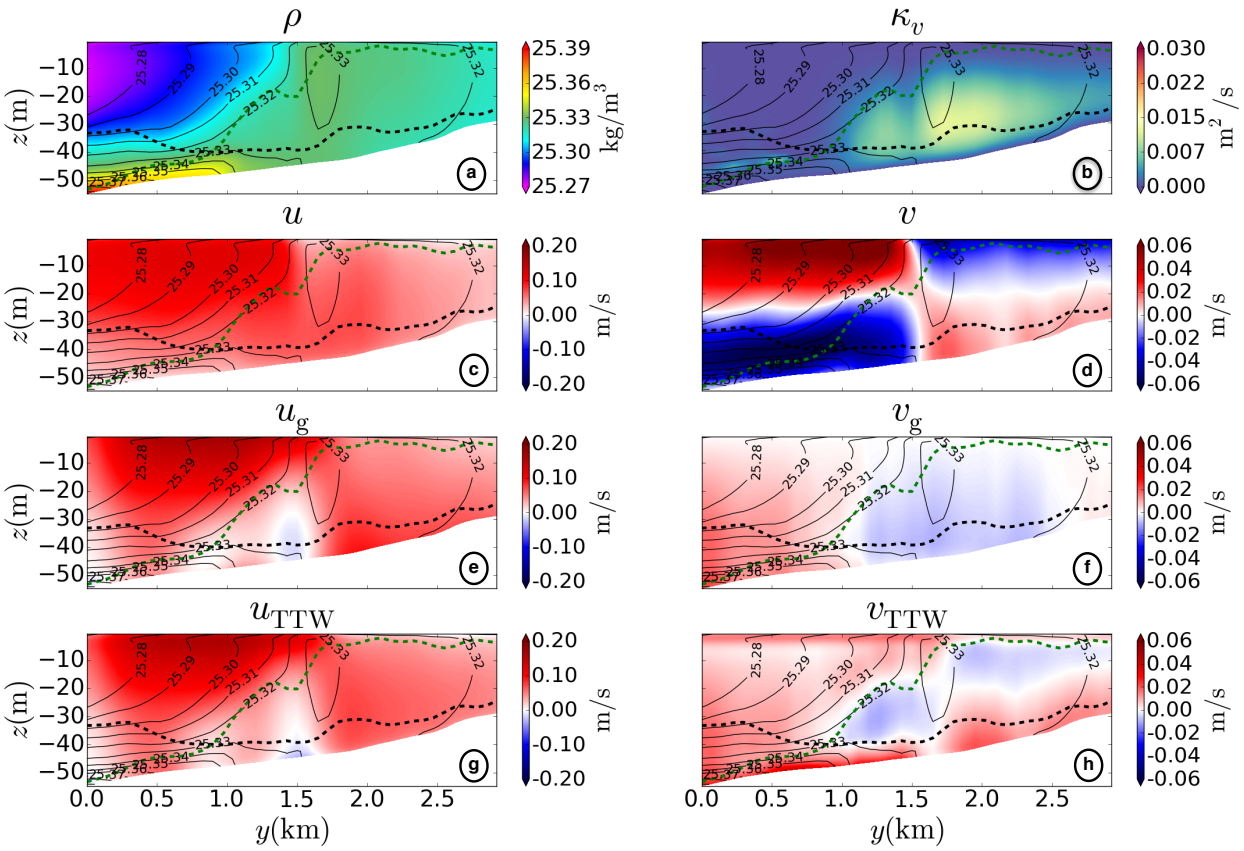

Figure 2.11: As in Figure 2.9 for the Filament4 in Figure 2.8. We note the name of Filament4 in reference to the overall life-cycle of this density gradient structure that is analyzed in Figure 2.13. Despite its frontal structure in this 2-hour average, it has a time-mean over its life-cycle more resembling a cold filament. Note the failure of the TTW balance to reproduce the transverse circulation v vs v_{TTW}. The failure of the TTW diagnostic is attributed to its inability to capture the full diurnal evolution of the secondary circulation as it responds to temporal changes in vertical mixing (which is weak and bottom intense in this 2-hour average, (b)).

(Figure 2.12, gray curve).

The surface wind stress can certainly induce vertical mixing and potentially control the diurnal signal of κ_v through a diurnal sea-breeze, which is common in Southern California [*Nam and Send*, 2012]. For SMB, the sea-land breeze phasing is a daytime onshore wind (ocean to land) and night-time offshore wind. If the onshore breeze is strong enough during the daytime, it can increase

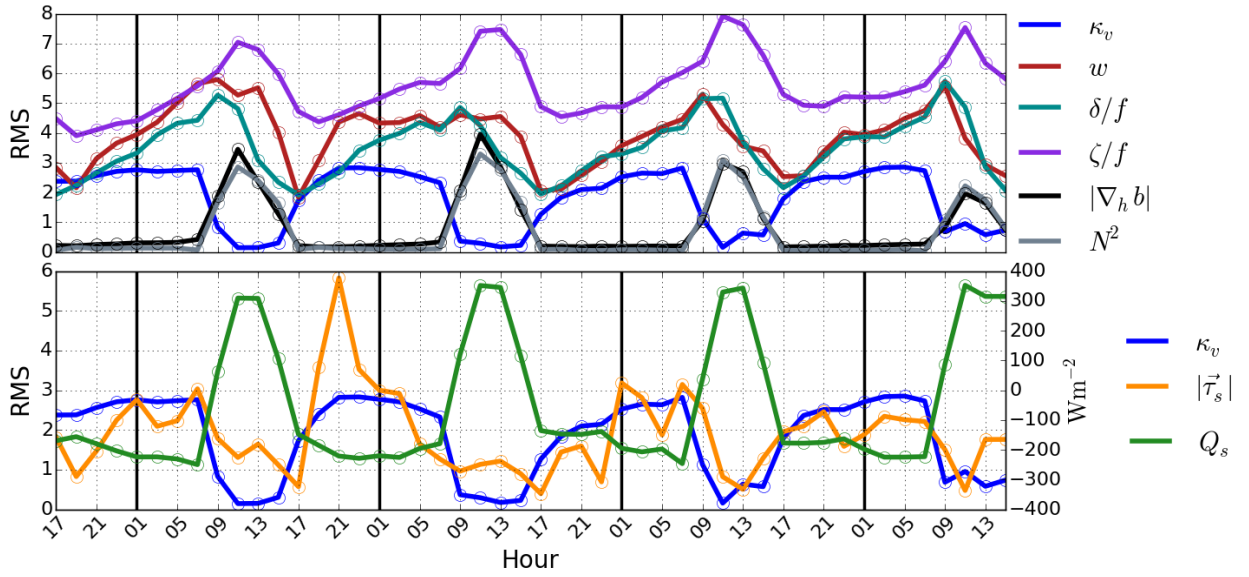

Figure 2.12: Four-day time series of spatial RMS values (starting on December 13, 2007 17:00 PST) taken from the black dashed box in SMB shown in Figure 2.2b. Top: vertical mixing (κ_v), relative vorticity (ζ/f), divergence (δ/f), vertical velocity (w), buoyancy gradient magnitude ($|\nabla_h b|$), Brunt-Väisälä frequency squared (N^2). All fields in the top panel are computed at $z = -7$ m. Bottom: vertical mixing (κ_v, at $z = -7$ m), and surface wind stress magnitude ($|\boldsymbol{\tau}_s|$). Surface heat flux Q_s (Wm^{-2}) values are plotted corresponding to the vertical axis on the right. Dots represent 2-hour averaged individual time-points. Vertical black lines separate days. Each spatial RMS for a variable is normalized by its standard deviation in time.

and dominate the vertical mixing (relative to stratifying effects of $Q_s > 0$ that can weaken the mixing). However, the most notable peaks in $|\boldsymbol{\tau}_s|_{RMS}$ (the large peak of the orange curve in Figure 2.12 at 21:00 on December 14) are due to a local wind event in Malibu with strong off- and along-shore winds that occur in the nighttime hours, coincident with strong surface cooling. Despite this strong wind-stress, the surface cooling (Q_s minima in green curve Figure 2.12) appear to control the maxima in vertical mixing (blue curve in Figure 2.12); that is, the maxima of RMS κ_v are consistent across the four days of the time-series and show no discernible increase during the distinct maximum in $|\boldsymbol{\tau}_s|_{RMS}$, indicating that during this period the diurnal cycle of κ_v is being primarily driven by the solar heat flux (Q_s).

Time-series of the RMS of submesoscale indicators ($w, \delta/f, \zeta/f, |\nabla_h b|$) relative to the temporal evolution of vertical mixing show responses to large $\partial\kappa_v/\partial t$ (Figure 2.12 top panel). The main behavior apparent in these time-series is the increase in δ/f and w RMS in response to negative $\partial\kappa_v/\partial t$. This peak in divergence RMS (*i*.e., peak in the strength of the secondary circulation) occurs at roughly 09:00 each day in the time series, coincident with a sharp drop-off in κ_v. ζ/f and $|\nabla_h b|$ are phase-aligned and lag $\delta/f, w$ by ~ 2 hours. The diurnal evolution of these fields is not consistent with a sequence of instantaneous TTW calculations (*e*.g., Figure 2.11g,h). Such a diagnostic (summarized by (2.2)) predicts a phase alignment between κ_v and the secondary circulation ($\delta/f, w$) for a given transverse buoyancy gradient.

Another aspect of transient evolution of fronts and filaments is a diurnal “flashing" of surface vorticity, divergence, and vertical velocity. The “flashing" is an increase in transverse thickness (and strength) of the latter fields illustrated with a comparison of Front1 at 04:00 and 10:00 local time (bottom two rows in Figure 2.8). The front is (relatively) thin at 04:00 with well defined temperature gradient, vorticity, and divergence signals amidst strong vertical mixing throughout the water column (not shown). The strength of the vertical mixing at the surface can be attributed to a uniformly negative solar heat flux ($Q_s \sim -140$ W/m^2) and a non-negligible surface wind stress ($|\boldsymbol{\tau}^s| \sim 3 \times 10^{-2}$ N/m^2) oriented in a roughly cross-front direction (not shown). At 10:00, strong solar heat flux ($Q_s \sim 750$ W/m^2) and relative lack of wind lead to stronger stratification and less vertical mixing in the surface layer. The temperature gradient remains and is in fact somewhat stronger at 10:00 (not shown). The heat flux imprint is clearly seen in the temperature map (which has been kept at the same color scale for comparison with the front at 04:00) with warmer temperature throughout. The lines of vorticity and divergence remain well defined and are notably wider than at 04:00.

The transient evolution of secondary circulations — both phasing of the secondary circulation and the transverse thickening/thinning of vorticity and divergence lines — is presented here as evidence of a diurnal cycle in the local circulation of fronts and filaments that has previously not been observed. Its dynamical mechanisms are investigated separately in Chapter 3.

2.5.6 Vertical heat flux

Strong downwelling induced by the ageostrophic secondary circulations of fronts and filaments can induce vertical heat fluxes in the 3D heat balance:

$$\frac{\partial T}{\partial t} + \nabla_h \cdot \boldsymbol{u}_h T + \partial_z w T = \partial_z \left(\kappa \partial_z T\right) \ . \tag{2.9}$$

Here we compare the terms in (2.9) responsible for vertical fluxes in a shelf front or filament over 3-day periods. The heat flux due to vertical advection (J_w) and due to vertical mixing (J_κ) for a front or filament are calculated as

$$J_w = \rho_0 C_p w T' \,, \qquad J_\kappa = \rho_0 C_p \kappa_v \frac{\partial T'}{\partial z} \,, \tag{2.10}$$

where the temperature anomaly, $T' = T - \overline{T}$ is defined as the deviation from the transverse mean $\left(\overline{T}\right)$ over a distance much larger than the submesoscale feature. The space-time averaging of the isolated front or filament fields results in $\overline{w} \sim 0$ and $w \sim w'$ for the heat flux calculations. We calculate a temporal average of these terms by "following" fronts and filaments over the course of 3 days with the same feature-isolation techniques used to diagnose the secondary circulations in Section 2.52.5.5 (cross-sections rotated into a frame of reference of the front or filament at each time step). Time- and longitudinal composites of fields for a front on the SPB shelf (Front2) and a cold filament on the SMB shelf (Filament4) are shown in Figure 2.13 (2-hour averages of surface fields for Front2 and Filament4 are shown in Figures 2.3 and 2.8, respectively) The vertical heat fluxes (J_w, J_κ) in Figure 2.13e,f,k,l represent the net heat flux over the 3 day period. Filament4 [5] and Front2 reside on the shelf throughout their lifecycle and are chosen as the most compelling illustrative cases for this analysis (relative to the other features in Table 2.2). Based on similar analysis in previous work [*Gula et al.*, 2014; *McWilliams et al.*, 2015; *McWilliams*, 2017], we expect a net restratifying vertical heat flux for any submesoscale secondary circulation (front or filament).

Both the front and filament are characterized by a strong time mean negative vertical velocity ($O(10^{-2}$ ms$^{-1})$) which peaks at mid depth (Figure 2.13a,g), by a nearly full-mixed water column

[5] We note that the density (and temperature anomaly) structure of Filament4 (Figure 2.13d) exhibits asymmetry in its warm temperature anomalies surrounding the cold center. We classify this structure as a filament because it is more clearly a transverse extrema in temperature than a transverse step as in Front2 (Figure 2.13j).

indicated by strong vertical mixing (Figure 2.13b,h), by overlapping boundary layers in the time mean, and by negative temperature anomalies at the center of the cross-sections (cold front and cold filament, Figure 2.13d,j). The resulting vertical heat flux profiles are dominated by the positive advective heat flux (J_w), which is indicative of the restratification effects of the secondary circulations. The heat fluxes due to vertical mixing are weaker and negative. For Filament4, the advective heat flux peaks at 198 Wm^{-2} at $z = -15$ m. Front2 has an even stronger advective flux of 383 $\mathrm{W/m}^2$, which peaks around mid-depth at $z = -20$ m. These advective fluxes are compared with vertical mixing fluxes (J_κ) of -76 Wm^{-2} and -73 Wm^{-2} for the front and filament, respectively.

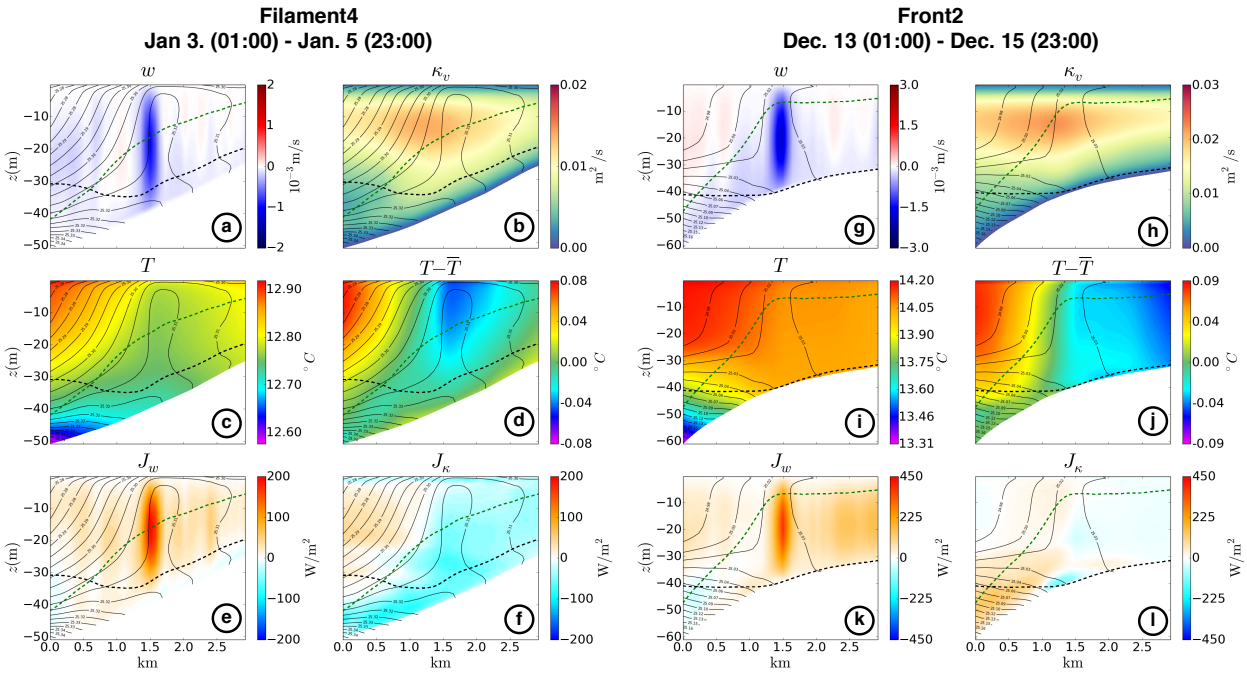

Figure 2.13: Time- and longitudinal averaged cross-sections for the Filament4 (Jan 3 01:00 - Jan 5. 23:00, left) and front Front2 (Dec 13 01:00 - Dec 14 23:00, right) Vertical velocity (a,g), vertical mixing (b,h) temperature (c,i), temperature anomaly in the cross-front (d,j), advective vertical heat flux (e,k) and vertical heat flux due to turbulent vertical mixing (g,l). Black contours denote density, dashed lines denote surface (black) and bottom (green) boundary layer depths. Bottom boundary layer depth is plotted relative to the bottom (*i*.e., vertical extent of bottom boundary layer).

The general picture these two cases present is that over the course of a shelf front or filament

life-cycle the TTW secondary circulations induce $O(100\ \mathrm{Wm}^{-2})$ fluxes that act to restratify the water column and dominate over weaker heat fluxes caused by vertical mixing that oppose the restratification effects. In the context of (2.9) it is clear from the unequal magnitudes of J_w and J_κ that the horizontal heat flux is playing a role in this time-mean, local front or filament view of the shelf. In this cross-sectional plane, the horizontal fluxes associated with the front or filament are approximately symmetric on either side of zero in a depth profile due to the symmetry of a TTW secondary circulation and due to the full-depth extent of the circulations (*i*.e., the shape of the secondary circulations presented in Section 2.5.5).

Large vertical heat fluxes on the shelf are usually attributed to breaking internal waves. Observations on the New Jersey shelf [*Shroyer et al.*, 2010] show considerable instantaneous vertical heat flux due to nonlinear internal waves, $J_q = \overline{\rho} C_p K_\rho T_z$, with observed J_q values as large as $790\ \mathrm{Wm}^{-2}$. Here, $\overline{\rho}$ is an average density; $K_\rho = \Gamma\epsilon/N^2$ is an estimated diapycnal eddy diffusivity; $\Gamma \approx 0.2$ is the turbulent mixing efficiency; ϵ is the local kinetic energy dissipation rate; C_p is specific heat capacity; and T_z is the vertical temperature gradient. The vertical heat flux due to internal waves (J_q) act to weaken the stratification via transport of surface heat through the pycnocline. The advective vertical heat flux of the fronts and filaments on the shelf (J_w) act in the opposite manner and restratify the water column $(w < 0, T' < 0)$ (for a cold filament). Both processes can be responsible for substantial vertical heat fluxes on the shelf: however, internal wave fluxes are dominant in subsurface stratified conditions while fronts and filaments typically are strongest in a more weakly stratified, near-surface layer.

2.5.7 Lagrangian material transport

The relative dispersion of Lagrangian particles depends on the Eulerian velocity wavenumber spectrum, and for flows with relatively flat spectra at the submesoscales the dispersion behavior is dominated by currents at the scale of the particle separation [*LaCasce*, 2008; *Romero et al.*, 2013]. Furthermore, the evolution of the spatial structure of particle patches (*i*.e., relative dispersion)

can thus be heavily controlled by the strong surface convergence associated with front and filaments on these daily time-scales. The control of particle trajectories by submesoscale coherent structures has been shown for cold filaments in the Gulf Stream [*Gula et al.*, 2014] and nearshore regions in the Santa Barbara Channel [*Romero et al.*, 2016]. The latter study put forth the hypothesis that the nearshore anisotropy in relative dispersion of particles can, in part, be due to the anisotropic spatial orientation of fronts and filaments closer to shore (*i*.e., the spatial geography of the submesoscale presented in Section 2.5.2). Here, we present further evidence of the ability of fronts and filaments to decrease relative dispersion and drive “self-organization" of particle patches into shapes coincident with fronts and filaments indicated by the surface convergence lines associated with secondary circulations. We also show more evidence of the diurnal cycle of secondary circulations through Lagrangian sampling of front and filament circulations.

Two types of initial particle distributions are used in this analysis. The first (‘front’ case), initializes 20,000 particles centered about a front in a circle of diameter 10 km just offshore of the SPB shelf-break (Figure 2.14a). The second (‘full-domain’ case), initializes 93,874 particles uniformly in between the 10 and 1000 m isobaths throughout the entire domain (Figure 2.14g). Both cases advect particles over the same 3- day time period. Particles are placed at the surface, neutrally buoyant, and advected only by the surface velocity field. To obtain the most accurate Lagrangian sampling of the submesoscale fields by the particles, we use 15- minute snapshot ROMS output. Sensitivity tests (not shown) indicate that model output exceeding 30 minute time intervals performs poorly for Lagrangian calculations in a submesoscale flow field.

Figure 2.14 shows the evolution of the particle positions for the front and full-domain cases. In panels (a) - (f), the particles initially distributed surrounding a front near the shelf-break collapse onto the front 25 hours after initialization due to the extreme surface convergence of the front. In Figure 2.14c,e the particle distribution matches the frontal structure, and material that was once near the shelf break is contained in a thin, elongated line that spans the cross-shore extent of the entire domain. Ultimately, the front dies and surface convergence weakens, which leads to increased separation between particles (Figure 2.14f). An analogous particle evolution is shown

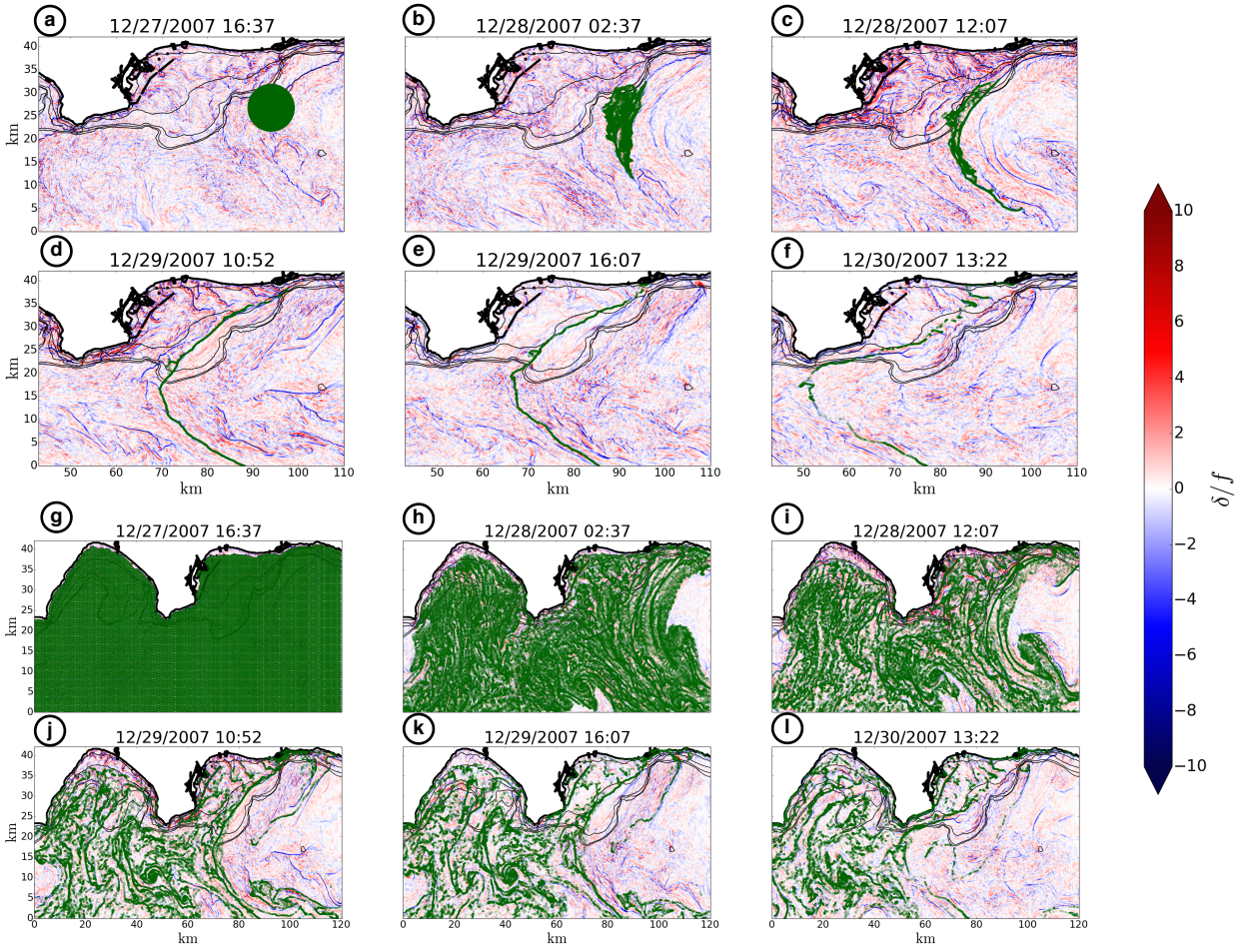

Figure 2.14: Snapshots of surface divergence (colors) and Lagrangian particle evolution for particles (green circles) for two initial particle distributions: front (a-f) and the full-domain (g-l) cases. Particles are neutrally buoyant, placed at the surface, and advected only by the horizontal surface velocity field. For the front case, 20,000 particles are initially distributed in a circle of diameter 10 km (a). For the full-domain case, 93,874 particles are initially distributed at all points offshore of the 10 m isobath. Time in between frames is uneven to highlight certain points in particle evolution. Note the extreme convergence and cross-shore elongation (from the shoreline to ~ 40 km offshore) of the particle distribution in panels (c) - (e), a direct consequence of the extreme surface convergence of the front.

for the full-domain release in Figure 2.14g-l. A uniform distribution of particles ultimately ends up in surface convergence structures (lines, curves and vortices) with some particles exiting the domain (mainly due to a bulk advection of offshore particles through the northwestern boundary by the mean offshore current) or becoming trapped on the shoreline. These snapshots indicate the daily timescale of lateral organization of material that is induced by the submesoscale flow fields. The ultimate spatial distribution of material on these daily time-scales is primarily controlled by the spatial distribution of the fronts and filaments, the advection of the fronts and filaments by larger scale flow-fields, and the location of the front or filament destruction which can cause particle separation.

Particles trapped in convergence lines of fronts or filaments sample the temporal evolution of the front or filament circulation. Figure 2.15a-d shows the mean and variance of particle-sampled surface divergence and relative vorticity (*i*.e., mean and variance over all particles of particle-coincident δ/f and ζ/f) for both the front (dark red curves) and full-domain (teal curves) cases. Particles that have exited the domain or are shoreward of the 5 m isobath are not used to calculate this mean or variance. The mean vorticity and divergence show, for both cases, an initial adjustment to particles becoming trapped in cyclonic, convergent structures followed by two diurnal peaks in both convergence and cyclonic vorticity. The variance of particle-sampled divergence and vorticity shows a similar evolution, with apparent diurnal peaks in δ/f and ζ/f variance for both particle distribution cases. Lagrangian analysis of ROMS solutions of the Gulf of Mexico show a similar diurnal evolution of particle-sampled divergence and vorticity [*Bracco et al.*, 2019].

In both cases, the strongest diurnal peaks occur during the first two cycles with a less pronounced peak in particle-sampled mean convergence on the third full-day. For the front case (red curves), the mean divergence shows a zero-crossing late in the day on December 29 (indicated by the second vertical dashed black line of that day). This is due to the death of the front itself; however, the particles still maintain their convergent, elongated shape at this time (Figure 2.14f). The magnitude of the mean vorticity and divergence is greater for the front case because the particles are isolated over a single, very strong convergence line. The diurnal peaks in these particle-sampled

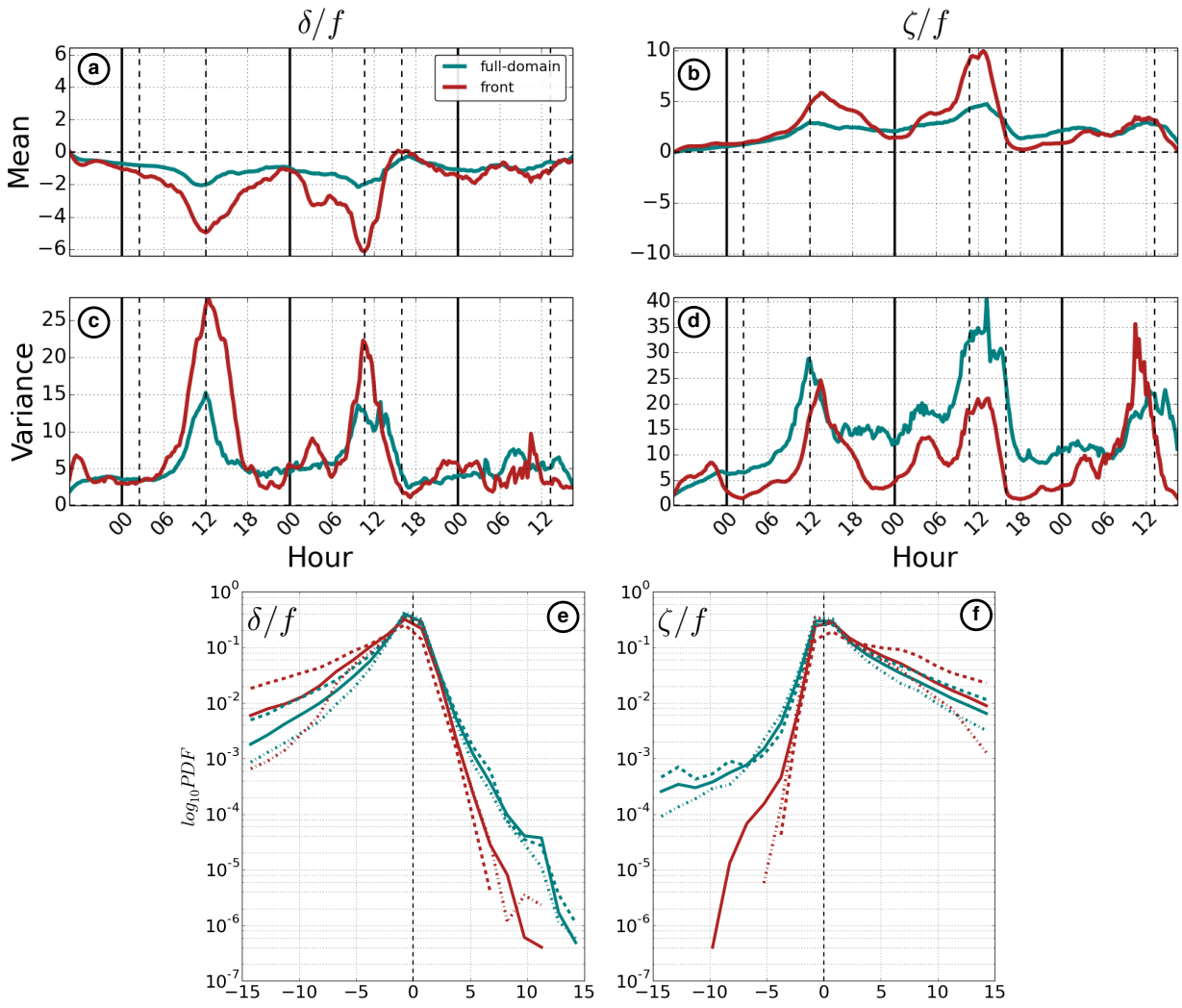

Figure 2.15: Lagrangian sampled metrics for the front (dark red) and a full-domain (teal) particle distribution cases. (a) - (d): Time series (beginning on December 27, 2007 16:37 PST) of Lagrangian sampled relative vorticity (b,d) and divergence (a,c) mean (a,b) and variance (c,d). Time series are obtained by interpolating surface fields ($\zeta/f, \delta/f$) to particle locations and taking the mean and variance over all particles at each time (particles that have exited the domain or are shoreward of the 5 m isobath are excluded from the mean and variance). Solid, vertical black lines indicate the start of a day and dashed vertical black lines indicate the times of the snapshots in Figure 2.14. (e) - (f): PDFs (log_{10}) of Lagrangian sampled divergence (e) and vorticity (f). Solid curves in (e)-(f) are PDFs obtained from fields at all time-points in the 3-day period (with $\left[N_{\text{particles}} \times 288 \text{ time points}\right]$ samples). Dashed-line PDFs represent the “late-morning" hour sampling (09:00-13:00) and dashed-dotted lines represent the “night-time" hour sampling (17:00-21:00).

metrics for divergence and vorticity indicate similar diurnal cycling of secondary circulations shown in Figure 2.12. However, the specific timing of the δ/f and ζ/f peaks (12:00 and 14:00, respectively) is different than those in Figure 2.12 (09:00 and 11:00). Reasons for this difference in phasing (*e*.g., variability in $\kappa_v(t)$ temporal structure) are investigated in Chapter 3.

PDFs of particle-sampled divergence and vorticity (Figure 2.15e,f) show that particles tend to be trapped by submesoscale coherent structures on the whole. For both releases, the PDFs are skewed towards negative divergence and cyclonic vorticity (solid lines). This skewness is more exaggerated when the sampling points are taken to be only in the late-morning (dashed lines), defined as 09:00-13:00, and less exaggerated when sampling points are taken to be in the night (dashed-dotted lines), defined as 17:00-21:00. Again, this metric indicates that surface material, on daily time-scales, is trapped in submesoscale structures of strong surface convergence and strong cyclonic vorticity. The strength of this convergence and vorticity exhibits a diurnal cycle that peaks in the late morning, signifying a transient response of secondary circulation to $\partial\kappa_v/\partial t \neq 0$. This diurnal signal is captured in the full-domain case (Figure 2.15, teal curves) where particles are sampling flow fields on and off the shelf; the diurnal evolution of vorticity and divergence is likely to be similar between shelf and open-ocean submesoscale currents.

2.6 Summary, Conclusions, and Prospects

The existence of submesoscale variability (in the form of fronts, filaments, and vortices) on the shelf is shown through a numerical simulation of the Southern California Bight with horizontal resolution $\Delta x = 75$ m. Fronts and filaments defined by large horizontal buoyancy gradients coincident with strong surface convergence and cyclonic vorticity are ubiquitous on the shelf with lifetimes on the order of days. No paradigms previously used to describe shelf-circulation predict the existence of this phenomena. These spontaneously formed and short-lived submesoscale density gradients differ in dynamical classification (Ro $>>$ 1) and evolution from the persistent

and geographically constrained shelf-break and tidal-mixing fronts that are commonly found on some continental shelves. Submesoscale currents on the shelf are frequently in contact with the sea floor; the shallow depth of the shelf is the primary source for differences in the phenomenology of open-ocean and shallow-water submesoscale dynamics. This study attempts to characterize the submesoscale regime on the shelf, and as such, raises a number of questions for further investigation.

Colder atmospheric temperatures along with more frequent storms lead to a less stratified shelf relative to other times of year. On some shelves with very strong storms or cooling the winter stratification disappears entirely (*e*.g., off New England), unlike in the SCB where a pycnocline is always present over most of the shelf. *Callies et al.* [2015] observe a seasonal cycle in submesoscale turbulence in the Gulf Stream, with stronger submesoscale activity in the winter months due to decreased stratification and deeper surface mixed layers. It is possible that the low-stratification associated with the winter-spring months of the L3 solution may lead to an over-representation of the submesoscale activity relative to summer months when stratification is higher. However, further investigation into the seasonality of shallow-water submesoscale variability is warranted given the BBL whose vertical mixing (and thus TTW secondary circulations) can potentially induce frontogenesis in the absence of surface cooling.

Generally, there is stronger submesoscale variance (indicated by ζ/f, δ/f variance) on the shelf relative to offshore. The shelf submesoscale variance is diminished inshore of $\sim$ 10 m isobath in our simulation. However, this result should be re-addressed with submesoscale-resolving simulations that include an active surf-zone. The coastal submesoscale geography is influenced by the local bathymetry and shape of the coastline. Shallow-water ($h \sim O(10$ m)) fronts and filaments show a preference for longitudinal alignment parallel to isobaths. This preference is less pronounced as depth increases with essentially isotropic orientations offshore. Headlands are sites of extreme vorticity variance and can act as the source point for submesoscale structure generation in a bay.

The formation mechanisms responsible for creating submesoscale gradients on the shelf are distinct from the mechanisms responsible for creating tidal-mixing and shelf-break fronts. Similar to their open-ocean analogs, horizontal advection is the dominant process responsible for increasing and elongating submesoscale density and velocity gradients on the shelf. However, local bathymetry can greatly influence formation. We present a case of a headland wake as an example of these two controls: coastline influenced cyclonic vorticity generation combined with frontogenesis dominated by horizontal advection. The fraction of coastal submesoscale activity due to shelf-specific controls on formation (creation of straining flows by topographic steering and frontogenisis from headland wake formation) or more general mechanisms that are perennially present in the open-ocean regime (frontogenesis by mesoscale straining flows or secondary circulations in a turbulent boundary layer and mixed layer instabilities) remains to be quantified.

The transverse structure of shelf fronts and filaments exhibit less transverse symmetry compared to their offshore counterparts. This asymmetry is manifested in isopycnal and vertical mixing structures (*e*.g., Figure 2.9). The most likely control of the asymmetry is the interaction of full-depth boundary layers on a slope, which generally causes a decrease in vertical mixing strength closer to shore. Offshore SBLs have no such interaction with the bottom.

The quasi-steady TTW diagnostic balance matches shelf front and filament secondary circulations at times of strong vertical mixing in the SBL. However, sometimes there is a clear diurnal evolution of the secondary circulation that is not consistent with a steady model. This diurnal evolution is characterized by a transient response of front and filament circulations to abrupt changes in the vertical mixing. The response primarily appears as a phase lag between peaks in mixing and divergence. The mechanism(s) controlling the diurnal evolution of secondary circulations is investigated separately (Chapter 3).

Over a submesoscale life-cycle, the strong downwelling associated with the secondary circulation can be responsible for vertical heat fluxes on the order of 100 W/m^2 over the area occupied by the feature. These fluxes act to restratify the water column and are comparable in magnitude

to observed vertical heat fluxes associated with breaking internal waves on the New Jersey shelf that act to mix in the pycnocline. The local heat flux calculations presented in this study do not constitute a full analysis of the statistically dominant terms in the heat balance on the shelf. Rather, we have presented the general question of vertical heat fluxes and stratification on the shelf in relation to internal wave and submesoscale TTW fluxes; to what degree do submesoscale TTW fluxes set the stratification on the shelf?

The prevalence of submesoscale coherent structures on the shelf raises many obvious questions regarding their role in controlling the fate of material in the nearshore. On daily time-scales, material on the shelf is preferentially trapped into surface convergence lines associated with fronts and filaments. Submesoscale currents should certainly be added to the inventory of shelf circulations responsible for lateral fluxes on the shelf (*e*.g., internal waves, cross-shelf winds). Lagrangian particles, used to sample the velocity gradients, provide alternate evidence of the diurnal cycle of front and filament secondary circulations; this evidence is derived from particles on and off the shelf and suggests this diurnal evolution is universal to fronts and filaments regardless of total depth. The strong downwelling associated with the convergence can drive this material into the interior once it is laterally advected into the center of a front or filament.

Explicit diagnostics of submesoscale control on material dispersion has applications in ecology (*e*.g., larval dispersal) as well as coastal management (*e*.g., urban runoff and pollution). Using submesoscale-resolving ROMS solutions of the SCB shelf, *Uchiyama et al.* [2014] and *Romero et al.* [2013] show that the submesoscale regime is more responsible for the dispersion of material on the shelf than the mean currents and tides. What these studies do not diagnose, however, is the role of submesoscale variability in controlling regional connectivity [*Mitari et al.*, 2009]. High-resolution simulations of the coastal ocean provide an updated tool (relative to the $\Delta x = 1$ km solutions of *Mitari et al.* [2009]) to inform ecological frameworks (*e*.g., *Castorani et al.* [2015]) that rely on physical parameters such as oceanographic connectivity between coastal sites. Further, the general role that the nearshore submesoscale regime plays in controlling coastal connectivity patterns remains unknown and needs to be explored; is submesoscale resolution needed to

accurately assess and/or predict the fate of material in the nearshore? This question is explored in Chapter 4.

An obvious route of discovery (and validation) lies in the development of coastal observational platforms capable of better resolving submesoscale processes. Nearshore observational platforms (fast, maneuverable boats, gliders and/or planes) seeking to “hunt" short-lived shelf fronts and filaments can maximize their strike-rate by looking for temperature gradient signals across-isobaths and potentially near headlands. Along with general field campaigns aimed at gaining a bulk understanding of the submesoscale regime on the shelf, we specifically encourage the pursuit for diurnal sampling of secondary circulations. To our knowledge, the metrics shown in Sections 2.5.5 and 2.5.7 represent first realizations (numerical or real-world) of diurnal variability of front and filament secondary circulation.

CHAPTER 3

Diurnal Evolution of Submesoscale Front and Filament Circulations

3.1 Introduction

In this chapter, we extend the understanding of submesoscale coherent structures by exploring the mechanisms controlling a diurnal evolution in front and filament circulations. This diurnal variability has not been investigated in previous studies of submesoscale dynamics, yet it can impact the high- and low-frequency behavior of submesoscale circulations. These impacts on the circulation can in turn affect processes controlled by submesoscale flows (described in Chapters 1 and 2). The problem is posed in an idealized setting and uses the turbulent thermal wind (TTW or T^2W) horizontal momentum balance relation [*McWilliams et al.*, 2015; *Wenegrat and McPhaden*, 2016a] as a starting point. T^2W is a diagnostic relation that assumes a balance among rotation, pressure gradient, and vertical mixing of momentum. Front and filament circulations can be calculated from this balance with knowledge of the transverse buoyancy gradient (here, defined as b_y, where b is the buoyancy and the subscript denotes a partial derivative and y a cross-front axis) and parameterized vertical diffusivity (κ_v) profiles. For a filament, such a circulation is defined by a primarily geostrophic, cyclonically sheared longitudinal (along-filament) flow and a transverse (cross-filament) ageostrophic secondary circulation characterized by strong surface convergence and downwelling (Fig. 3.2, detailed in Section 3.2).

Relative to other frontal secondary circulation diagnostics [*Garrett and Loder*, 1981; *Nagai et al.*, 2006], T^2W is the most successful in describing the circulations of fronts or filaments with $Ro > 1$. A T^2W prediction for dense filament frontogenesis by boundary layer turbulence [*McWilliams et al.*, 2015] compares well with a Large Eddy Simulation (LES) of the same process [*Sullivan and McWilliams*, 2017]. Similarly, T^2W successfully reproduces the local circulation of individual fronts or filaments in some regional simulations (e.g., Gulf Stream cold filaments investigated in *Gula et al.* [2014]) when κ_v is strong and there is a well defined b_y.

However, in our analysis of a ROMS simulation of the Southern California Bight in Chapter 2 (adapted from *Dauhajre et al.* [2017], hereafter DMU17), we show that there is a high-frequency, diurnal evolution of submesoscale circulations with three distinct analyses. First, it is shown that individual fronts and filaments can exhibit strong secondary circulations at times of weak κ_v; these circulations are not accurately predicted by T^2W (Fig. 2.11). Further, the coincidence of strong secondary circulation and weak κ_v is characteristic of a domain-wide diurnal cycle in horizontal divergence (δ) and vertical relative vorticity (ζ) at submesoscale magnitudes ($\zeta/f, \delta/f \sim Ro = O(1)$). This domain-wide diurnal evolution is indicated by both a spatial root-mean square time-series of secondary circulation strength indicators (e.g., δ, ζ, w, where w is the vertical velocity, Fig. 2.12) and Lagrangian sampled time-series of δ and ζ, where particles are advected into fronts and filaments (Fig. 2.15).

Here we present another metric evidencing a diurnal oscillation in secondary circulations in a realistic, full primitive equation (PE), simulation. Figure 3.1 shows the diurnal evolution of vertical diffusivity, vertical velocity, and relative vorticity local to a dense filament on the Santa Monica Bay shelf over a 24-hour period. The dense filament is followed in time, and the fields local to its circulation are isolated with 3 km cross-sections that cut across the density gradient defining the filament (analysis details are given in Chapter 2). Solar heating drives a diurnal cycle in κ_v (Fig. 3.1c). Converse to the TTW prediction of strong secondary circulation (δ, w) at times of large κ_v, the strongest secondary circulation of the filament (Fig. 3.1d, dark red) occurs at a minima in $\kappa_{v_{\mathrm{RMS}}}$, with $(\zeta/f)_{\mathrm{RMS}}$ (Fig. 3.1d, dark cyan) lagging w_{RMS}.

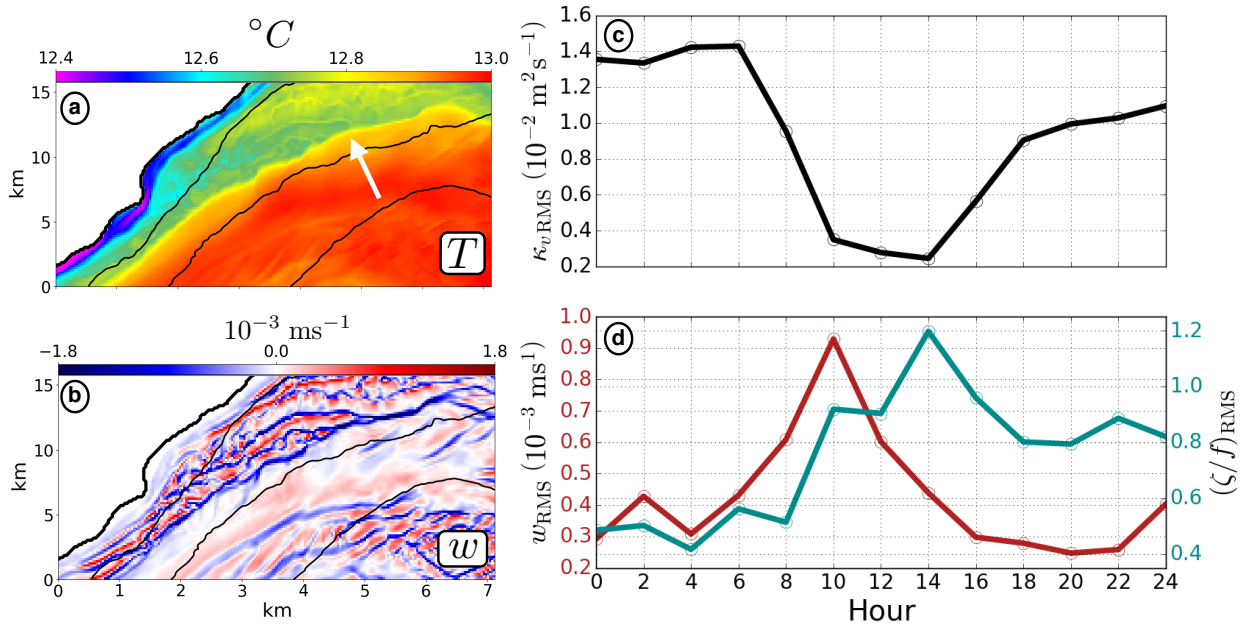

Figure 3.1: Diurnal evolution of a dense filament in a ROMS simulation of the Santa Monica Bay shelf (Filament4 in Chapter 2). (a): sea surface temperature (b): vertical velocity at z = -5 m (c): time-series of vertical diffusivity, (d): time-series of vertical velocity (left y-axis, dark red) and relative vorticity (right y-axis, dark cyan). The time-series curves in (c) and (d) are spatial (transverse-depth plane) root mean squares of the fields local to the filament over a 24-hour period. Each time-point (dots) represents a root mean square calculation from instantaneous 2-hour average of ROMS fields. The local filament fields are isolated at each time step with 3 km cross-sections across the density gradient. The root mean square in the transverse-depth plane is calculated from an average of multiple cross-sections along the longitudinal filament axis (see Chapter 2). Note the peak in vertical velocity RMS (indicative of the overall ageostrophic secondary circulation strength) at a minima in vertical diffusivity RMS, with relative vorticity lagging vertical velocity. The instantaneous fields in (a) and (b) correspond to hour 10 in the time-series.

The above two paragraphs summarize four metrics evidencing a diurnal oscillation of submesoscale circulations in a mid-latitude PE simulation. In all four analyses, the same qualitative phasing is apparent: a maxima in $|\delta|$ coincident with a minima in κ_v and with $|\zeta|$ lagging $|\delta|$. These four separate indications of a diurnal, non-T^{2}W, evolution in secondary circulations motivate investigation of the mechanism(s) controlling the diurnal evolution, the high-frequency and diurnally averaged effects on the circulation by transient oscillations, and the implications

of this diurnal variability on submesoscale controlled processes (e.g., vertical fluxes in the boundary layer).

In this study, the basic physics driving the diurnal variability in front or filament circulation are explained with a modified T^2W system that includes acceleration, which we call the Transient Turbulent Thermal Wind (T^3W) system. The dynamical target is a mid-lifecycle submesoscale density front or filament (after frontogenetic birth and before frontolytic destruction) in the surface boundary layer with $\mathrm{Ro}, \mathrm{Fr} \sim 1$ and where the Ekman number $\left(\mathrm{Ek} = \kappa_v / f h_{\mathrm{sbl}}^2\right)$ fluctuates in magnitude over a diurnal period (here, h_{sbl} is the surface boundary layer depth). Our goal is to understand the mechanism(s) that cause temporal evolution of front or filament circulation forced by a diurnal variation in solar heating or wind stress, the extent of the disagreement between T^2W and T^3W solutions, and the effect of the transient evolution on the low-frequency strength of the secondary circulation. We are motivated by the simple question: why is there such strong $|\delta|$ when κ_v is weak in fronts and filaments? Further, is the diurnal evolution of the secondary circulation distinct or universal for different forcing regimes or geographical settings? Our analysis will expand on the success of the T^2W system in describing high-Ro submesoscale front and filament circulations [*Gula et al.*, 2014; *McWilliams et al.*, 2015; *Wenegrat and McPhaden*, 2016a; *Dauhajre et al.*, 2017], with this study correcting an apparent predictive limit of the T^2W balance during periods of high-frequency temporal variability in κ_v.

This chapter introduces the T^3W equations as a 2-D (y, z)-system that captures the relevant spatial structure of a front or filament circulation and accurately predicts the phasing and strength of secondary circulations under diurnal surface forcing observed in Fig. 3.1 (Section 3.2 and 3.3). However, the fundamental mechanisms controlling the diurnal evolution of the 2-D circulation are shown to operate in independent, 1-D vertical columns responding to temporal changes in κ_v (Section 3.4). As such, this study adds and overlaps with the literature on the upper ocean response to diurnal fluctuations in vertical diffusivity [*McWilliams et al.*, 2009c; *Price et al.*, 1986; *Wenegrat and McPhaden*, 2016b], but it represents a particular, unexplored case of 1-D Ekman layer dynamics translating to coherent 2-D circulation structures. Our analysis will reveal and quan-

tify the important role of both inertial and diffusive mechanisms in the 1-D system and expose when, why, and with what magnitude differences between T^2W and T^3W solutions arise. In Section 3.5 we will show that the phasing of δ and ζ in fronts and filaments observed in two ROMS simulations (southwestern Pacific and coastal California) exhibits regional sensitivities that are predicted by the 1-D model. We conclude with a summary and discussion of results in Section 4.6.

3.2 The Transient Turbulent Thermal Wind (T^3W) System

3.2.1 Turbulent Thermal Wind balance

We pose the transient turbulent thermal wind equations starting with the diagnostic, turbulent thermal wind momentum balance [*McWilliams et al.*, 2015; *Wenegrat and McPhaden*, 2016a; *McWilliams*, 2017] introduced in Chapter 2 (but defined again here for context with the T^3W system, Section 3.2.2). T^2W is contained within the hydrostatic primitive equations and combines geostrophic, Ekman, and hydrostatic dynamics to give a diagnostic relation for front and filament circulation:

$$f\hat{\boldsymbol{z}} \times \boldsymbol{u}_h = -\nabla_h \phi + \frac{\partial}{\partial z}\left(\kappa_v \frac{\partial \boldsymbol{u}_h}{\partial z}\right), \tag{3.1a}$$

$$\nabla_h \cdot \boldsymbol{u}_h + \frac{\partial w}{\partial z} = 0, \tag{3.1b}$$

where x and y are the longitudinal and transverse axes, respectively. The horizontal velocity vector is $\boldsymbol{u}_h = u\hat{x} + v\hat{y}$, f the Coriolis parameter, κ_v the vertical diffusivity associated with boundary layer turbulence, and $\phi = p/\rho_0$ the pressure normalized by a reference density (ρ_0).

For the problems presented in this study, we assume a rigid-lid and a finite-depth. These constraints require an assumption regarding the barotropic component of the pressure field in (3.1) that we detail in the Section 3.2. Hydrostatic vertical momentum balance ($\partial\phi/\partial z = b = -g\rho/\rho_0$)

and specified density and vertical diffusivity profiles can be used in (3.1) to give an estimate of front or filament circulation $(\boldsymbol{u}_h, w)$. [1]

Given a $\nabla_h b$ and κ_v, (3.1) is capable of producing the defining characteristics of a submesoscale flow structure, illustrated in Fig. 3.2. In this example, the buoyancy structure (dashed lines) shows the dense filament structure: lighter fluid at the surface, with the transverse buoyancy gradient confined to the surface boundary layer (SBL, $z < -h_{\text{sbl}}$) where strong vertical diffusivity (not shown) limits stratification (implied in the illustration is an assumption of longitudinal uniformity, $\partial/\partial x = 0$). The associated T^2W circulation is composed of a primarily geostrophic, vertically sheared longitudinal jet that gives rise to cyclonic vorticity at the filament center and an ageostrophic secondary circulation (black streamlines) with surface convergence and downwelling at the filament center.[2]

It is important to note that (3.1a) can be solved in individual vertical columns. In this manner, the horizontal structure of filament (or front) circulation (*e*.g., left panel Fig. 3.2) results from adjacent 1-D T^2W solutions that are dependent on individual vertical profiles $b_y(z)$ and $\kappa_v(z)$. Two examples of 1-D T^2W profiles are shown in the right panels of Fig. 3.2 illustrating day (top, $\text{Ek} \sim 10^{-1}$) and night (bottom, $\text{Ek} \sim 10^{-2}$) T^2W predictions.

The profiles at large Ek (Fig. 3.2, top right) are typical of a mid-latitude dense filament ($\kappa_v \approx 3 \times 10^{-2}$ m^2s^{-1}, $h_{\text{sbl}} \approx 50$ m, $f_0 \approx 8 \times 10^{-5}$ s^{-1}). The longitudinal geostrophic flow (u_g) is eastward and decays with depth by thermal wind balance. The ageostrophic flow u_a, v due to $\kappa_v(z)$ is a clockwise Ekman spiral: v (u_a) is positive (negative) at the surface and negative (positive) at the base of the boundary layer. The total longitudinal flow (u) is reduced in magnitude from the geostrophic component (u_g) by the ageostrophic component (u_a) that is driven by the strong ver-

[1] Equation (3.1) is not a complete representation of a diagnostic balanced model for front or filament circulation. To satisfy balance, an Omega equation is also needed that accounts for geostrophic tendency, advection, and the dynamical effect of interior stratification to correct the w calculated from (3.1) [*McWilliams*, 2017].

[2] A warm (light) filament would have the opposite T^2W circulation (surface divergence and upwelling), although these features are short-lived and not as ubiquitous as their cold counterparts. Thus, we focus on a dense filament in this study.

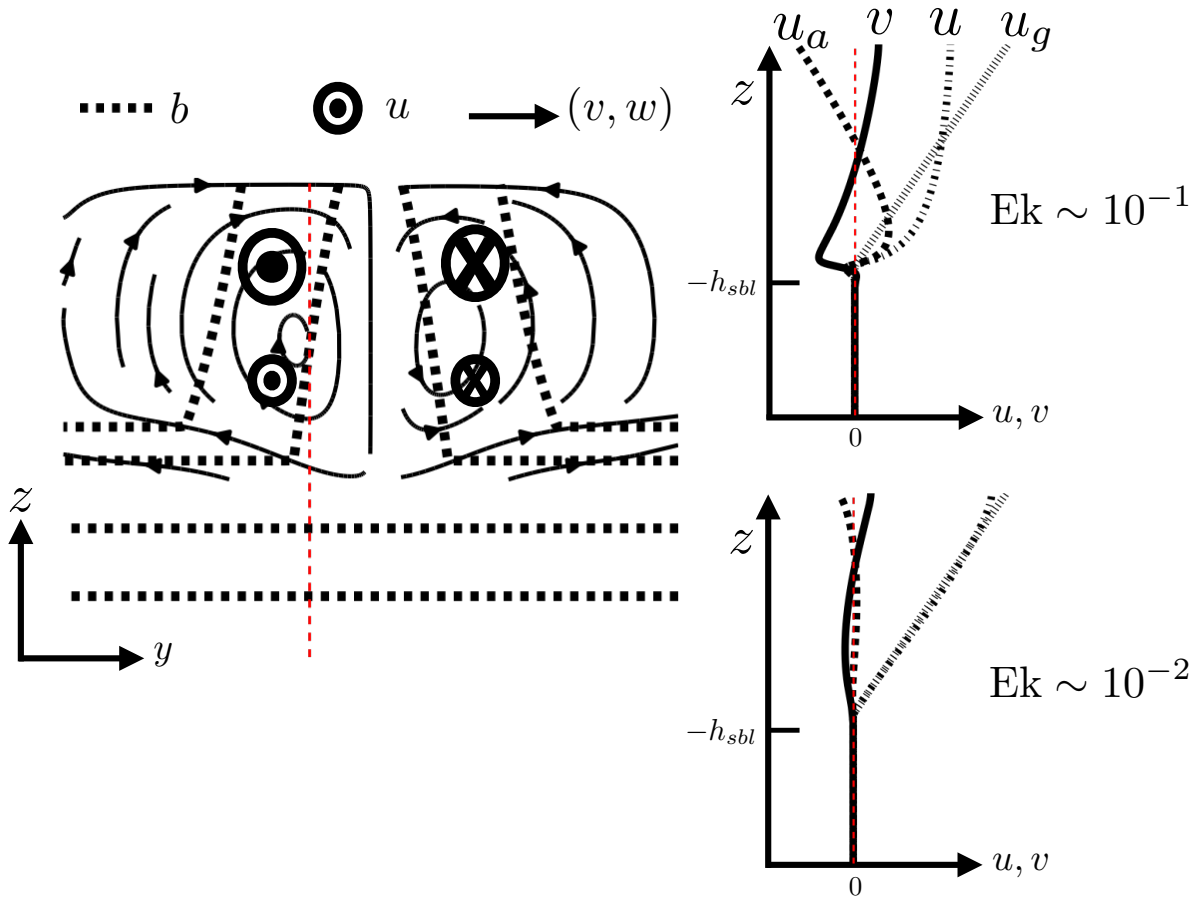

Figure 3.2: Schematic of 2-D T^{2}W circulation in a surface boundary layer, open-ocean dense filament (left) and corresponding 1-D velocity profiles (right) at a horizontal location (dashed red line in 2-D plane) at large (top right) and small (bottom right) Ekman number $\left(\text{Ek} = \kappa_v / f_0 h_{\text{sbl}}^2\right)$ Left: Transverse-depth (y, z)-plane view of a dense filament. The filament (density) structure is indicated by the black dashed lines. The buoyancy gradient, combined with boundary layer vertical diffusivity (not shown) gives rise to a T^{2}W circulation: longitudinal flow (u, where $u > 0$ is out of the page) and a secondary circulation (arrows, (v, w)) that is entirely ageostrophic. Below the surface boundary layer, the vertical diffusivity is negligible, the buoyancy gradient zero, and the T^{2}W flow quiescent. Right: 1-D T^{2}W velocity profiles at large (top) and small (bottom) Ekman numbers: transverse velocity (v) and longitudinal flow (u), with the ageostrophic (u_a) and geostrophic (u_g) components of the longitudinal flow shown (v is entirely ageostrophic here). The diagnostic T^{2}W relation predicts that at larger Ek, u_a and v are larger in magnitude and at smaller Ek, $u \approx u_g$ and u_a, v much weaker.

tical diffusivity. At lower Ek (weak κ_v), T^{2}W reverts to near thermal wind balance $\left(u \approx u_g\right)$ with the ageostrophic flows u_a and v much weaker. Due to the symmetric structure of the filament (or a front), δ and ζ at the filament center can be thought of as proportional to the magnitudes of the 1-D velocities, *i.e.*, $\delta \propto 2v/\Delta y$, where $v = v(z)$ is a 1-D TTW profile. We will rely on this assumption in Section 3.4.4, 3.5 to translate 1-D ageostrophic dynamics back to the 2-D circulation.

McWilliams [2017] derives a scaling estimate for the strength of the (overturning) secondary circulation (Φ) based on the diagnostic T^{2}W system:

$$\Phi \sim \frac{\kappa_{v_{max}} \max\left[|b_y|\right]}{f^2}, \quad \text{or} \quad \Phi \sim \frac{\kappa_{v_{max}} \max\left[|u_g|\right]}{f h_{\text{sbl}}}, \tag{3.2}$$

where b_y is the transverse buoyancy gradient with associated geostrophic flow u_g. Either large b_y, large κ_v, or small h_{sbl} produce strong secondary circulation overturning cells. (3.1) and (3.2) are accurate in predicting the general structure and strength of front or filament circulation in a quasi-steady balance. Yet, the primary motivation of this study is based on observations in realistic submesoscale simulations that contradict (3.2) in the diurnal phasing of the circulation: strong $\Phi \propto |\delta|, |w|$ at weak κ_v (Fig. 3.1).

3.2.2 T^{3}W governing equations

Here, we introduce time-memory to (3.1) to form the 2-D transient turbulent thermal wind (T^{3}W) system. T^{3}W is posed in a transverse-depth (y, z)-plane under the assumption of longitudinal uniformity along a front or filament ($\frac{\partial}{\partial x} = 0$, which excludes frontal instabilities other than symmetric). T^{3}W builds on (3.1) by adding time-derivatives to the momentum equations and accounting for buoyancy evolution by advection and vertical eddy diffusion. These are the simplest *a* priori additions to T^{2}W that allow time-memory. The hydrostatic assumption can be justified in solutions that are scale anisotropic ($H/L << 1$, where H and L are vertical and horizontal scales, respectively). In the solution shown in Section 3.3, surface and bottom boundary layer depths ($h_{\text{sbl}}, h_{\text{bbl}}$) and vertical eddy diffusivities for momentum (κ_v) and buoyancy (κ_b) are pa-

rameterized with a K-Profile Parameterization (KPP) [*Large et al.*, 1994; *McWilliams et al.*, 2009c]. [3]

Momentum advection is not included for simplicity, and the buoyancy advection allows some frontogenesis to occur, although less than if momentum advection were retained. In highly frontogenetic situations, momentum advection does play a significant role [*McWilliams*, 2017], but this is not the situation being addressed in this study. Non-linear dynamics due to momentum advection can potentially cause variability in secondary circulation over a diurnal period (e.g., by the non-linear Ekman transport effect [*Wenegrat and Thomas*, 2017] or by a favorably aligned, oscillating wind-stress [*McWilliams*, 2017]), however, we do not explore such effects in this study.

The 2-D T^{3}W system is given by

$$\frac{\partial u}{\partial t} - fv = \frac{\partial}{\partial z}\left(\kappa_v \frac{\partial u}{\partial z}\right), \tag{3.3a}$$

$$\frac{\partial v}{\partial t} + fu = -\frac{\partial \phi}{\partial y} + \frac{\partial}{\partial z}\left(\kappa_v \frac{\partial v}{\partial z}\right), \tag{3.3b}$$

$$\frac{\partial \phi}{\partial z} = b, \tag{3.3c}$$

$$\frac{\partial b}{\partial t} + v\frac{\partial b}{\partial y} + w\frac{\partial b}{\partial z} = \frac{\partial}{\partial z}\left(\kappa_b \frac{\partial b}{\partial z}\right), \tag{3.3d}$$

$$\frac{\partial v}{\partial y} + \frac{\partial w}{\partial z} = 0. \tag{3.3e}$$

Definitions are as in (3.1) with u, v, w velocities in the x, y, z directions respectively, f assumed constant in y, $\rho_0 = 1027.5$ kgm^{-3}, and $g = 9.8$ ms^{-2}.

Vertical boundary conditions for momentum are

$$\kappa_v \frac{\partial \boldsymbol{u}_h}{\partial z} = \frac{\boldsymbol{\tau}^s}{\rho_0} \quad \text{at } z = 0, \qquad \kappa_v \frac{\partial \boldsymbol{u}_h}{\partial z} = \frac{\boldsymbol{\tau}^b}{\rho_0} \quad \text{at } z = -H, \tag{3.4}$$

[3] *McWilliams et al.* [2009c] and *Durski et al.* [2004] find that KPP is suitable for diurnal forcing and finite-depth application, respectively. Previous T^{2}W investigations utilize KPP in idealized [*McWilliams et al.*, 2015; *McWilliams*, 2017] and more realistic settings [*Gula et al.*, 2014].

and buoyancy

$$\kappa_b \frac{\partial b}{\partial z} = \frac{g\alpha Q_s}{\rho_0 C_p} \qquad \text{at } z = 0\,, \qquad \kappa_b \frac{\partial b}{\partial z} = 0 \qquad \text{at } z = -H\,, \tag{3.5}$$

where $\boldsymbol{\tau}^s, \boldsymbol{\tau}^b$ represent surface and bottom stresses respectively. $\alpha = 2 \times 10^{-4}$ is a thermal expansion coefficient, Q_s is a surface heat flux (in Wm^{-2}), and $C_p = 3985\ \mathrm{Jkg}^{-1}\mathrm{K}^{-1}$ is a specific heat capacity. The bottom stress is computed as a bottom-layer quadratic drag law,

$$\boldsymbol{\tau}^b = \frac{\rho_0 \kappa^2 |\boldsymbol{u}_b| \boldsymbol{u}_b}{\ln\left(z_b / z_0^2\right)}\,, \tag{3.6}$$

where $\boldsymbol{u}_b$ is the velocity vector at the bottom; $\kappa = 0.41$ is von Karman's constant, z_b is the height above the bottom (mid-point of the bottom grid cell, see supplemental information of *Dauhajre and McWilliams* [2018]); and $z_0 = 10^{-2}\mathrm{m}^2$ is a roughness length. The vertical velocity is obtained from vertical integration of the continuity equation with a rigid-lid assumption.

A diagnostic barotropic pressure equation is used to compute $\partial\phi/\partial y$ and is derived by taking the divergence of the vertically averaged horizontal momentum equations (with an assumption of constant depth in y):

$$\frac{\partial}{\partial t}\left(\frac{\partial \overline{v}^H}{\partial y}\right) + f\frac{\partial \overline{u}^H}{\partial y} = -\frac{\partial^2 \overline{\phi}^H}{\partial y^2} + \frac{1}{\rho_0 h}\frac{\partial}{\partial y}\left(\tau_y^s - \tau_y^b\right). \tag{3.7}$$

The overbarred variables in (3.7) denote the barotropic fields. That is, for any variable $q(z)$:

$$q(z) = \widetilde{q}(z) + \left(\overline{q}^H - \overline{\widetilde{q}}^H\right)\,, \tag{3.8}$$

where the ^{H} indicates a vertical average and variables with a tilde represent a calculated baroclinic component, *e*.g.,

$$\widetilde{\phi} = \int_{-z}^{0} b\,dz\,. \tag{3.9}$$

With the rigid-lid assumption, $\partial \overline{v}^H/\partial y = 0$ from continuity, and (3.7) becomes a diagnostic relation for $\overline{\phi}^H$:

$$\frac{\partial^2 \overline{\phi}^H}{\partial y^2} = -f\frac{\partial \overline{u}^H}{\partial y} + \frac{1}{\rho_0 H}\frac{\partial}{\partial y}\left(\tau_y^s - \tau_y^b\right)\,. \tag{3.10}$$

The total pressure is then obtained by correcting the baroclinic pressure $\left(\widetilde{\phi}\right)$ by (3.8). [4] Equations (3.3) and (3.10) are solved numerically and details of the spatial-temporal discretization are given in the supplemental information of *Dauhajre and McWilliams* [2018] (model code can be found at: `https://github.com/ddauhajre/T3W_DIM_MODEL`).

3.3 Diurnal Evolution of a 2-D Dense Filament

Here, we show the success of (3.3) in capturing the diurnal variability in a 2-D front or filament circulation. We will also show that the primary diurnal behavior is retained in a simplified, 1-D version of (3.3) that is explored in Section 3.4 and validated against ROMS data in Section 3.5. The reduction in dynamical complexity is justified with two solutions: one solution (FIL1) contains as much dynamical complexity as allowed in (3.3). The vertical diffusivity contains spatial structure, is parameterized by KPP (along with boundary layer depths) and is forced by a diurnal heat flux $Q_s = -Q_0 \cos 2\pi t/T$, (where $T = 1$ day and $Q_0 = 100$ Wm^{-2}) and a constant wind-stress $\tau_y^s = 0.02$ Nm^{-2}. Also, in FIL1, the buoyancy field evolves due to vertical diffusivity of buoyancy and advection. A second solution (FIL2) employs the following simplifications: vertical diffusivity is spatially uniform and prescribed ($\kappa_v(y,z,t) = \kappa_v(t)$), there are no surface stresses or fluxes $\left(\boldsymbol{\tau}^s, \boldsymbol{\tau}^b = 0\right)$, and buoyancy advection is turned off $\left(vb_y + wb_z = 0\right)$.

FIL1 and FIL2 are simulated at mid-latitude ($f = 8 \times 10^{-5} s^{-1}$) to allow a qualitative comparison with the observation from Southern California in Fig. 3.1. The initial condition creation and model spin-up for case FIL1 is described in the chapter supplement (Section 3.7.1). To allow a consistent comparison between the cases, FIL2 is initialized with the buoyancy field of case FIL1 after a 4-day spinup period during which buoyancy advection has altered the idealized $b(y,z,t=0)$.

[4] If the T^{2}W relation is used to diagnose flows from a full primitive equation model (*e.g.*, as in *Gula et al.* [2014] or DMU17), the full pressure field is known and can be used directly as an input into (3.1). However, if idealized T^{2}W solutions are being created from prescribed b and κ_v in finite depth with a rigid lid (as they are in this study), $\widetilde{\phi}$ is taken from b, and $\overline{\phi}^H$ is computed from a $\overline{u}^H$ that is derived from a thermal wind relation with the prescribed b. In this sense, a T^{2}W initial condition can be created from an initially prescribed b, κ_v.

Similarly, the magnitude of $\kappa_v(t)$ in case FIL2 is taken as a spatial average of the parameterized $\kappa_v(y, z, t)$ in case FIL1. We show FIL1 2 days after the spin-up procedure, where the solution exhibits approximate periodicity (there is a low-frequency trend in $\partial b/\partial y$ by the secondary circulation advection). FIL2 has no such trend.

After the 4-day spin-up, the dense filament is within a submesoscale parameter space with a local mean $\mathrm{Ro} = \zeta/f = 0.8$ and $\mathrm{Fr} = \partial_z\sqrt{u^2 + v^2}/N = 0.9$ for FIL1, where the mean is taken over a diurnal period in the 2 km surrounding the filament center and in upper-half of the water column.

3.3.1 FIL1 diurnal evolution

Figure 3.3 shows the evolution of $b, \kappa_v, \zeta/f, \delta/f$, and secondary circulation streamlines for FIL1 over a 24-hour period. Strong κ_v and overlapping h_{sbl} (gray line) and h_{bbl} (orange line) at the filament center are present at 00:00 (Fig. 3.3, first column). At 09:00, surface heating increases stratification that causes κ_v to decrease in magnitude. Yet, $|\delta/f|$ reaches its maxima at 09:00 (Fig 3.3 bottom). Lateral buoyancy advection associated with stronger δ/f at 09:00 sharpens b_y at the surface and widens b_y at the bottom (Fig. 3.3 first row). At 18:00, h_{sbl} and h_{bbl} separate and shrink towards the surface and bottom, respectively, as the heating continues. $|\zeta/f|$ is strongest at 18:00, with some spatial deformation resulting from the evolution of the buoyancy ($b_{yy} \propto \zeta$). The effect of this deformation also imprints onto the secondary circulation as seen in δ/f and the streamlines of the secondary circulation. Domain-wide $|\delta/f|$ is much weaker at 18:00, relative to 09:00. Cooling begins after 18:00, and the fields evolve back to a similar state as in 00:00. The qualitative phasing of δ, ζ in the FIL1 solution agrees with the observations in DMU17 and Fig. 3.1.

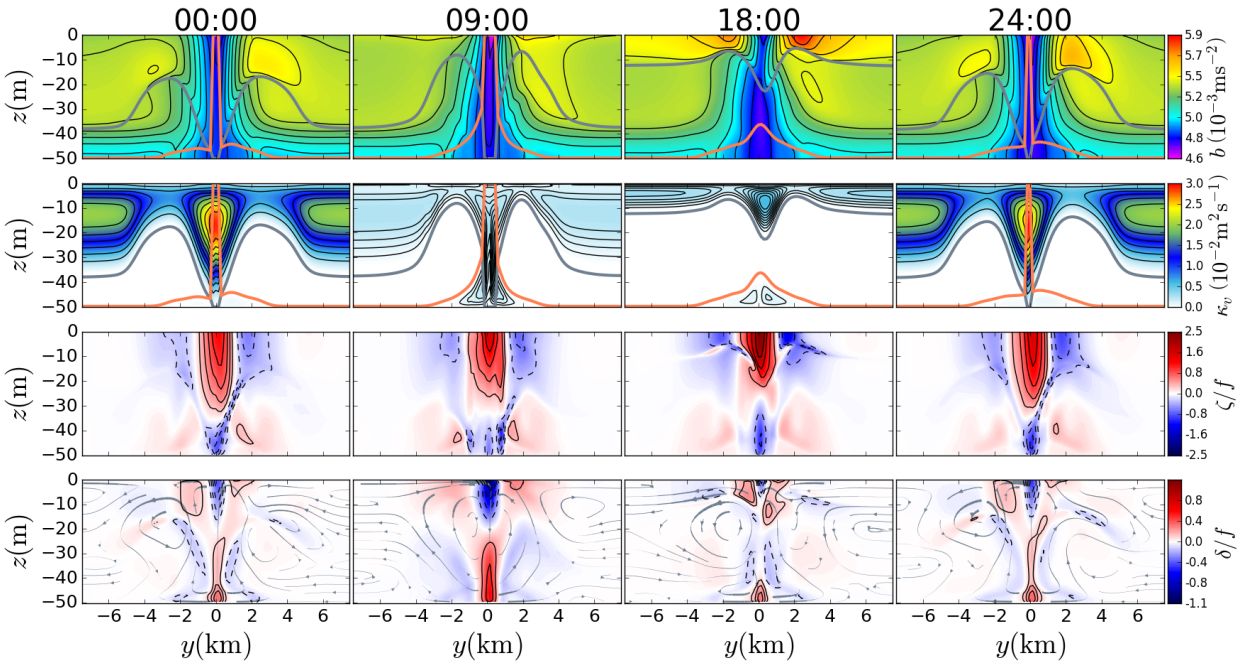

Figure 3.3: (y, z) evolution of fields for case FIL1 over a diurnal period (4 days after initialization). Snapshots in time (columns) of b (top row), κ_v (second row), ζ/f (third row) and δ/f (bottom row) with the secondary circulation indicated by the grey streamlines. h_{sbl} and h_{bbl} thicknesses are plotted as gray and orange lines, respectively, in the first and second row. Note the maxima in surface convergence at 09:00, coincident with weak vertical diffusivity.

3.3.2 Diurnal behavior retained in 1-D

Figure 3.4 shows a two-day RMS time-series of κ_v, u, v, ζ/f, and δ/f for FIL1 (solid) and FIL2 (dashed). The RMS for any field q is denoted by $\langle q \rangle$, and denotes the (y, z) RMS normalized by its standard deviation in time. $\langle \kappa_v \rangle$, $\langle u \rangle$, $\langle v \rangle$, $\langle \zeta/f \rangle$, and $\langle \delta/f \rangle$ are periodic at this stage in their respective simulations. In Fig. 3.4f we show the T^{3}W (salmon) and T^{2}W (maroon) $\langle \delta/f \rangle$ to compare instantaneous differences between the prognostic and diagnostic predictions of the secondary circulation. The diagnostic T^{2}W solution at each time-step is calculated with the $b(y, z, t)$, $\kappa_v(y, z, t)$, and $\overline{u}^H(y, t)$ from the T^{3}W solution, where $\overline{u}^H$ is used in (3.10) to compute $\overline{\phi}^H$.

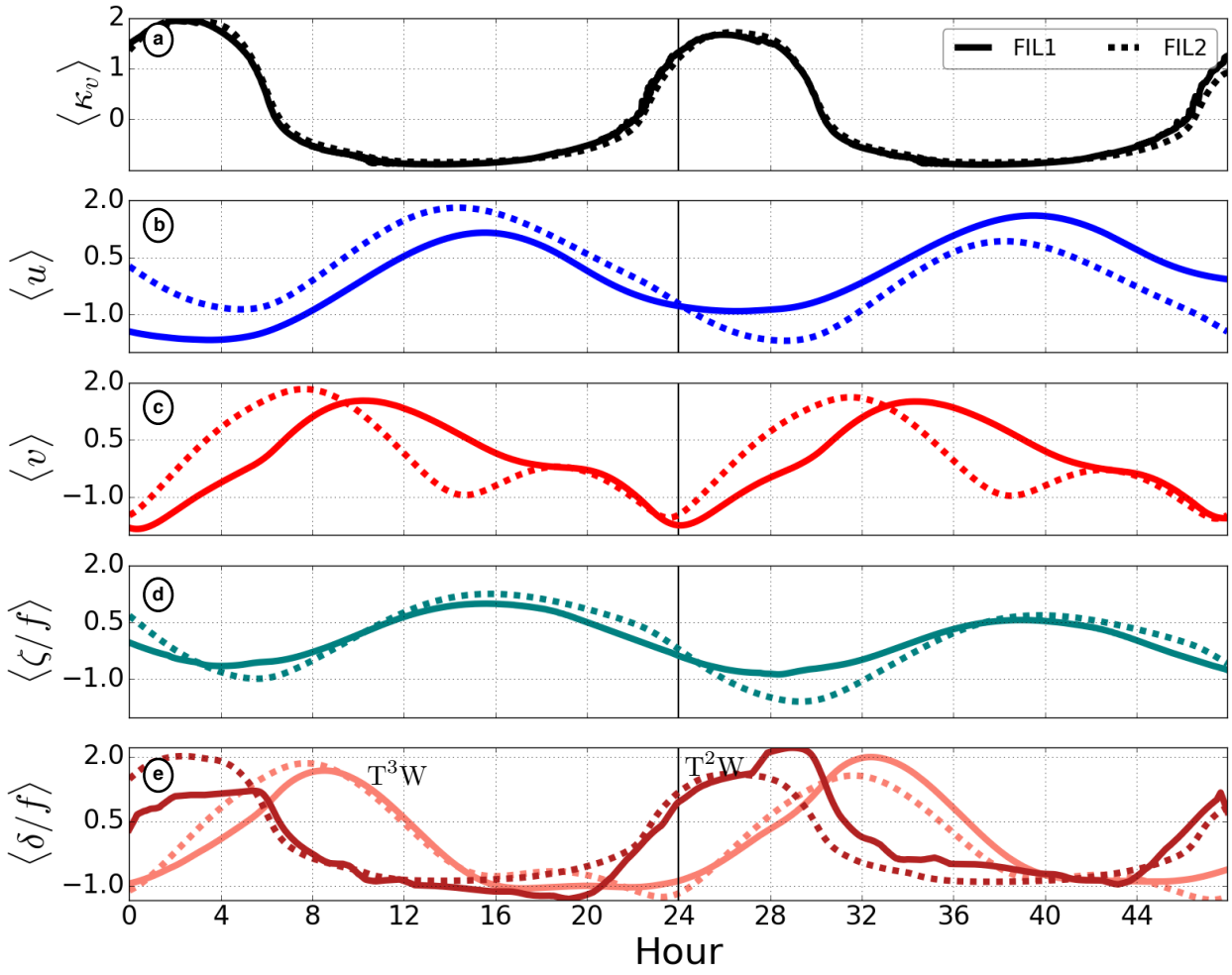

Figure 3.4: Two-day time-series of the normalized spatial RMS of fields for the cases FIL1 (solid) and FIL2 (dashed) solutions. (a) κ_v, (b) u, (c) v, (d) ζ/f, and (e) δ/f. In (e), the T^{2}W solution is shown in dark red and the T^{3}W solution in salmon. Vertical black lines separate days. Each spatial RMS for a variable is normalized by its standard deviation in time, denoted by the symbol $\langle . \rangle$. $\langle \zeta/f \rangle$ has been de-trended to remove the effect of a trend in $\partial b/\partial y$ for each case. Some temporal (boxed window) smoothing has been done on the T^{2}W FIL1 $\langle \delta/f \rangle$ (solid maroon). The time-series begins at 00:00 in Fig. 3.3.

The T^{2}W prediction (Fig. 3.4f, maroon curves) of the secondary circulation in both cases disagrees with the respective transient solution in its phasing. The diagnostic prediction primarily follows $\langle \kappa_v \rangle$, as dictated by (3.2), even in FIL1, where b_y is not constant in time. FIL2 has no b_y modulation by advection (as well as constant h_{sbl}, h_{bbl} and spatially uniform κ_v). Yet, the phasing of the RMS fields for FIL1 and FIL2 are extremely similar. In both cases, $\langle v \rangle$ (Fig. 3.4c) peaks with a minima in

$\langle \kappa_v \rangle$ (Fig. 3.4a) and $\langle u \rangle$ (Fig. 3.4b) lags $\langle v \rangle$. The secondary circulation strength, indicated by $\langle \delta / f \rangle$ (Fig. 3.4e), is very similar in both cases with a maxima around 08:00 each day coincident with a minima in κ_v. Because b_y is not changing in FIL2, the agreement between FIL1 and FIL2 indicates that ageostrophic accelerations are controlling diurnal phasing. Again, note the agreement in phasing between the simple 2-D and 1-D systems in Fig. 3.4 and the realization from a realistic, PE simulation in Fig. 3.1. The transient oscillations in the secondary circulation are instanteously stronger than the T^2W flow at times of weak mixing, however, the diurnal average (not shown) of the secondary circulation is weaker in a T^3W solution relative to T^2W. This averaged weakening is analogous to diurnal Ekman layer rectification [*McWilliams et al.*, 2009c; *Wenegrat and McPhaden*, 2016b] where the "effective" vertical eddy diffusivity in the diurnally averaged transient solution is reduced relative to a steady-state.

3.4 1-D Controlling Mechanisms

3.4.1 1-D T^3W governing equations

To isolate the fundamental mechanism controlling diurnal variability of front or filament circulation we simplify (3.3) and isolate the ageostrophic flow. We decouple the momentum and buoyancy equations in (3.3) by assuming $b_z = 0$, subtract out the geostrophic component, and assume $\kappa_v(z,t) = \kappa_v(t)$ (and constant h_{sbl} in time):

$$\begin{pmatrix} u \\ v \end{pmatrix}_t + f \begin{pmatrix} -v \\ u \end{pmatrix} = \kappa_v(t) \begin{pmatrix} u \\ v \end{pmatrix}_{zz} , \tag{3.11}$$

where now, $u = u_a$.

The boundary condition enforces geostrophic shear at the surface and bottom of the surface

boundary layer ($h_{\text{sbl}} = H$) for u and a free-slip condition at the surface and bottom for v:

$$\kappa_v u_z = -\kappa_v \left(u_g\right)_z \quad \text{at} \quad z = 0\,, -H \tag{3.12a}$$

$$\kappa_v v_z = 0 \quad \text{at} \quad z = 0\,, -H\,, \tag{3.12b}$$

where the geostrophic longitudinal shear $\partial u_g/\partial z = -b_y/f$. The problem can be analogously posed with a no-slip condition at the bottom (not shown), which produces the same general solution behavior. We note, this system has been studied in the atmospheric context [*Zhang and Tan*, 2002; *Wiel et al.*, 2010] and more recently explored for the oceanic boundary layer [*Wenegrat and McPhaden*, 2016b]. Although, here, we use a free slip boundary condition and geostrophic relation at the boundary as opposed to a surface wind stress. We will also use a flow decomposition and non-dimensional framework to explore the solution as opposed to the analytical framework of *Wenegrat and McPhaden* [2016b]. These 1-D Ekman layer dynamics are shown to behave by dual inertial and diffusive processes. Ultimately, we relate the 1-D dynamics back to 2-D secondary circulations (Section 3.4.4, 3.5).

We assume that κ_v varies periodically with a bulk change $\Delta K = K_{\text{max}} - K_{\text{min}} > 0$ and define a mean vertical mixing $K_0 = \Delta K/2 + K_{\text{min}}$. We also assume that the barotropic component of (3.11) is unforced and choose solutions with $\int_{-H}^{0} \boldsymbol{u} dz = 0$.

The full solution is decomposed into steady and periodic components

$$\boldsymbol{u} = \overline{\boldsymbol{u}} + \boldsymbol{u}'\,, \tag{3.13}$$

where $\overline{\boldsymbol{u}}$ represents the steady solution and $\boldsymbol{u}'$ represents the periodic fluctuation about the steady-state. $\boldsymbol{u}'$ is assumed to have a time- and vertical-average of zero. The steady solution is given by

$$f\begin{pmatrix} -\overline{v} \\ \overline{u} \end{pmatrix} = K_0 \begin{pmatrix} \overline{u} \\ \overline{v} \end{pmatrix}_{zz}\,. \tag{3.14}$$

With boundary conditions

$$K_0\overline{u}_z = -\kappa_{v_0}\frac{\partial u_g}{\partial z} \quad \text{at} \quad z = 0\,, -H\,, \tag{3.15a}$$

$$K_0\overline{v}_z = 0 \quad \text{at} \quad z = 0\,, -H\,. \tag{3.15b}$$

Using (3.11), (3.13), and (3.14), the periodic solution is given by

$$\begin{pmatrix} u' \\ v' \end{pmatrix}_t + f\begin{pmatrix} -v' \\ u' \end{pmatrix} - \kappa_v(t)\begin{pmatrix} u' \\ v' \end{pmatrix}_{zz} = (\kappa_v(t) - K_0)\begin{pmatrix} \overline{u} \\ \overline{v} \end{pmatrix}_{zz}\,, \tag{3.16}$$

with $u'_z = v'_z = 0$ as free-slip boundary conditions at the surface and bottom.

3.4.1.1 Non-Dimensionalization

We non-dimensionalize (3.14) and (3.16) to understand the parameter regimes controlling the evolution of the circulation. We choose scalings $z \sim H$, $f \sim f_0$, $t, \Delta t \sim T$, $b_y/f \sim \Lambda$, $\overline{\boldsymbol{u}} \sim \Lambda H$, $\kappa_v \sim \Delta K/2$, and $\boldsymbol{u}' \sim \Delta K \Lambda T/2H$. Here, T represents a diurnal period (1 day) and Λ a geostrophic shear. We introduce a non-dimensional vertical diffusivity, $K(t) = \mathcal{K}(t) + k$, where $\mathcal{K}(t) = \cos(2\pi t/T)$ and $k = 2K_0/\Delta K$ is a non-dimensional parameter that expresses the bulk change in vertical diffusivity relative to the time-mean.

Defining $\mathrm{Ek}_0 = K_0/f_0H^2$ and choosing $\Lambda = 1$, (3.14) can be non-dimensionalized, [5]

$$\begin{pmatrix} -\overline{v} \\ \overline{u} \end{pmatrix} = \mathrm{Ek}_0\begin{pmatrix} \overline{u} \\ \overline{v} \end{pmatrix}_{zz}\,, \tag{3.17}$$

with boundary conditions $\overline{u}_z = -1$ and $\overline{v}_z = 0$ at $z = 0\,, -1$. (3.17) represents a background Ekman layer system that sets and passes on vertical structure to $\boldsymbol{u}'$.

[5] The choice of $\Lambda = 1$ is arbitrary as it divides out in the non-dimensionalization and only appears in the boundary condition for $\overline{u}_z$. Variation in Λ does not change general solution behavior.

The periodic problem (3.16) becomes

$$\begin{pmatrix} u' \\ v' \end{pmatrix}_t + \Omega \begin{pmatrix} -v' \\ u' \end{pmatrix} - \Gamma \left(\mathcal{K}(t) + k\right) \begin{pmatrix} u' \\ v' \end{pmatrix}_{zz} = \mathcal{K}(t) \begin{pmatrix} \overline{u} \\ \overline{v} \end{pmatrix}_{zz} , \tag{3.18}$$

with analogous boundary conditions to (3.16). Here, $\Omega = T f_0$ is a ratio of the inertial frequency (f_0) to the diurnal period (T) and $\Gamma = T\Delta K / 2H^2$ represents a ratio of the range of mixing time-scales $\left(\Delta K / H^2\right)$ relative to the diurnal period. Γ and Ω express the control by inertial or diffusive dynamics on accelerations.

The periodic solution is further decomposed

$$\boldsymbol{u}' = \boldsymbol{u}'' + \boldsymbol{u}_* , \tag{3.19}$$

where $\boldsymbol{u}_*$ represents the periodic T^2W component and $\boldsymbol{u}''$ represents the difference between the periodic T^3W and T^2W solutions. $\boldsymbol{u}''$ evolves as

$$\begin{pmatrix} u'' \\ v'' \end{pmatrix}_t + \Omega \begin{pmatrix} -v'' \\ u'' \end{pmatrix} - \Gamma \left(\mathcal{K}(t) + k\right) \begin{pmatrix} u'' \\ v'' \end{pmatrix}_{zz} = - \begin{pmatrix} u_* \\ v_* \end{pmatrix}_t . \tag{3.20}$$

With the same boundary conditions imposed on $\boldsymbol{u}'$.

The evolution of $\boldsymbol{u}_*$ is given by

$$\Omega \begin{pmatrix} -v_* \\ u_* \end{pmatrix} - \Gamma \left(\mathcal{K}(t) + k\right) \begin{pmatrix} u_* \\ v_* \end{pmatrix}_{zz} = \mathcal{K}(t) \begin{pmatrix} \overline{u} \\ \overline{v} \end{pmatrix}_{zz} . \tag{3.21}$$

From this decomposition, we see the same inertial and diffusive parameters on the L.H.S. of (3.20) (analogous to (3.18)). $\boldsymbol{u}_*$ changes due to the time-tendency of the mixing (the 2nd L.H.S term in (3.21)) with a baseline vertical structure imposed by the steady-solution $\overline{\boldsymbol{u}}$ (R.H.S term in (3.21)).

For completeness, and for reference to metrics used in Section 3.4.2, evolution of the full-flow ($\boldsymbol{u}$) is given by:

$$\begin{pmatrix} u \\ v \end{pmatrix}_t + \Omega \begin{pmatrix} -v \\ u \end{pmatrix} - \Gamma \left(\mathcal{K}(t) + k\right) \begin{pmatrix} u \\ v \end{pmatrix}_{zz} = \mathcal{K}(t) \left(1 - \Gamma\right) \begin{pmatrix} \overline{u} \\ \overline{v} \end{pmatrix}_{zz} . \tag{3.22}$$

The non-dimensional parameters Ek_0, Ω, Γ, and k will control the solution behavior, with Γ and Ω exerting the most control on the solution behavior in physically relevant parameter spaces (defined below). (3.17), (3.18), (3.21), and (3.20) are solved numerically (detailed in the supplemental information of *Dauhajre and McWilliams* [2018] and model code can be found at `https://github.com/ddauhajre/T3W_ND_MODEL`). We solve for the steady-flow ($\overline{\boldsymbol{u}}$) first, then time-step for the periodic transient component ($\boldsymbol{u}'$). At each time-step, the periodic $\mathrm{T}^2\mathrm{W}$ component ($\boldsymbol{u}_*$) and periodic difference component ($\boldsymbol{u}''$) are computed from the periodic transient component ($\boldsymbol{u}'$). We initialize $\boldsymbol{u}'(t = 0) = 0$. All of the 1-D solutions shown in the following subsections (Table 3.1) are run for 10 diurnal periods and exhibit periodicity.

Table 3.1: Parameters for the 1-D $\mathrm{T}^3\mathrm{W}$ non-dimensional cases. Cases P1 and P2 increase Γ and Ω, respectively, relative to the base case. All cases are run for 10 diurnal periods and exhibit periodicity.

Case	Base	P1	P2
k	1.007	1.007	1.007
Γ	0.26	1.5	0.26
Ω	4.92	4.92	9.84
Ek_0	0.05	0.05	0.05

3.4.2 Base Case

The non-dimensional system (3.17) - (3.21) takes 4 realistic parameters as inputs: $K_{\mathrm{max}}, K_{\mathrm{min}}, h_{\mathrm{sbl}}$, and f_0. We present a base case within a physically relevant parameter space for a submesoscale front or filament undergoing diurnal forcing ($K_{\mathrm{max}} = 3 \times 10^{-2}$ $\mathrm{m^2 s^{-1}}$, $K_{\mathrm{min}} = 10^{-4}$ $\mathrm{m^2 s^{-1}}$, $h_{\mathrm{sbl}} = 70$ m, $f_0 = 5.7 \times 10^{-5}$ $\mathrm{s^{-1}}$), which gives the non-dimensional parameters: $k = 1.007$, $\Omega = 4.92$, $\Gamma = 0.26$, $\mathrm{Ek}_0 = 0.05$ (Table 3.1). This solution illustrates relevant 1-D solution behavior and highlights the dual inertial and diffusive mechanisms driving temporal variability.

Figure 3.5 shows the (z, t) evolution for the base case solution. The full flow shows oscillations in

u and v characterized by a deepening and strengthening of the near-surface and bottom flows. The vertical structure of these flows is controlled by $\overline{\boldsymbol{u}}$ through the R.H.S term in (3.19). In the base case, the primary oscillation in v leads u, with the strongest v occurring near the minima in the non-dimensional mixing $\mathcal{K}(t)$ at $t/T = 0.5$ and the strongest u occurring at $t/T = 0.7$. The periodic transient components u', v' differs greatly from the periodic TTW component u_*, v_*; an indication of the failure of the TTW system to capture the diurnal motion, especially at mid-day ($t/T = 0.5$), when mixing is weakest. This difference is demonstrated by the large magnitude of u'', v''. The (z, t) structure of u and v is in general agreement with the solution of [*Wenegrat and McPhaden*, 2016b]. In Section 3.4.4, the phasing of u and v in this solution will be translated back to ζ and δ (in a front or filament) to illustrate the predictive capability of the 1-D model.

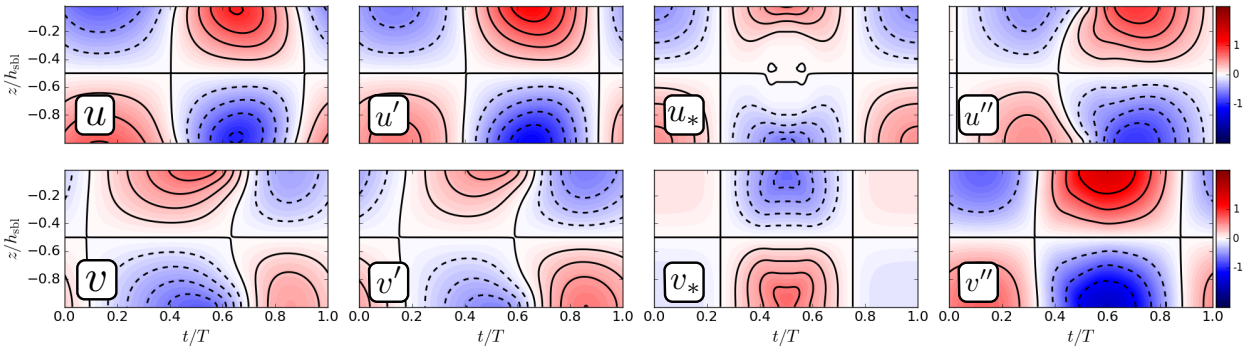

Figure 3.5: Solution for the non-dimensional base case over the tenth diurnal period. Shown is the full component of the flow (first column), the periodic transient component (second column), the periodic T^{2}W component (third column), and the periodic difference between the transient and T^{2}W components (fourth column).

Inertial or diffusive terms can be responsible for $\boldsymbol{u}_t$. One way to quantify the relative importance of these terms is to look at their relative magnitudes in the momentum balance (as in *Wenegrat and McPhaden* [2016b]). Here, we take a different approach and diagnose the dominance of either with a difference of normalized covariances, based on terms in (3.22), and defined for x and y

components as follows:

$$C_x(t) = \frac{\langle u_t - \mathrm{rhs_u}\rangle\langle \Omega v\rangle}{\left(\overline{\langle u_t - \mathrm{rhs_u}\rangle^2}^t\,\overline{\langle \Omega v\rangle^2}^t\right)^{1/2}} - \frac{\langle u_t - \mathrm{rhs_u}\rangle\langle \Gamma\left(\mathcal{K}(t)+k\right)u_{zz}\rangle}{\left(\overline{\langle u_t - \mathrm{rhs_u}\rangle^2}^t\,\overline{\langle \Gamma\left(\mathcal{K}(t)+k\right)u_{zz}\rangle^2}^t\right)^{1/2}}, \tag{3.23a}$$

$$C_y(t) = \frac{\langle v_t - \mathrm{rhs_v}\rangle\langle \Omega u\rangle}{\left(\overline{\langle v_t - \mathrm{rhs_v}\rangle^2}^t\,\overline{\langle \Omega u\rangle^2}^t\right)^{1/2}} - \frac{\langle v_t - \mathrm{rhs_v}\rangle\langle \Gamma\left(\mathcal{K}(t)+k\right)v_{zz}\rangle}{\left(\overline{\langle v_t - \mathrm{rhs_v}\rangle^2}^t\,\overline{\langle \Gamma\left(\mathcal{K}(t)+k\right)v_{zz}\rangle^2}^t\right)^{1/2}}. \tag{3.23b}$$

Where $\mathrm{rhs_u} = \mathcal{K}(t)(1-\Gamma)\,\overline{u}_{zz}$, $\mathrm{rhs_v} = \mathcal{K}(t)(1-\Gamma)\,\overline{v}_{zz}$, the overline in the denominators denotes a time-mean, and $\langle . \rangle$ denotes a RMS in z. C_x and $C_y > 0$ imply that inertial motions cause the acceleration terms ($\boldsymbol{u}_t$) and C_x and $C_y < 0$ imply that the vertically diffusive terms cause $\boldsymbol{u}_t$. [6] In the analysis that follows, we show the sum of these terms $\left(C_x + C_y\right)$, which leads to the same interpretations as analysis of the individual time-series.

We also quantify a normalized magnitude of the difference of $\boldsymbol{u}'$ from $\boldsymbol{u}_*$ as

$$D(t) = \left(\frac{\overline{u''^2 + v''^2}^z}{\overline{u_*^2 + v_*^2}^{z,t}}\right)^{1/2}. \tag{3.24}$$

Both instantaneously large $D(t)$ and a time-mean over a diurnal period T $\left(\overline{D(t)}^t\right)$ indicate disagreement between $\boldsymbol{u}'$ and $\boldsymbol{u}_*$.

Figure 3.6 shows $C_x + C_y$ (a) and D (b) for the base case. As $\mathcal{K}(t)$ decreases to its minima at $t/T = 0.5, C_x + C_y > 0$, which implies that inertial terms cause the acceleration during the night-to-day decrease in mixing. Conversely, as $\mathcal{K}(t)$ increases back to its maxima ($t/T > 0.5$), $C_x + C_y < 0$, indicating that diffusive terms cause the acceleration during the day-to-night increase in mixing. The $D(t)$ curve (Figure 3.6b) shows that there is a persistent non-zero deviation of the

[6] C_x and C_y are a form of normalized covariance, but the individual terms in (3.23) subtracted from each other are not "standard" correlation coefficients (i.e., bounded by $[-1, 1]$). C_x, C_y are bounded, but their bounds are dictated by the RMS. The numerator's use of the product of separate vertical RMS terms ($\langle a\rangle\langle b\rangle$) produces similar results and interpretations to a RMS of the product of two terms ($\langle ab\rangle$), with only the magnitude varying between the two forms of the metric (not the temporal structure).

T^2W and T^3W solutions, with the largest difference occurring after the minima in mixing after the inertially-caused acceleration of the flows.

The analysis of the base case shows that inertial- and diffusive-driven accelerations control the phasing of u and v on either side of the diurnal cycle. The T^2W solution (u_*, v_*) is unable to capture these accelerations and incorrectly predicts the diurnal evolution for this parameter regime.

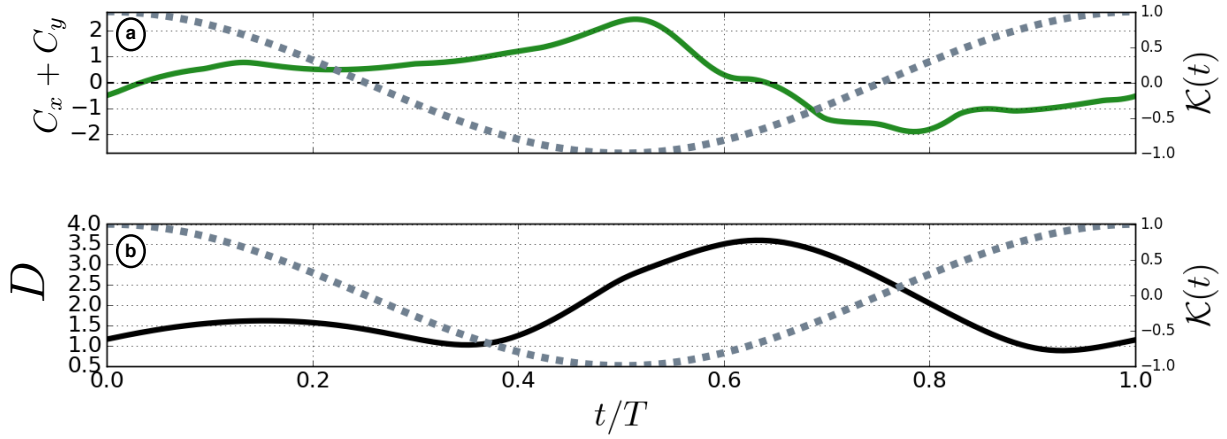

Figure 3.6: Temporal evolution metrics (a) $C_x + C_y$ (Eq. (3.23)) and (b) D (Eq. (3.24)) for the base case. In (a), $C_x + C_y > 0$ implies an inertial-caused acceleration and $C_x + C_y < 0$ implies a diffusive-caused acceleration. D indicates the magnitude of $\boldsymbol{u}''$ normalized by $\boldsymbol{u}_*$. The non-dimensional diffusivity $\mathcal{K}(t)$ is shown in the dashed gray line corresponding to the right-hand vertical axis.

3.4.3 Parameter varations

The main controls on the non-dimensional system are expressed in the parameters Γ and Ω, which set the diffusive and inertial time-scales, respectively. k will primarily control the amplitude of the response and Ek_0 sets vertical structure of the solution. We present two more solutions, P1 and P2, which increase Γ and Ω, respectively, relative to the base case (Table 3.1). P1 increases the range of diffusive time-scales with $\Gamma = 1.5$ and P2 increases the inertial time-scale with $\Omega = 9.84$. These increases in Γ and Ω are relatively large and are used to clearly illustrate the isolated effect of each parameter.

In P1, the increase in Γ results in a sharper oscillation in v' that is more confined to the surface and bottom layers, respectively (Fig. 3.7a). Here, there is still substantial disagreement between the periodic transient (v') and periodic steady (v_*) components, indicated by relatively large v'' at mid-day (Fig. 3.7b,c). In P2, the increase in Ω results in an oscillation that is phase-shifted relative to the base-case (positive v' peaks earlier, Fig. 3.7d). The periodic steady and periodic transient components agree more in their phasing, but the difference between the two still exhibits large magnitude (Fig. 3.7e,f).

The increase in Γ in P1 causes the diffusive-driven acceleration ($C_x + C_y < 0$) to appear at the start of the diurnal period (Fig. 3.8a, green curve). There is also a more exaggerated inertial acceleration mid-day at $t/T = 0.5$ (Fig. 3.8a, green curve). P2 exhibits predominantly inertial dynamics ($C_x + C_y > 0$) with a peak mid-day, followed by a short diffusive-driven acceleration at $t/T = 0.65$ (Fig. 3.8a, orange curve). However, the large Ω in P2 dictates mostly inertial dynamics. Both cases show large mid-day deviations between the transient and steady periodic components (Fig. 3.8b). In P1, the largest deviation occurs earlier relative to the base case (Fig. 3.8b, green curve) and in P2 the persistent inertial dynamics cause a larger and more sustained deviation throughout the diurnal period (Fig. 3.8b, orange curve).

3.4.4 1-D translation to δ and ζ

The 1-D non-dimensional solutions explored above can ultimately be translated back to a prediction of surface divergence and vorticity phasing in a front or filament circulation with the underlying assumption of slowly changing geostrophic shear b_y/f. Eq. (3.22) gives the evolution of the ageostrophic flow in such a circulation, and a translation to a non-dimensional divergence and vorticity can be made as follows: $\delta_{ND} \propto 2v$ and $\zeta_{ND} \propto \zeta_g + u$. Here, the divergence is completely ageostrophic, and the factor of 2 is to emphasize that the divergence is simply the difference between two oppositely signed vertical columns on separate sides of a dense filament. The cyclonic vorticity of a filament is modified by the ageostrophic vorticity that modulates the

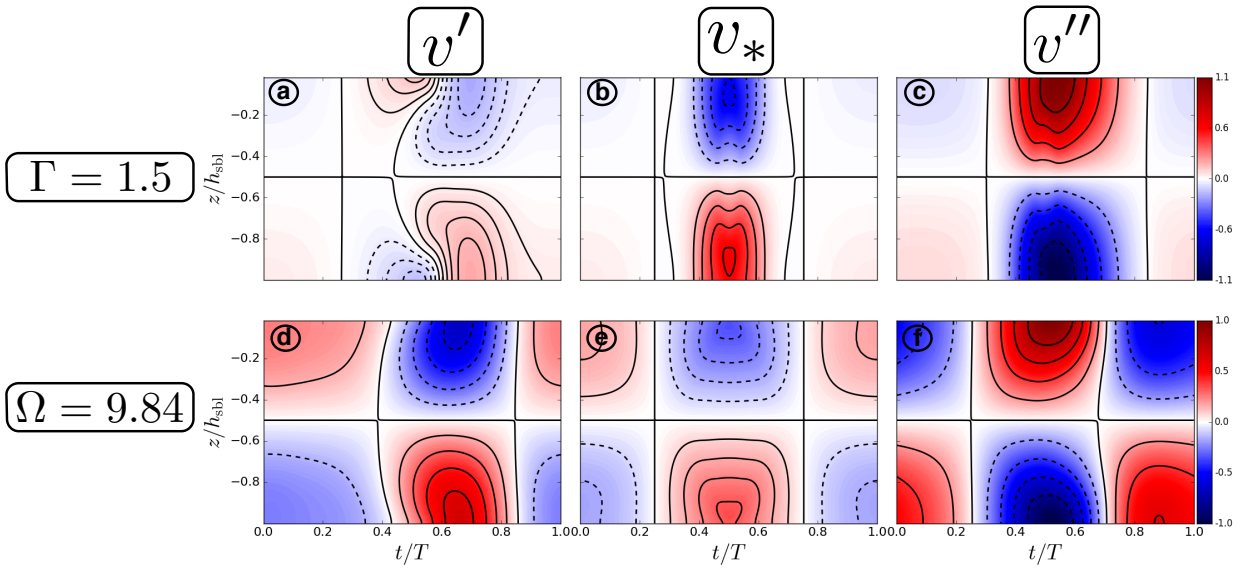

Figure 3.7: Transverse flow components v' (first column), v_* (second column) and v'' (third column) for the two parameter variation solutions P1(first row) and P2 (second row), that vary a single non-dimensional parameter relative to the base case (Fig. 3.5). P1 increases Γ and P2 increases Ω relative to the base case with the values indicated in each row. (z, t) evolution is shown for the tenth diurnal period. v', v_*, and v'' are defined in (3.19), (3.21), and (3.20), respectively.

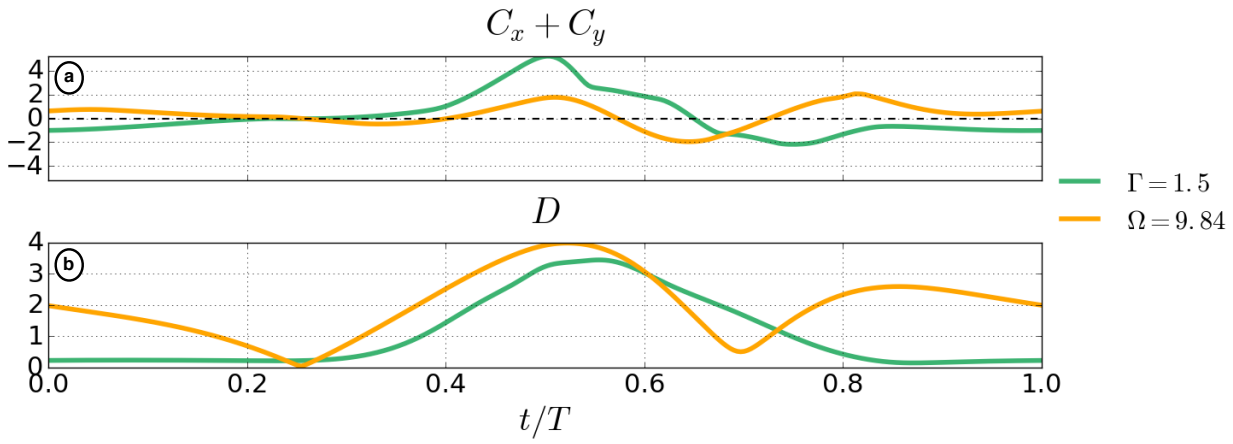

Figure 3.8: Temporal evolution metrics (a) $C_x + C_y$ (Eq. (3.23)) and (b) D (Eq. (3.24)) for cases P1 (green) and P2 (orange) solutions. The non-dimensional parameter varied, relative to the base case is indicated in the legend for each solution.

geostrophic component of the vorticity (ζ_g), which we set to 1 for simplicity (*i*.e., the cyclonic vorticity is mostly geostrophic and modulated by the anticyclonic, ageostrophic vorticity evolution).

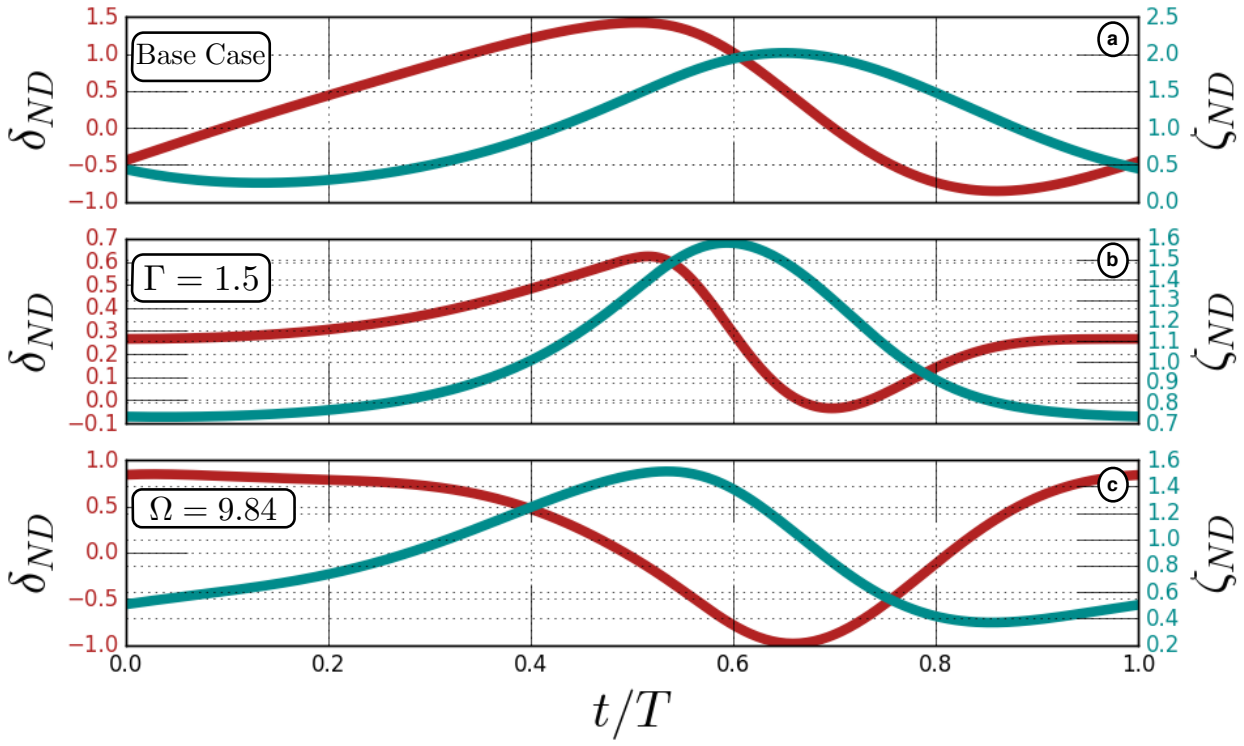

Figure 3.9: Surface divergence (dark red) and vorticity (dark cyan) phasing predictions by the non-dimensional solutions (base case (a) and two parameter variations (b-c), Table 3.1) over a diurnal period. Here, $\delta_{ND} = 2v$, and $\zeta_{ND} = 1 + u$, where u, v are the (ageostrophic) surface velocities (Eq. (3.22)). The magnitudes of δ_{ND} and ζ_{ND} are non-dimensional and not meant to predict the exact magnitude of δ and ζ in a realistic front or filament, but rather the general phasing of δ and ζ for different parameter regimes. $\Omega = Tf_0$ and $\Gamma = T\Delta K/2H^2$ are non-dimensional parameters that represent the control by inertial or diffusive time-scales, respectively, relative to a diurnal time-scale ($T = 1$ day; discussed in Section 3.4)

Figure 3.9 shows these translations for the base case, P1, and P2 solutions (based on the surface velocity $\boldsymbol{u}(z = 0)$) which can be qualitatively compared to the metric from a ROMS simulation in Fig. 3.1. The base case displays peak δ at mid-day, with ζ lagging δ. In P2, δ peaks at mid-day, though less strongly than in the base case (note the different y-axis scalings), and ζ and δ are less phase-lagged. In P3, δ is strongest earliest in the day, and ζ peaks mid-day. These results

suggest a nuanced view of the diurnal evolution of δ and ζ in fronts and filaments, with phasing controlled by inertial- and diffusive-time scales set by latitude, boundary layer depth, and the strength of the diurnal forcing.

3.5 Validation of the 1-D model with ROMS data

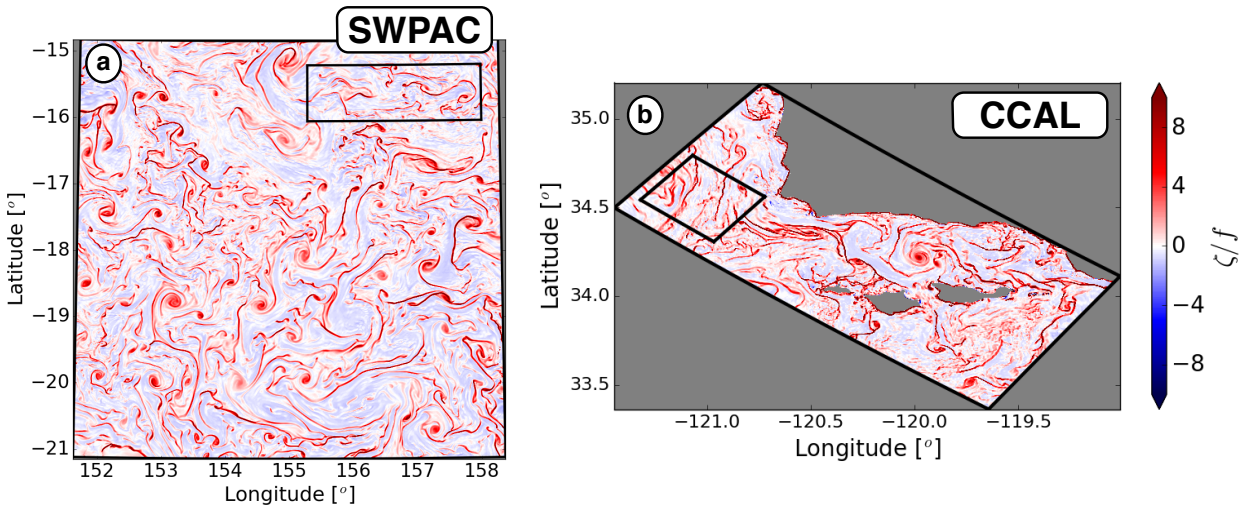

Figure 3.10: Snapshot of surface relative vorticity (normalized by f) in (a) the southwestern Pacific (SPWAC) and (b) coastal California (CCAL) ROMS simulations. The sub-domains used to generate the root-mean square fields in Fig. 3.11 are indicated for each region (small black boxes). The snapshots correspond to hours 15 (SWPAC) and 14 (CCAL) in the time-series in Fig. 3.11.

Here, we show the predictive capability of the 1-D non-dimensional system by using it to reproduce the phasing of δ and ζ observed in ROMS simulations of two different regions: southwestern Pacific (SWPAC, $\Delta x \approx 700$ m) and coastal California near Pt. Conception (CCAL, $\Delta x \approx 100$ m). Details of solution setups are in chapter supplement (Section 3.7.2). A snapshot of surface relative vorticity for each solution (Fig. 3.10) shows the ubiquity of high Ro submesoscale structures in each solution. A diurnal cycle in κ_v, δ and ζ for each solution is shown in Fig. 3.11 as a spatial RMS of surface δ, ζ and boundary layer κ_v for two diurnal periods. The RMS curves are generated from sub-regions in each of the simulations (Fig. 3.10, small black boxes) during times where multi-

ple submesoscale fronts and filaments exist forced by primarily solar heating (with weak winds). There is a notable regional sensitivity in the diurnal phasing of δ and ζ. At lower-latitudes (SWPAC, latitude $\approx -15°$), δ peaks later in the day and ζ and δ are less phase-lagged ($\approx$ 1 hour lag). At mid-latitudes (CCAL, latitude $\approx 34°$), δ peaks mid-morning and there is a $\approx 2-4$ hour phase lag between δ and ζ.

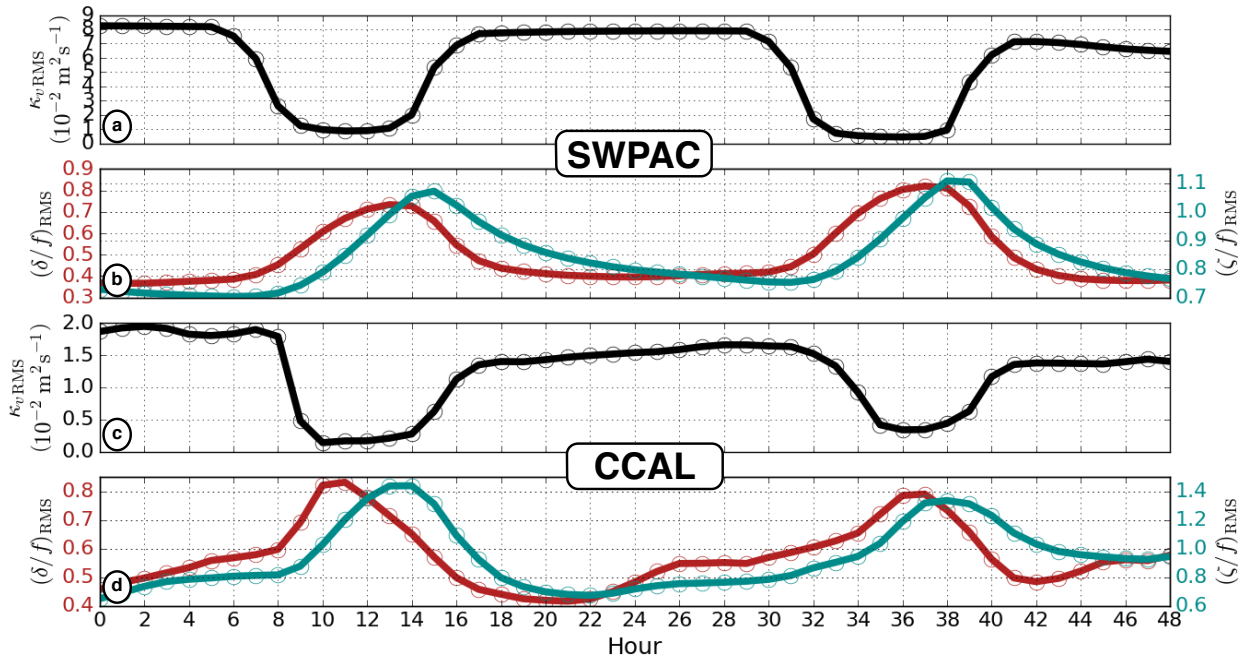

Figure 3.11: Time-series of spatial RMS of κ_v in the upper 40 m (black curve) and δ/f (dark red) and ζ/f (dark cyan) at the surface in ROMS simulations of (a-b) the Southwestern Pacific (SWPAC) and (c-d) coastal California (CCAL). The spatial RMS is computed over a sub-domain in each simulation in an open-ocean region, away from the coastline at times when submesoscale currents are well-defined (Fig. 3.10) and subject to a relatively clean diurnal forcing (*i.e.*, strong heating/cooling and weak winds). The plots show two diurnal periods for each simulation, with the RMS values calculated from 1-hour instantaneous averages (dots); the x-axis time-scale is arbitrary and defined by the initial data point, not the local time. Note the difference in the phasing of the δ and ζ in response to changes in κ_v in the two simulations. δ and ζ show little phase separation and peak later (relative to the drop in κ_v) in the SWPAC (latitude $\approx -15°$). In CCAL (latitude $\approx 34°$), δ is strongest near the initial minimum in κ_v with a larger phase separation between δ and ζ compared to SWPAC. The local time of the initial data point in SWPAC (a-b) is 7/21/2007 00:30 and in CCAL (c-d) 12/4/2006 01:35.

As noted in the previous section, the only inputs needed for the non-dimensional 1-D system are $K_{\max}, K_{\min}$, h_{sbl}, and f_0. We take an average of f_0 and h_{sbl} (for the times plotted) from the sub-domains used to generate the curves in Fig. 3.11, and set a $K_{\max}, K_{\min}$ based on the first diurnal period in the RMS time-series in Fig. 3.11a,c. These physical inputs and resulting non-dimensional parameters are given in Table 3.2 for the two regions. We run the 1-D non-dimensional model (with a sinusoidal forcing, $\mathcal{K}(t)$ as in Section 3.4) [7] for the two regions and plot the translated δ_{ND}, ζ_{ND} (defined in Section 3.4.4) in Fig. 3.12 for two diurnal periods.

Table 3.2: Parameters for the application of the 1-D model to ROMS data for the southwestern Pacific (SWPAC) and coastal California (CCAL). Physical inputs to the system ($K_{\max}, K_{\min}, f_0, h_{\text{sbl}}$) are taken from the ROMS simulations (Fig. 3.11) and converted into the non-dimensional parameters ($k, \Gamma, \Omega, \text{Ek}_0$) as inputs for 1-D model (Eqs. (3.17) - (3.21)) . $K_{\max}, K_{\min}$ are taken as the maximum and minimum $\kappa_{v_{\text{RMS}}}$ for the first diurnal period in Fig. 3.11, and f_0 and h_{sbl} are taken as spatial averages in the regions where the RMS curves in Fig. 3.11 are obtained. $k, \Gamma, \Omega, \text{Ek}_0$ are defined in Section 3.4.1. All cases are run for 10 diurnal periods and exhibit periodicity.

Region	SWPAC	CCAL
$K_{\max}$ $\left(\text{m}^2\text{s}^{-1}\right)$	0.082	0.019
$K_{\min}$ $\left(\text{m}^2\text{s}^{-1}\right)$	0.0045	0.0014
$\lvert f_0 \rvert$ $\left(\text{s}^{-1}\right)$	3.93×10^{-5}	8.27×10^{-5}
h_{sbl} (m)	76	37
k	1.12	1.16
Γ	0.58	0.56
Ω	3.4	7.15
Ek_0	0.2	0.09

The 1-D model is able to reproduce the general behavior for each region. At lower latitude (SWPAC, Fig. 3.12b), δ and ζ have a very small phase separation and and peak later in the diurnal period (coincident with weaker mixing, as in the ROMS data). In this case, diffusive dynamics are

[7] The κ_v curves in Fig. 3.11 exhibit a step-like temporal shape. We use a sinusoidal forcing for the 1-D model because $\mathcal{K}(t)$ is defined with a time-average of zero. We note that while the temporal shape of $\mathcal{K}(t)$ can control some of the solution behavior, it does not greatly affect the general predictive capability of the 1-D solutions.

more dominant (*i*.e., control by Γ) and $u(\propto \zeta)$ and $v(\propto \delta)$ in the 1-D system evolve more in phase with each other. The CCAL solution (Fig. 3.12c) exhibits a larger phase separation between δ_{ND} and ζ_{ND}, with δ_{ND} peaking earlier, when the mixing has just reached its minimum. Relative to SWPAC, this regime has a stronger expression of inertial dynamics that drive a larger phase separation between δ_{ND} and ζ_{ND}. These results indicate that the simple 1-D model is able to capture the primary processes controlling the diurnal phasing of submesoscale currents in a fully 3-D, PE solution and highlights a latitudinal sensitivity to the diurnal phasing of δ and ζ in submesoscale circulations.

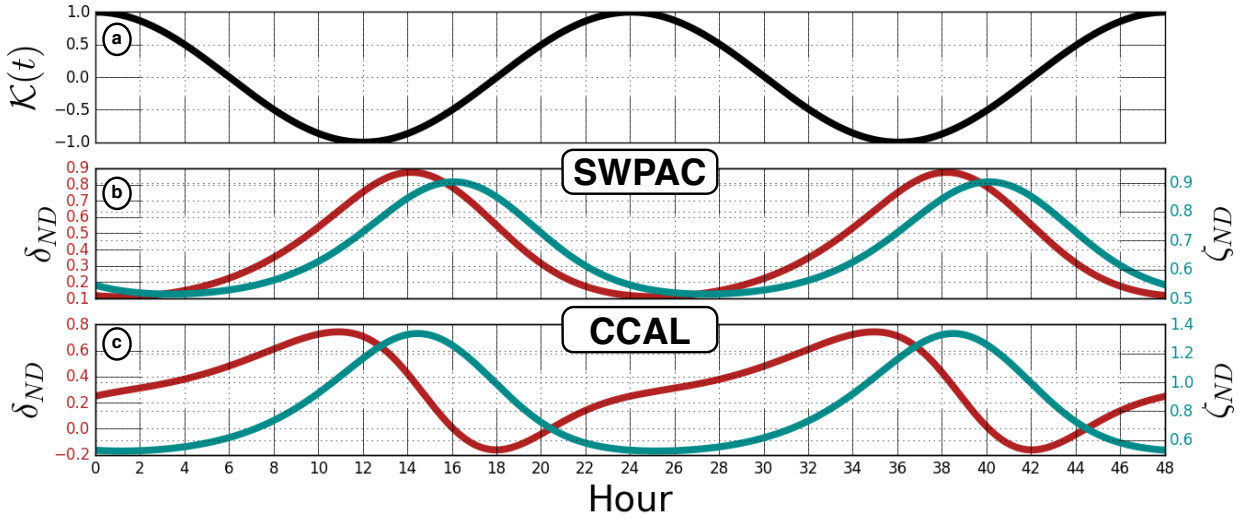

Figure 3.12: 1-D non-dimensional model predicted δ_{ND} (dark red) and ζ_{ND} (dark cyan) for (b) the south-western Pacific (SWPAC) and (c) coastal California (CCAL) parameter regimes (Table 3.2) defined by the ROMS simulations (Fig. 3.11). (a): the non-dimensional vertical mixing $\mathcal{K}(t)$ (defined in Section 3.4.1) is shown for phasing reference. The curves show two diurnal periods. δ_{ND} and ζ_{ND} are defined as in Fig. 3.9. Note the general agreement with the curves in Fig. 3.11 for each region. In SWPAC, the peak in δ_{ND} and ζ_{ND} are closer together and occur later. In CCAL, there is a larger phase separation between δ_{ND} and ζ_{ND}, with the strongest δ_{ND} occurring earlier in the diurnal period.

The simple 1-D model can guide observational campaigns aimed at sampling fronts and filaments at times of maximal convergence and vorticity. Fig. 3.13 provides an approximate roadmap (and summary of general phasing trends) for δ, ζ phasing, based on the CCAL 1-D solution for a range of latitudes (Fig. 3.13a) and h_{sbl} (Fig. 3.13b) to show the effect on the phasing of δ, ζ for these

important parameters. At lower latitudes or shallower boundary layers, the phase lag between δ and ζ will be small, and they will peak after or close to the minimum in vertical mixing. At higher latitudes or deeper mixed layers, the phase lag between δ and ζ increases and δ peaks earlier than the minimum in mixing.

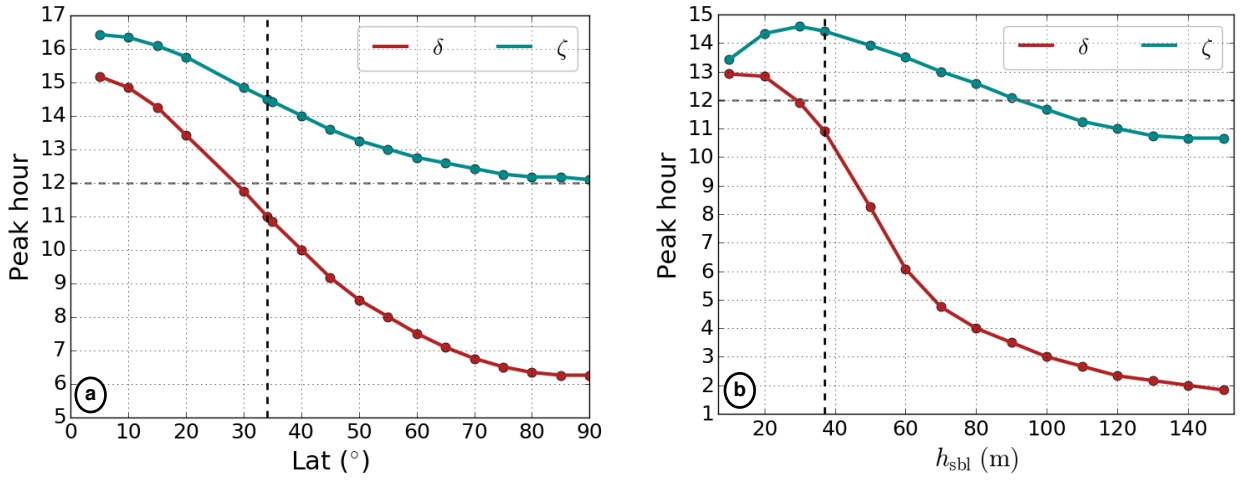

Figure 3.13: 1-D non-dimensional predicted times of maximal δ (dark red) and ζ (dark cyan) based on the CCAL parameter regime (Table 3.2). The 1-D model is run at different (a) latitude and (b) h_{sbl} (latitude changes Ω, Ek_0 and h_{sbl} changes Γ, Ek_0 in Eqs. (3.17) - (3.21)). The peak hour can be interpreted relative to the minimum in vertical mixing (hour 12, dashed grey line). At lower latitude or shallower mixed layer depth, there is a later peak in both δ and ζ with little phase lag. Conversely, at higher latitude or deeper mixed layer depth, δ and ζ peak earlier, with a larger phase lag. For reference, the CCAL solution (Section 3.5) is indicated by the vertical black dashed line.

3.6 Summary and Discussion

The T^2W diagnostic is capable of predicting the low-frequency spatial structure of 2-D front or filament circulations given a strong, non-changing, boundary layer vertical diffusivity and lateral density gradient. However, large diurnal changes in vertical diffusivity cause fluctuations in the strength of front or filament circulations that are not captured by the instantaneous T^2W relation. In this paper, the T^2W relation is expanded to include time-memory to give the T^3W system, posed

here for a 2-D transverse-depth plane. This simple 2-D system is able to reproduce the observed diurnal phasing in a realistic, PE simulation (Figures 3.1, 3.11). Inherent in the 2-D T^3W system are 1-D Ekman layer dynamics that control the phasing of the flow over a diurnal period by dual inertial- and diffusive-driven accelerations in response to changes in κ_v (independent of surface forcing). The oscillations in the local 3-D circulations can be attributed to these 1-D mechanisms imprinting onto the front or filament circulation that is quasi-stationary in its spatial structure as shown with an application of the 1-D model to 3-D ROMS solutions (Section 3.5).

The transient T^3W solutions disagree with a T^2W diagnostic and the extent of the discrepancies is controlled primarily by the magnitude of the change in κ_v over a diurnal period. The T^3W secondary circulation can be instantaneously stronger than its steady analog; however, transients driven by time-variability in κ_v can weaken the diurnally averaged secondary circulation. These results hold for a density front (as well as the filament analyzed in Section 3.3). A 1-D non-dimensional framework, posed with an assumption of stationarity in front or filament secondary circulation structure, exposes the primary mechanisms at play over a diurnal period. In mid-latitudes, an inertially-caused acceleration drives an increase in secondary circulation strength that leads to a large difference between T^2W and T^3W solutions as mixing decreases. Diffusive dynamics will primarily control the non-T^2W accelerations when mixing increases. The bulk change in vertical diffusivity, relative to its diurnal mean, (k) controls the amplitude of the transient oscillation. The relative phasing of δ and ζ is primarily controlled by the inertial and range of diffusive time-scales relative to the diurnal period (Ω and Γ, respectively). At larger (smaller) Γ (Ω), diffusive dynamics dominate and δ and ζ are less-phase lagged. The importance of these diffusive dynamics in 1-D Ekman layer systems has not been discussed in previous studies [*Wenegrat and McPhaden*, 2016b; *Zhang and Tan*, 2002; *Wiel et al.*, 2010].

The T^3W equations lack momentum advection. In real fronts and filaments, the effects of momentum advection is not small, especially during frontogenesis [*McWilliams*, 2017]. Here we have removed this source of non-linearity for simplicity in interpretation of the behavior in question. Momentum advection evaluated with the 2-D model solution (FIL1) (where this term is

neglected) show that it is smaller than the dominant retained terms in the linear balance (not shown), but not so small that it is an entirely accurate approximation. *McWilliams* [2017] shows that main effect of nonlinear (ageostrophic) advection on a front or filament is a strengthening of the secondary circulation when the wind is oriented favorably (NW or SE for a filament and SE for a front, for the transverse y-axis defined here). It is possible that in the real ocean the strengthening of the secondary circulation by momentum advection due to a favorable wind-stress simultaneously occurs with T^3W oscillations due to changes in $\kappa_v(t)$, though this remains an open question. However, the success of the 1-D non-dimensional system in predicting the diurnal phasing of submesoscale circulations in realistic, full PE simulations shows that linear 1-D Ekman layer dynamics capture the fundamental processes relevant to diurnal variability when there is a well-defined diurnal signal in κ_v.

With the 1-D model (Eqs. (3.17) - (3.21)), all that is needed to predict the phasing of δ and ζ in fronts or filaments (subject to clean diurnal forcing) is K_{max}, K_{min}, h_{sbl}, and f_0. *A priori* estimates of these four parameters inputted into the 1-D system can give an approximation of times of maximal δ and ζ. Such knowledge can guide both observational campaigns focused on high-frequency sampling of ephemeral submesoscale currents or pollution cleanup efforts on daily time-scales. Similarly, the 1-D model can provide an indirect measure of boundary layer turbulence (κ_v) with high-frequency measurements of $\boldsymbol{u}(z)$.

The diurnal fluctuations of secondary circulation are historically not considered in discussion of lateral or vertical fluxes induced by submesoscale coherent structures. Both the instantaneous and time-averaged modifications of the circulation have implications for fluxes (horizontal and vertical) associated with submesoscale structures. The role of submesoscale currents in regulating transport pathways of tracers is an open question and the results of this work imply a more nuanced view of material transport on daily time-scales by submesoscale circulations.

3.7 Supplement

3.7.1 2-D Dense Filament Idealization: Initial Condition and Spin-Up

We create $b(y,z)$ and $\kappa_v(y,z)$ and feed them into the T^{2}W balance to give an initial condition for u and v (and by continuity w). Following *McWilliams* [2017], a general 2-D surface boundary layer filament can be idealized as

$$b(y,z) = b_0 + N_b^2\,(z+H) + \frac{N_0^2}{2}\left[(1+B)\,z - (1-B)\left(h_{\text{sbl}}(y) + \lambda^{-1}\log\cosh\left[z + h_{\text{sbl}}(y)\right]\right)\right]\,. \tag{3.25}$$

With a boundary layer profile $h_{\text{sbl}}(y)$ designed to give a buoyancy extremum in the center:

$$h_{\text{sbl}}(y) = h_0 + \delta h\,\exp\left[-\left(\frac{y}{l}\right)^2\right]\,. \tag{3.26}$$

For case FIL1, we prescribe the following parameters:

$$l = 3000\text{ m}\,,\quad N_0^2 = 3.4\times10^{-5}\text{ s}^{-2}\,,\quad N_d^2 = 10^{-7}\text{ s}^{-2} \tag{3.27a}$$

$$b_0 = 6.4\times10^{-3}\text{ m s}^{-2}\,,\quad B = 0.025\,,\quad \lambda^{-1} = 3\text{ m}\,, \tag{3.27b}$$

and set a shallow-water domain with

$$H = 50\text{ m}\,,\quad h_0 = 35\text{ m}\,. \tag{3.28}$$

For such a filament, the boundary layer depth deepens by $\delta h = 15$m at the center of the filament with $L_y = 15$ km. We set $\Delta z = 0.5$ m. For all simulations, we use a time-step $\Delta t = 120$ s and horizontal spacing $\Delta y = 150$ m.

An initial guess of κ_v is fed into a T^{2}W iteration with the idealized $b(y,z)$. κ_v is idealized as in

McWilliams et al. [2015]:

$$\kappa_v(y,z) = \kappa_{v_0} G(\sigma) \frac{h_{\text{sbl}}(y)}{h_0} + \kappa_{v_b}\,, \quad \sigma = -\frac{z}{H}\,, \tag{3.29a}$$

$$G(\sigma) = C_G\,(\sigma_0 + \sigma)\,(1-\sigma)^2\,, \quad \sigma \le 1\,, \tag{3.29b}$$

$$G(\sigma) = 0\,, \quad \sigma \ge 1\,. \tag{3.29c}$$

Where κ_{v_0} is a baseline amplitude for the diffusivity; $0 < \kappa_{v_b} << \kappa_{v_0}$ is a background diffusivity in the interior; $C_G = 4\left(1+\sigma_0^2\right)/27$ limits the vertical column maximum of $G = 1$; and σ_0 is a velocity logarithmic singularity regularization constant as $\sigma \to 0$.

We choose the following parameters:

$$\kappa_{v_0} = 0.02 \text{ m}^2 \text{ s}^{-1}\,, \quad \kappa_{v_b} = 10^{-4} \text{ m}^2 \text{ s}^{-1}\,, \quad \sigma_0 = 5 \times 10^{-3}\,. \tag{3.30}$$

For case FIL1, $b(y,z)$ from (3.25) and $\kappa_v(y,z)$ from (3.29) are used in (3.1) to give initial guesses of u, v, w. These fields are then input into KPP to give a new $\kappa_v, \kappa_b, h_{\text{sbl}}, h_{\text{bbl}}$. This procedure is iterated until convergence whereby $\kappa_v, \kappa_b, h_{\text{sbl}}, h_{\text{bbl}}$ are calculated by KPP and then used to give a new u, v, w by (3.1).

We spin-up the solution to allow the KPP vertical diffusivities and boundary layers to adjust to a well-behaved state as well as allow any transient adjustments in other fields to take place. Diurnal cycling of the surface forcing (for case FIL1, Q_s) begins once the solution has reached an equilibrated state. The spin-up for case FIL1 is as follows:

1. Solve for initial u, v with (3.1) given $b(y,z)$ and $\kappa_v(y,z)$ with $Q_s = 0$ W m^{-2} and $\tau_y^s = 0.1$ N m^{-2}.
2. Prescribe constant $\tau_y^s = 0.1$ N m^{-2} for days 1-2.
3. On day 3, linearly decrease τ_y^s to 0.02 N m^{-2} and linearly decrease Q_s to -100 W m^{-2}.

4. Hold $Q_s = -100$ W m^{-2} and $\tau_y^s = 0.02$ N m^{-2} constant through day 4.

5. Diurnally vary Q_s beginning on day 5.

3.7.2 ROMS Setup: SWPAC and CCAL

The SWPAC and CCAL simulations are made with ROMS [*Shchepetkin and McWilliams*, 2005], a hydrostatic, primitive equation model that uses a K-profile parameterization (KPP; *Large et al.* [1994]; *McWilliams et al.* [2009c]) for vertical mixing. Submesoscale circulations are resolved in both SWPAC and CCAL with a nesting procedure. Both solutions contain 1-hour instantaneous averaged output and are hindcasts of winter months, with SWPAC beginning on 7/19/2007 and CCAL on 11/20/2006.

The SWPAC solution nesting procedure is analogous to the solution in *Srinivasan et al.* [2017]. An outer grid ($\Delta x = 12$ km) encompasses the entire Pacific Ocean with initial and boundary conditions given by SODA climatology. Three more nests are made at $\Delta x = 6$ km, $\Delta x = 1.5$ km, and $\Delta x = 0.7$ km. This inner-most nest (Fig. 3.10a) contains 50 vertical levels and is used in Section 3.5 to obtain the RMS curves in Fig. 3.11. Surface forcing is detailed in *Srinivasan et al.* [2017]. We note that the SWPAC solution atmospheric forcing contains daily variability in the winds and an analytically prescribed diurnal heat flux. This combination of forcing gives a relatively clean κ_v hourly response to diurnal heating (Fig. 3.11a) that drives a well-defined diurnal response in the submesoscale circulation (Fig. 3.11b).

The CCAL solution ($\Delta x = 0.1$ km, 60 vertical levels, Fig. 3.10b) is a child-nest of a U.S. West Coast solution set with an outer-grid ($\Delta x = 4$ km) that is nested down to $\Delta x = 1, 0.3$, and 0.1 km. The CCAL solution contains tides (prescribed in the outer parent grid) and atmospheric forcing (winds, surface heat, and freshwater fluxes) that is given by a 6-km Weather Research and Forecast (WRF) simulation. Compared to the SWPAC solution, the diurnal variability in CCAL is less idealized with hourly winds and heating given by WRF, though we restrict our analysis to

times of clean forcing and κ_v response (Fig. 3.11c).

CHAPTER 4

Nearshore Lagrangian connectivity

4.1 Introduction

Accurate characterization of the transport of material in the nearshore ocean (from the shoreline to $\approx$ 10 km offshore) is fundamental to interdisciplinary study or utilitarian application of coastal oceanography. In both scientific investigations (*e.g.,* larval/spore dispersal and its control on ecosystem dynamics [*Fujimura et al.*, 2017; *Jackson and Strathmann*, 1981; *Gaylord and Gaines*, 2000; *Siegel et al.*, 2003; *Castorani et al.*, 2017]) and coastal management application (*e.g.,* risk-assessment by prediction of pollution transport, [*Poje et al.*, 2014; *Boehm et al.*, 2002; *Uchiyama et al.*, 2014]) concise metrics summarizing transport outcomes are required. A useful metric physical oceanographers can exchange with other disciplines is a probability of material being transported from a source point to a destination, over a given time-scale since material release; referred to as the oceanographic 'connectivity' between the two sites, [*Mitari et al.*, 2009]. Confident connectivity estimates requires the capability to accurately sample the different types of oceanographic variability important for material transport. In coastal waters, this variability includes tides [*Suanda et al.*, 2018; *Ganju et al.*, 2011], wind-driven flows [*Lentz and Fewings*, 2012; *Feddersen et al.*, 1998; *Chapman*, 1987], internal waves [*Lerczak et al.*, 2003; *Noble et al.*, 2009; *Buijsman et al.*, 2012], surf-zone eddies and rip currents [*Feddersen*, 2014; *Kumar and Feddersen*, 2017; *Hally-Rosendahl and Feddersen*, 2016; *Spydell*, 2016], shelf-break fronts [*Chapman and Lentz*, 1994; *Zhang and Gawarkiewicz*, 2015], mesoscale eddies, and submesoscale fronts and filaments [*Uchiyama et al.*, 2014; *Romero*

et al., 2013; *Dauhajre et al.*, 2017]. Together, these dynamical regimes encompass a range of space ($O(0.01 - 10$ km)) and time-scales (O(hours - months)), that makes comprehensive sampling in the real-ocean extremely difficult. Similarly, the confidence in a regional connectivity answer grows with the sampled number of flow realizations. For these latter reasons, a realistic circulation model that can generate large ensembles of simulated Lagrangian trajectories is a pragmatic tool to investigate coastal transport pathways, mechanisms, and connectivity.

The ability of a coastal circulation model to simulate well the above-listed classes of currents (and their respective interactions) is primarily a function of the model resolution (and quality of the oceanic forcing datasets if realism is the goal). Generally, as resolution increases, so does the accuracy of the approximation to the equations governing oceanic flows. Recently, regional coastal models have been refined down to $\Delta x \approx O(10 - 100)$ m with grid-nesting techniques [*Mason et al.*, 2010]. Smaller-scale dynamical regimes, namely, turbulent submesoscale flows [*McWilliams*, 2016; *Thomas et al.*, 2008], are well-resolved at these fine resolutions.

Submesoscale flows are ubiquitous in most regions of the ocean, yet individually ephemeral, with life-spans on the order of hours to days. Investigation of submesoscale currents on the shelf is still rather nascent; the simulation in Chapter 2 demonstrates that they are prevalent on the Southern California shelf [*Dauhajre et al.*, 2017], and due to their strongly convergent surface flows, they can control nearshore dispersion [*Romero et al.*, 2013] and pollution transport on daily time-scales [*Uchiyama et al.*, 2014]. Observational evidence indicates control of Lagrangian trajectories by submesoscale currents in both open-ocean [*Lumpkin and Elipot*, 2010; *Berti et al.*, 2011] and coastal [*Ohlmann et al.*, 2017] regimes. These modeling and observational investigations indicate that resolving such small-scale currents on the shelf is potentially a necessity for accurate simulation of material transport in the nearshore.

Historically, many studies [*Mitari et al.*, 2009; *Xue et al.*, 2008; *Mayorga-Adame et al.*, 2017] simulate nearshore connectivity in regional domains with circulation models that have horizontal resolutions of $\Delta x \approx 1$ km; such models will poorly resolve the shelf and under-represent the fine-scale

currents (*e.g.,* submesoscale fronts and filaments) in the nearshore. [1] The results of these studies may then become 'datasets' that are utilized in ecological investigations. However, often there is a resolution gap between the ecological scales in question (*e.g.,* $O(100\text{ m})$) and physical simulation (1 km), *e.g.,* modeling the demographic connectivity of giant kelp [*Castorani et al.*, 2017].

It is not fully known what differences will arise between simulated Lagrangian trajectories from coastal circulation models with different horizontal resolutions (*e.g.,* 1 km and 100 m). To our knowledge no systematic comparison has been made of material transport in realistic coastal models at different resolutions. *Poje et al.* [2010] investigate the effect of model resolution on the pair-wise separation of simulated two-dimensional (horizontal) surface trajectories in mostly idealized configurations. They find that the fine-scale flow structures (*e.g.,* submesoscale) that arise with increased resolution drive local dispersion controlled by velocity differences at the local separation scale, which is consistent with a less steep velocity spectrum. Their investigation follows frameworks linking Lagrangian relative dispersion to turbulent mixing in the ocean [*LaCasce*, 2008].

In this study we investigate the controlling physical mechanisms on nearshore transport and the resolution sensitivity of coastal connectivity with a hierarchy of Regional Oceanic Modeling System (ROMS) [*Shchepetkin and McWilliams*, 2005] solutions for the Santa Barbara Channel (SBC). The SBC is historically a well-investigated region with its heavily studied coastal dynamics and giant kelp ecosystem; the investigations have fostered collaboration between physical and ecological communities. *Ohlmann et al.* [2012] provides observational motivation for our simulations; there, surface-drifters give evidence of high-flow variability (eddies, along- and cross-shore transport, and large variance in velocity magnitude) within a few kilometers of the SBC shoreline. Ecologically, the influence of nearshore flows on local SBC giant kelp population dynamics is not fully understood. *Cavanaugh et al.* [2014] find that the spatial synchrony of SBC giant kelp functions at spatial scales of less than 0.3 km; it is an open question whether inter-patch spore dispersal and settling controls small scale ($O(100\text{ m})$) synchrony. It is our intent that this study adds to coastal

[1] We note that this choice in resolution is sometimes made to allow for long-term simulation (O(years)) and/or larger spatial coverage.

transport literature in a generic sense, however, we envision localized application of the physical simulations and results.

We simulate currents in the SBC at $\Delta x = 1$, 0.3, 0.1, and 0.036 km with consistent realistic forcing and calculate three-dimensional (3-D) Lagrangian trajectories within a generic coastal connectivity setup (Section 4.2). We find a resolution sensitivity to connectivity estimates that is due to both larger nearshore horizontal and vertical displacement (mainly downwelling of near-surface particles) at higher-resolution (Section 4.3). In Section 4.4 we present examples of a variety of nearshore flow structures (exclusively resolved at high-resolution) responsible for rapid alongshore transport and dispersion. There, we present illustrative and statistical evidence of control by spontaneously formed shallow-water submesoscale fronts and filaments in early time downwelling and displacement of nearshore particles. Similarly, for particles converged into front and filament circulations, there is a dichotomy in 3-D and two-dimensional (2-D) trajectories that imprints onto differences in overall relative dispersion (Section 4.5).

One motivation for this study is to provide a check on the accuracy of historical connectivity studies (*e.g.,* [*Mitari et al.*, 2009]) and provide a guide for future ones with comparison of the $\Delta x = 1$ km and $\Delta x = 36$ m connectivity. This comparison can help guide biophysical studies requiring Lagrangian information. We ultimately offer cautionary evidence for the use of coarse-resolution coastal models to simulate nearshore transport of material. Equally important to biophysical application, our dynamical focus is rooted in exploring and illustrating newly resolved nearshore transport mechanisms that occur in higher resolution simulations. We prefer to focus on physical mechanisms of transport (*e.g.,* lateral convergence and downwelling by an ageostrophic secondary circulation in a dense filament or dispersion by a topographic wake) as opposed to interpreting the trajectories with blind diagnostics (*e.g.,* Lagrangian coherent structures [*Haller*, 2015]) that say little of the underlying shelf-dynamics at play. Overall, the results paint a picture of rapid material transport by highly variable, finer-scale currents in the nearshore that offers an alternative to dynamical conceptions known as “sticky water" [*Wolanski and Spangol*, 2000; *Wolanski and Kingsford*, 2014; *Restrepo et al.*, 2014] and the “coastal boundary layer” [*Nickols et al.*, 2012] that

hypothesize strong retention and weak dispersal in nearshore waters, approximately 1 km from the shoreline.

4.2 Experimental Setup

4.2.1 Circulation model

We utilize a family of nested ROMS solutions [*Shchepetkin and McWilliams*, 2005; *Mason et al.*, 2010] that focus on the Santa Barbara Channel for 40 days in the winter of 2006 (11/12/2006 - 12/22/2006). ROMS solves the hydrostatic Primitive Equations and uses a K-Profile Parameterization [*Large et al.*, 1994] for vertical mixing. Previous ROMS simulations are used to analyze coastal dispersion [*Romero et al.*, 2013] and wastewater effluent transport [*Uchiyama et al.*, 2014] studies, as well as phenomenological investigation of submesoscale currents on continental shelves [*Dauhajre et al.*, 2017]. All of these are realistic continental shelf ROMS solutions that *Kumar et al.* [2016, 2015] show accurately capture nearshore observed tidal and subtidal variability. A caveat about all these solutions, as well as the present one, is the lack of surface gravity waves, which can interact with shelf currents and drive surf-zone dynamics (*e.g.,* rip currents). Inclusion of surface wave effects in coastal models that resolve both the shelf and surf-zone is the subject of current model development and exploration, with *Uchiyama et al.* [2010] serving as a starting point. Therefore, we will mainly restrict our attention in this paper to areas of the shelf outside of the surf zone and make further comments on the potential importance of wave effects in Section 4.6.

Figure 4.1 displays the family of four nested solutions (R1km, R300m, R100m, and R36m) with resolutions of $\Delta x = 1$ km, 300 m, 100 m, and 36 m and vertical levels N=60, 50, 50, and 50, respectively. This nested family of solutions is further nested in an outer parent grid ($\Delta x = 4$ km) that spans the entire U.S. West Coast [*Renault et al.*, 2019]. Additional tidal forcing is prescribed in the R1km grid with the TPXO7.1 global tidal prediction model [*Egbert et al.*, 1994] that gives tidal

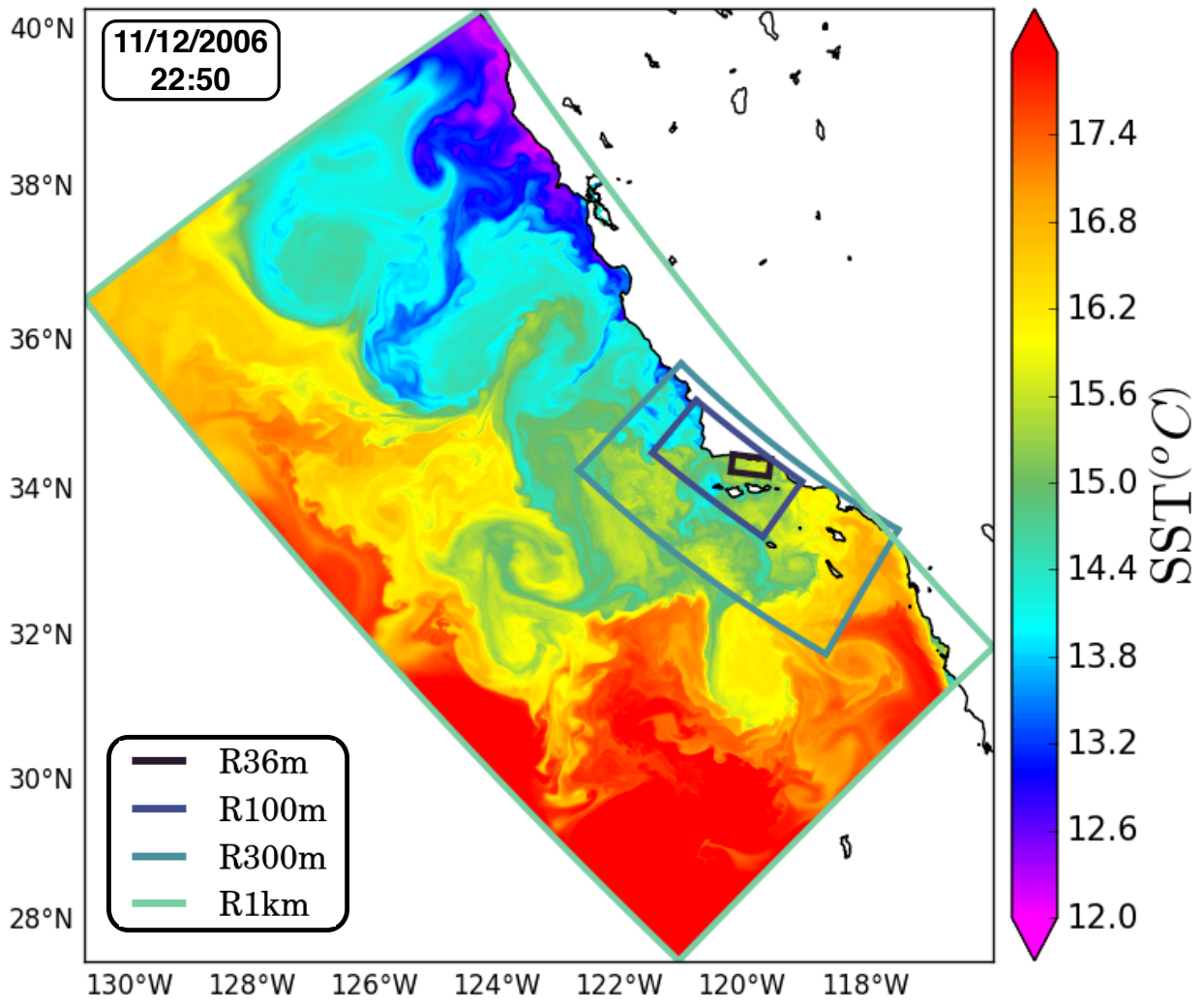

Figure 4.1: ROMS grid nesting hierarchy for the Santa Barbara Channel region. The four simulations allow investigation of realistic, coastal Lagrangian transport at various resolutions in the Santa Barbara Channel beginning with a $\Delta x = 1$ km (R1km, light green) simulation of a large portion of the U.S. West Coast (forced by an outer $\Delta x = 4$ km solution, not shown). The subsequent nests systematically focus in on the Santa Barbara Channel: $\Delta x = 300$ m (R300m, teal), $\Delta x = 100$ m (R100m, blue), and $\Delta x = 36$ m (R36m, black). Sea surface temperature in each simulation is plotted as a 30 min. average on 11/12/2006 22:50 (local time).

amplitude and phases for 10 tidal constituents (M_2, S_2, N_2, K_2, K_1, O_1, P_1, M_f and M_m). The tidal variability is passed onto the child nests (R1km-R36m) at the lateral boundaries with boundary conditions from the respective parent grid (*e.g.,* R300m provides the boundary condition for R100m). Realistic atmospheric forcing is prescribed for all nests with a Weather Research and

Forecast (WRF) simulation [*Michalakes et al.*, 1998] at 6 km resolution. The WRF forcing provides synoptic winds, surface heat, and freshwater fluxes. All solutions contain a wind-current coupling paramezation for the surface that gives a more realistic eddy-kinetic energy level [*Renault et al.*, 2016].

4.2.2 Lagrangian coastal connectivity

We pose a generic coastal connectivity experiment by splitting the SBC coastline into 19 nearshore sites where Lagrangian particles are released (Fig. 4.2). These sites act as the source and destination sites in our study, and they allow us to focus on nearshore transport pathways that are most prevalent in an along-shore direction. In this setup the coastline and nearshore waters are divided into semi-circular coastal sites defined to avoid overlap between adjacent sites. While the site definitions are somewhat arbitrary, we are not primarily concerned with transport between specific locations, but rather with the general geographic connectivity of the region (eastward vs. westward connections, headland vs. bay dispersion or retention, and short vs. long distance transport), the important processes controlling connectivity, and how and why connectivity can vary across model grid resolution. Site numbers range from 0 to 18, with 0 on the eastern-most end of the domain near Carpenteria, and 18 the furthest to the west (Fig. 4.2). The nearshore sites extend from the shoreline to approximately 4 km offshore with none extending past the 100 m isobath.

The frequency of particle releases is designed to sample as many independent flow realizations as possible: 100 particles are released from each of the 19 coastal sites 3 times a day for the 40 day time period (beginning on 11/12/2006 22:50 and ending 12/22/2006 22:20) resulting in 228,000 total particles advected in each simulation. A sensitivity test (not shown), performed with R36m velocities, demonstrates that doubling the total number of particles does not substantially change the connectivity estimates. Individual particle locations for each release (Fig. 4.2, black dots) are prescribed to have consistent initial positions across the four simulations.

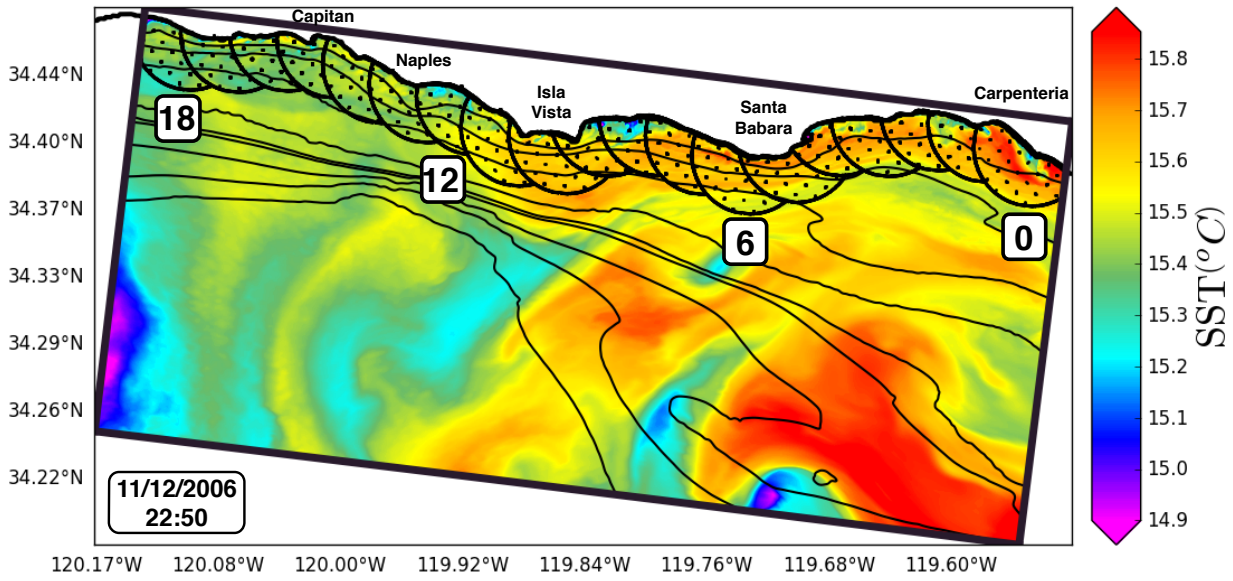

Figure 4.2: Initial particle positions (black dots) for the coastal connectivity experimental setup for the Santa Barbara Channel. Particles are initialized at $z = -2$ m consistently across the four simulations (interpolated onto each grid by latitude and longitude positions). Nineteen coastal source (and destination) sites are delineated by the black lines with the numbering convention indicated. Site 0 begins in the eastern-most portion of the domain, near Carpenteria, and the numbers increase sequentially to the west. Three times a day, each site is re-filled with 100 particles for the 40-day simulation period, resulting in 228,000 total particles. Sea surface temperature for the R36km solution is shown in color as a 30 min. average on 11/12/2006 22:50 (local time) and local bathymetry in the thin black contours. Several along-shore locations are indicated to better orient the reader.

All particles are neutrally buoyant, initialized at $z = -2$ m, and advected by the 3-D velocity field. In Section 4.5, we analyze an analogous experiment in R36m where particles are held at $z = -2$ m to compare 2-D and 3-D trajectories and dispersion. In both 2-D and 3-D cases, Lagrangian trajectories are calculated with linear interpolations of velocities in time and space from the archived gridded velocity field from ROMS.

Accurate calculation of Lagrangian trajectories in submesoscale flows (which evolve on hour to daily time-scales) requires a relatively high temporal sampling frequency for the velocity fields. Particles are advected with a 30 min. averaged output of the ROMS solutions for all simulations.

This is sufficient to accurately capture submesoscale transport; however, it forces us to restrict our analyses to a relatively short, 40-day time-period due to computational cost and limited data storage. This is in contrast to a historical predecessor to our study [*Mitari et al.*, 2009], which calculates connectivity in a $\Delta x = 1$ km ROMS simulation of the Southern California Bight over multiple years. Despite the short time-period for the simulation, we are mainly investigating short time-scale mechanisms of along-shore transport induced by better resolved physics with the higher grid resolutions in R100m and R36m (*e.g.,* submesoscale fronts).

4.3 Resolution Comparison

4.3.1 Connectivity statistics

In this section we compare connectivity results across the four simulations (R1km, R300m, R100m, and R36m). Pathways are possible between any given source (i) and destination (j) site with a connectivity for a given i, j pairing ($C_{ij}(t)$):

$$C_{ij}(t) = \frac{n_{ij}(t)}{N_i}\frac{A_i}{A_j}\ , \tag{4.1}$$

where $n_{ij}(t)$ is the number of particles sourced at site i that arrive at destination j at a time t (where t is the time since particle release); N_i is the total number of particles released at source i; and A_i and A_j the areas of the source and destination sites, respectively. C_{ij} is unit-less and quantifies particle density (number of particles per km^2) arriving at a destination j $\left(n_{ij}/A_j\right)$ relative to the total particle density released from a source site i (N_i/A_i).

We quantify connectivity for 40 days (sampling all possible flow realizations as seen by the 120 particle releases over the simulation period). There is a decrease in time of the total fraction of remaining particles in the R36m domain (Fig. 4.3). In the R36m solution approximately 20% of particles remain after 10 days, with the coarser resolution solutions exhibiting a slower exit of particle density with more than 40% in R1km after 10 days. In the resolution comparisons, R36m

trajectories serve as the 'truth' standard, and the focus is on short-time (0–10 days) variability in the connectivity when particle density is not yet too depleted in the R36m domain.

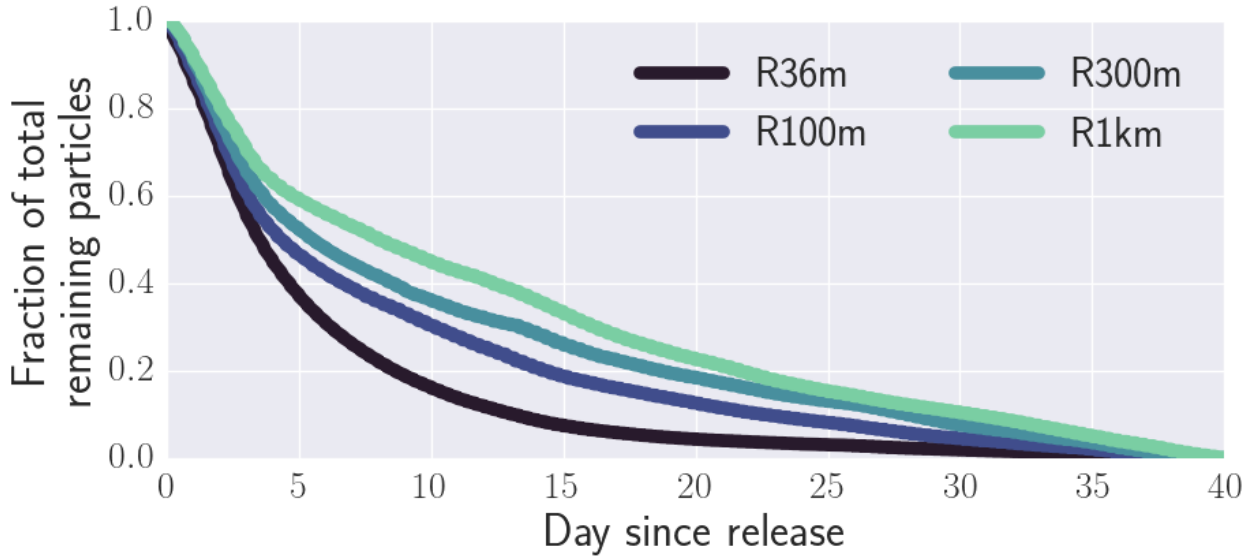

Figure 4.3: Fraction of total remaining particles in the R36m domain (Figure 4.2) as a function of time since release for all four resolutions. Notice the coarser resolution solutions are more retentive.

Figure 4.4 displays connectivity matrices for R1km, R300m, R100m, and R36m plotted as temporal means over specific advective time periods (0–4 days, 4–10 days and 0–40 days). R36m (Figure 4.4, top row), exhibits a strong initial pulse (days 0–4) of connectivity between adjacent or near adjacent i, j pairs, with a preference for westward transport, primarily due to a westward mean current on the shelf. The imprints of the initial pulses of particle delivery to the west are apparent in later times (days 4–10), with a decay in connectivity for most sites with time. In the full time-mean (days 0-40, right column in Fig. 4.4), the coarser resolution cases overestimate self-connection and connections between adjacent sites, displayed most drastically in R1km.

Figure 4.5 quantifies the sensitivity with the difference of the temporal root-mean square (RMS) of connectivity relative to R36m (*e.g.*, $\Delta C = \mathrm{RMS}[C_{ij}^{R36m}(t)] - \mathrm{RMS}[C_{ij}^{R1km}(t)]$), where the RMS is taken over time periods days 0–4 and 4–10. At early time (days 0–4), the coarser resolution solution (notably R1km, bottom row Figure 4.5) exhibits an underestimation of the connectivity between nearby sites ($\Delta C > 0$) as well as a strong overestimation of self-connection ($\Delta C < 0$).

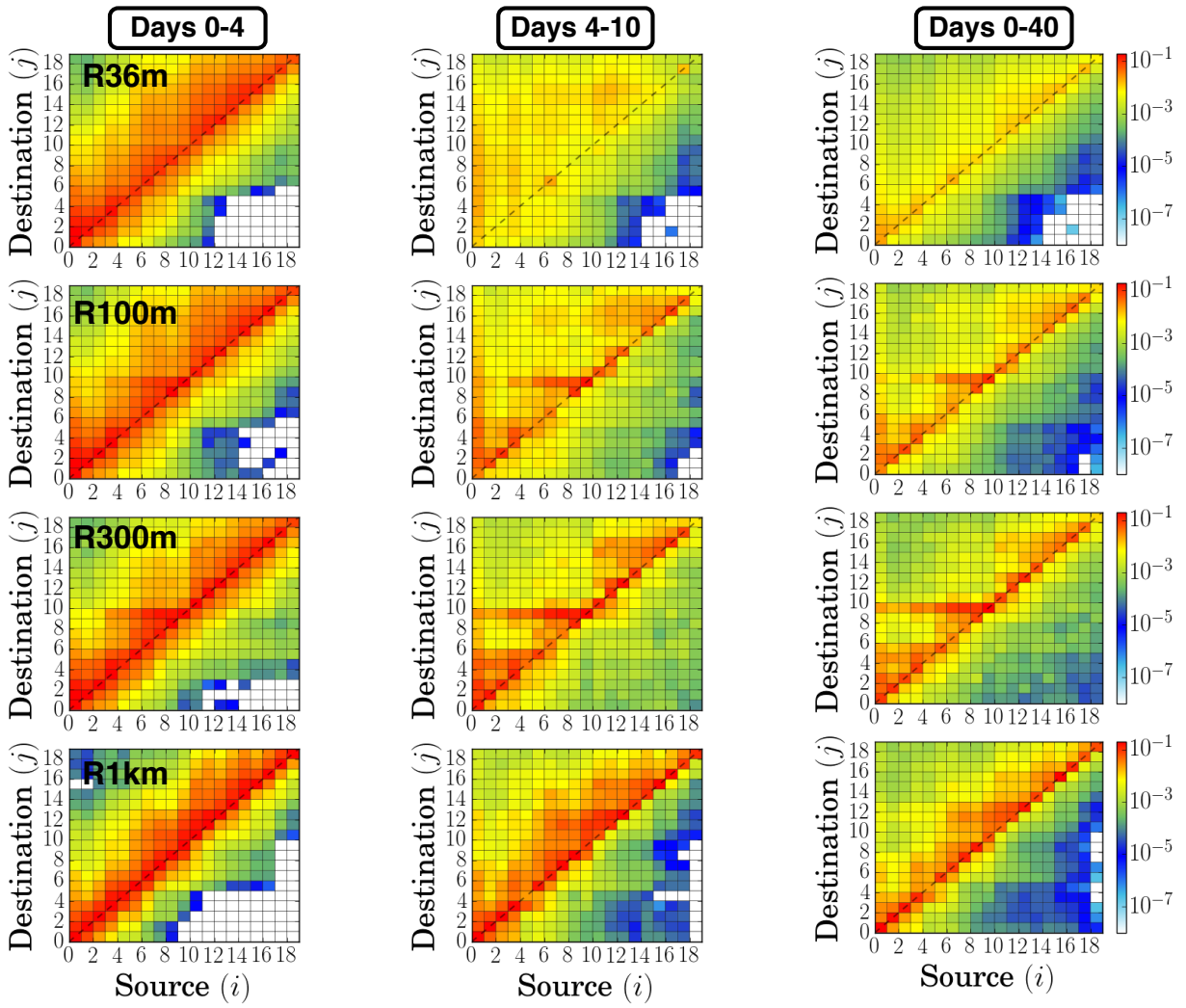

Figure 4.4: Mean connectivity matrices for R1km, R300m, R100m, and R36m (rows). The mean connectivity for each (i, j) pairing is calculated over multiple time-periods (columns); connectivity C_{ij} is defined in Eq. (4.1) and quantifies the particle density (number of particles per km^2) arriving at a destination relative to the total particle density released from a source site. Individual columns represent a time mean over days (left) 0-4, (middle) 4-10, and (right) 0-40. Color-scaling is the same in every panel. Note the relatively increased spread in connectivity around the 1:1 line (near site connections) of R36km compared to R1km for days 0-4. Conversely, R1km exhibits stronger retention in self-connections and adjacent sites at later time (days 4-10).

The magnitude and spread of this difference grows with decreasing resolution. At later time (days 4–10), R1km, R300m, and R100m exhibit a retentive bias in self- and short-distance connections

(Fig. 4.5, right column).

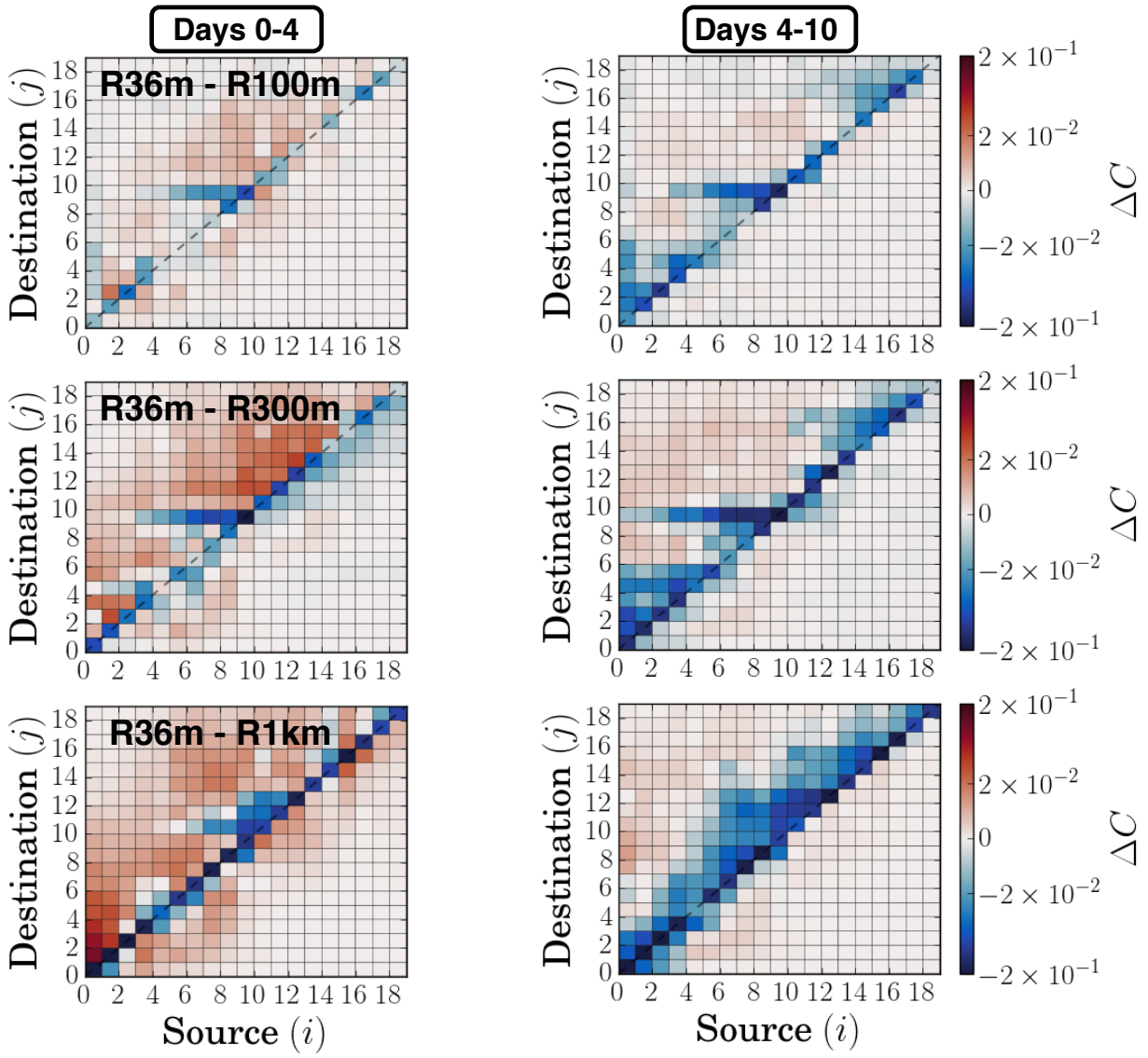

Figure 4.5: Difference in the temporal root-mean square (RMS) of connectivity (ΔC) between R36m and the indicated coarser grid (rows). The RMS of $C_{i,j}$ for each solution is calculated over a time-period relative to a time mean: (left) days 0-4 and (right) days 4–10. Color-scaling is the same in every panel. Here, $\Delta C > 0$ indicates an underestimation of particles in a given i, j pairing, and $\Delta C < 0$ indicates an overestimation (*i.e.,* retentive bias).

To illustrate the temporal variability of types of connections (*e.g.,* westward, eastward, short, and long) and their behavior at differing resolution, we quantify averaged connectivity for ensembles

of (i, j) pairings ($\langle C \rangle$) for all resolutions (Figure 4.6)[2]. Here, we conditionally sample connectivity in the westward ($i < j$, Figure 4.6a,c) and eastward ($j < i$, Fig. 4.6b,d) directions for 'short' and 'long' distances. The distance classification is defined by the difference in site numbers: $|i-j| < 5$ for short and $5 \leq |i-j| \leq 12$ for long connections (Fig. 4.2).

Expectedly, short-distance connections exhibit a maximum in connectivity at very short time-scales ($\sim$ 1 day), with a very rapid rate of increase relative to longer-distance connections. For short-distance connections, there is generally an underestimation of the maxima in connectivity and a retentive bias at coarser resolution (most notably in R1km; Fig. 4.6a,b). We note that R300m does display the strongest connectivity for short-distance eastward connections; however, we cannot rule out sampling variability as a cause of this anomaly, further discussed in the following paragraph. At longer-distance (Fig. 4.6c,d), the magnitude of connectivity is expectedly weaker (especially for eastward connections against the mean flow; Fig. 4.6d), but the time-scale of retention is slightly longer. Similar to the short-distance connections, R1km underestimates the connectivity maximum and displays very weak particle 'flushing' from nearshore sites, indicated by the slower decay rate in $\langle C_{ij} \rangle(t)$.

Because of the short time period of simulation (40 days), a concern is that the connectivity metrics calculated for our family of solutions may be realization-dependent and not general. This is a legitimate concern in the face of our computational and storage limitations. However, sensitivity tests (not shown) that calculate the connectivity for various time-periods in the simulation (*e.g.,* compute separate connectivity for particles released in 5 day intervals) indicate that the results and interpretations given by the metrics in Fig. 4.4, 4.5, and 4.6 generally hold for these shorter time intervals, with exceptions of anomalous behavior (*e.g.,* R300m in Fig. 4.6b).

The results in Figs. 4.4, 4.5, and 4.6 lead to a general interpretation that at coarser resolution, simulated nearshore connectivity will be weaker and more retentive than higher resolution simulations. The rest of the study investigates the dynamical reasons for this sensitivity and focuses

[2]Discussion of the connectivity for the R36m 2-D connectivity in Fig. 4.6 (black dashed line) is left for Section 4.5

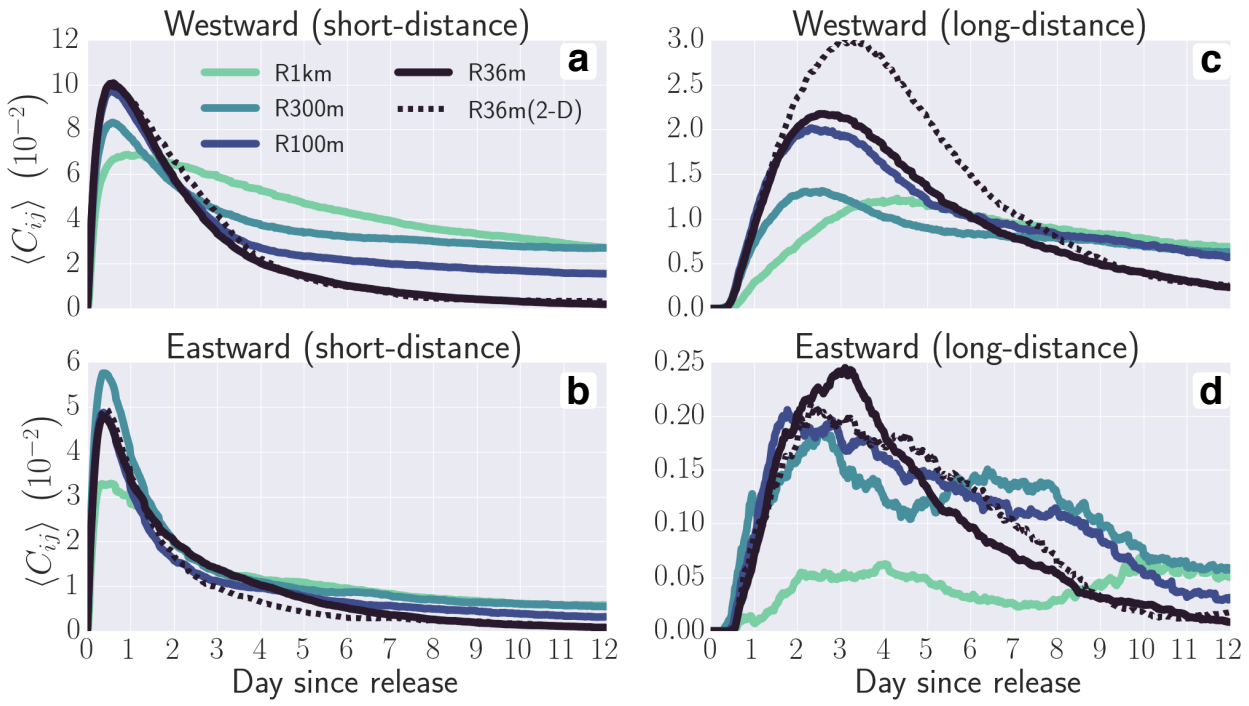

Figure 4.6: Twelve-day time-series of connectivity averaged over (i, j) pairings based on direction and distance: (a,c) westward ($i < j$) and (b,d) eastward ($i > j$) connections for (a,b) short-distance ($|i - j| < 5$) and (c,d) long-distance ($5 \leq |i - j| \leq 12$). The temporal axis corresponds to the day since particle release. Connectivity curves are given for the 3-D resolution comparisons (solid) and a 2-D case in R36m (black dashed). Note the general agreement between R36m and R100m, and disagreement of R1km in all cases, expressed as an underestimation of connectivity at early time and an overestimation of retention at late time.

on control on Lagrangian transport by small-scale and fast-evolving nearshore physics that are best simulated at high-resolution ($\Delta x \lessapprox 100$ m).

4.3.2 Nearshore horizontal and vertical displacements

Here, we explain the resolution sensitivity to nearshore connectivity by examining the horizontal displacement and vertical transport of individual particles that make journeys between source and destination sites. Displacement is defined in along-shore (A_a) and cross-shore (A_c) direc-

tions, relative to a bathymetric unit-gradient vector ($\boldsymbol{h}_g = \nabla h/|\nabla h| = \hat{h_x} + i\hat{h_y}$, analogous to dispersion metrics in [*Romero et al.*, 2013]) where the absolute displacement $\boldsymbol{A}$ at time t is defined as the displacement relative to a position at time t_0 ($\boldsymbol{A} = \boldsymbol{x}(t) - \boldsymbol{x}(t_0)$), where $\boldsymbol{x}$ is the particle position.

Figure 4.7 displays the relationship between the closest particle distance to the shoreline (Fig. 4.7, left column) or particle depth (Fig. 4.7, right column) upon arrival at a destination site versus the along-shore displacement of these particles two days after arrival at the site (where the displacement is calculated relative to the particle position upon site arrival). The scatter plots take data points of particles sourced at nearshore sites 1, 3, 4, 5, 6, 7, 9, 12, 15 (Fig. 4.2) that make along-shore connections to any other potential nearshore site for time periods of 1 to 10 days after release; in essence, we sample a majority of the particles that comprise the largest connectivity signals in the time-periods of interest, 1–10 days after particle release. We do not show an analogous metric of cross-shore displacement for brevity, but note that it exhibits similar functional dependencies with respect to particle distance to shoreline and particle depth.

All solutions exhibit a decrease in displacement when particles move to within a distance of Δx to the shoreline, where Δx is the model resolution (indicated for each case by the vertical dashed lines in Fig. 4.7 left column). Numerically, this drop-off is due to the solid wall boundary condition at the land-mask that imposes zero-normal and no-slip flow at the wall [*Dong et al.*, 2007; *Shchepetkin and O'Brien*, 1996]. This is interpreted dynamically as an under representation of flow variability nearshore at coarser resolution. In R1km, there is a clear misrepresentation of material transport on the shelf in the waters approximately less than 0.8 – 1 km from the shoreline. More nearshore variability is resolved at higher resolution and can indeed drive large displacements at distances close to shore (≈0.05 – 0.8 km). The increase in nearshore displacement is present in R300m, R100m, and R36m with a resolution limit on minimum particle distance to the shoreline. In the R36m solution large displacements can occur for particles that are within 100 m from the shoreline [3] (Fig. 4.7, left column, top row).

[3] We note that a surf zone (absent in our simulations) could exist within 200 - 300 m from the shoreline so we do

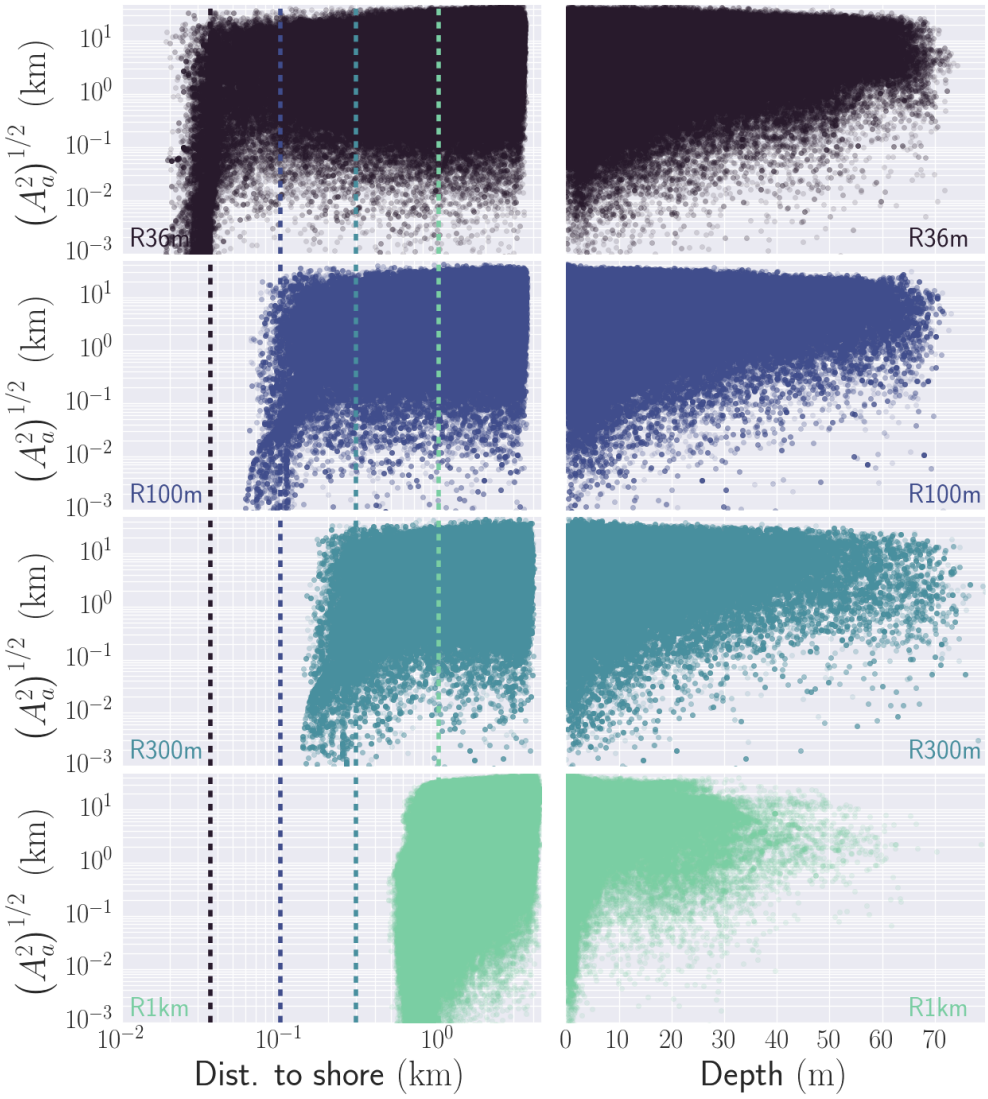

Figure 4.7: Scatter plot of (left column) minimum particle distance to the shoreline and (right column) depth upon arrival at a coastal site vs. along-shore displacement (plotted as $\sqrt{A_a^2}$) 2 days after arrival at the site for the four resolutions (rows: R1km (light green), R100m(teal), R100m(blue), and R36m (black)). Data points are plotted for particles sourced at nearshore sites 1,3,4,5,6,7,9,12,15 that make along-shore connections to any other potential nearshore site (0 to 18) for time periods of 1 to 10 days after release (site arrivals are sampled at 4 hour intervals). Only particles that remain in the R36m domain 2 days after arrival are used. Vertical dashed lines on the left-panels indicate the model resolutions. Note the deeper vertical transport at higher resolution as well as the resolution-dependent drop-off in along-shore displacement in all solutions, most notably in R1km, which cannot resolve the large displacements that occur inshore of ~800 m.

Analogous to the behavior of particles at higher resolution to both move closer to the shoreline and experience larger displacements at these nearshore locations, particles arriving at nearshore sites can move to deeper depths, in larger numbers, as the resolution increases (Fig. 4.7, right column). In general, R36m, R100m, and R300m display the same maximal depth of arrival (≈70 m). R1km greatly underestimates this downwelling. Interestingly, particles that arrive at nearshore sites at large depth can travel far after arrival (Fig. 4.7 right-panels).

4.4 Transport by Turbulent Nearshore Currents

4.4.1 Illustrative events

We now illustrate how nearshore dynamics that preferentially arise at high resolution can impact the horizontal and vertical transport of particles. Three sequences of snapshots (Fig. 4.8, 4.9, and 4.10) allow visualization of transport events in the R36m simulation. Each sequence displays a subset of selected particles for clear visualization, rather than all particles being advected in the domain. We note that these few illustrations do not represent all potential transport pathways. Rather, they are chosen to highlight the role of smaller-scale, turbulent shelf-dynamics that arise as model resolution increases: narrow along-shore jets, topographic wakes, and shallow-water submesoscale fronts and filaments. Our sense is that these examples are typical, but not a comprehensive set.

Figure 4.8 presents group of particles advected from east to west in a narrow-band on the shelf over a period of three days. The particles begin near Carpenteria, with most near the surface (light-green dots, Fig. 4.8 top). In the next two snapshots (middle two panels, Fig. 4.8), the particles are strained into a narrow-band along the shelf, and quickly advected past the Santa Barbara and Isla Vista headlands. Along the way a fraction of particles are downwelled (blue dots)

not attempt to over analyze dynamics within this region.

and later dispersed as they encounter anticyclonic vortices generated at the Isla Vista headland due to the fast, westward along-shore flow on the shelf. Fast, narrow, along-shore pulses like this resemble "Lévy flights" [*Solomon et al.*, 1993] and are common in the R36m and R100m trajectories.

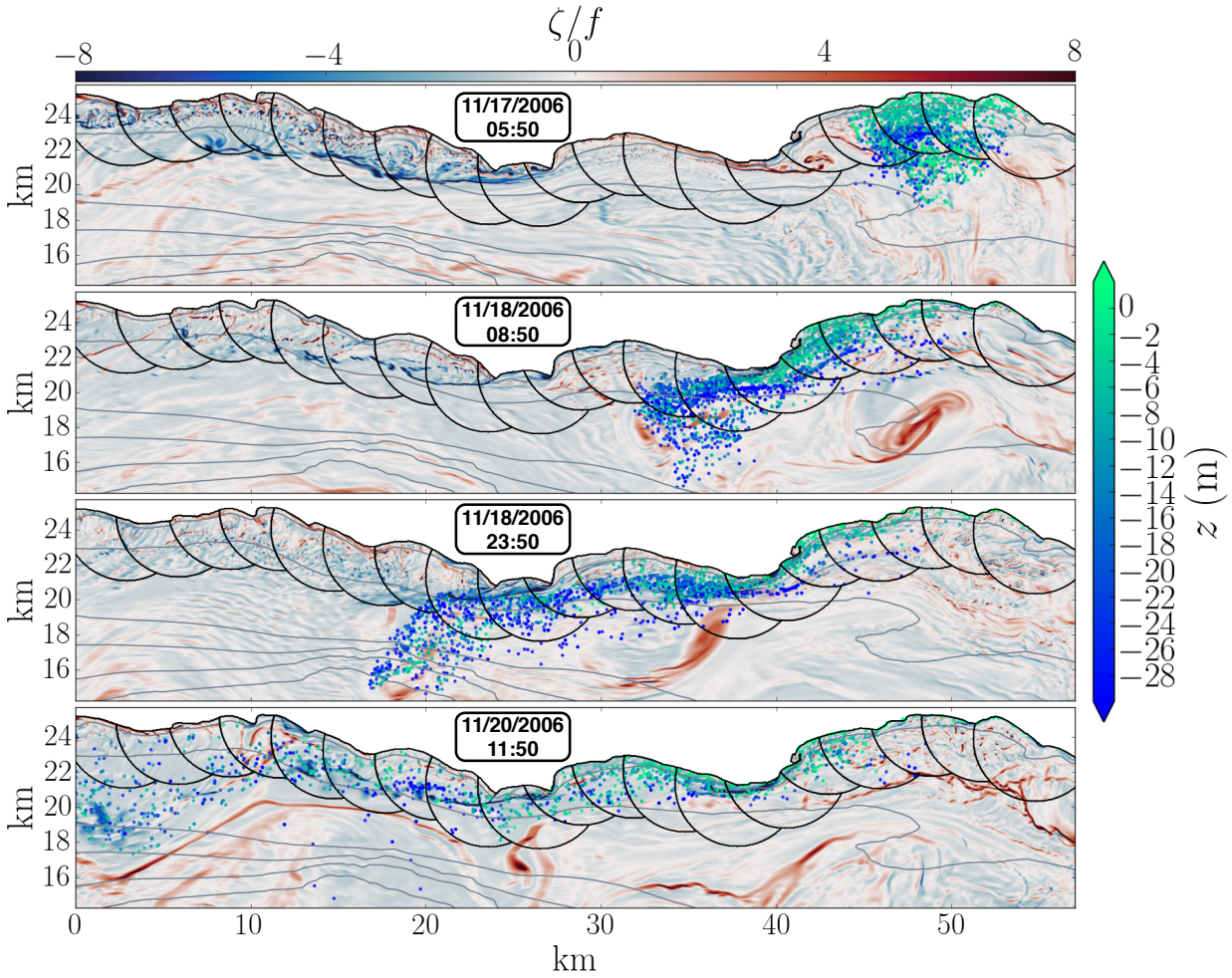

Figure 4.8: Snapshot sequence illustrating fast along-shore transport of a batch of particles beginning in the eastern portion of the domain near Carpenteria. Surface relative vorticity is indicated by the colored contours, particle depth is colored onto each particle corresponding to the colorbar on the right and the local time for each snapshot is indicated at the top of each panel. Particles advected in a nearshore band to the west over the course of three days (11/17/2006 – 11/20/2006) are primarily transported by a narrow along-shore current (middle two panels), are downwelled along their trajectories, and are dispersed by anticyclonic headland wakes generated from topographic interaction with the westward mean flow (bottom two panels).

Figures 4.9 and 4.10 illustrate rapid convergence and downwelling of particles by spontaneously formed submesoscale fronts and filaments on the shelf. While such features have a statistical preference of aligning in an along-shore direction on the shelf [*Dauhajre et al.*, 2017; *Romero et al.*, 2013], we give two examples where the front or filament is aligned either along-shore (Fig. 4.10) or cross-shore (Fig. 4.9). As mentioned in Section 4.1, these currents can be identified by their strong cyclonic vorticity ($\zeta = \frac{\partial u}{\partial y} - \frac{\partial v}{\partial x} > 0$) and surface convergence ($\delta = \frac{\partial u}{\partial x} + \frac{\partial v}{\partial y} < 0$) that manifest as thin features in ζ or δ, which trace out strong surface density gradients. It is common to normalize both ζ and δ by the Coriolis frequency f, which equates to a local measure of Rossby number Ro.

In Figure 4.9 a group of particles just offshore (approximately 6 km from the shoreline) of the Isla Vista headland encounters a cross-shore aligned submesoscale dense filament (*i.e.,* a local maxima in density, not shown). Here, the feature is indicated by its large cyclonic (positive) relative vorticity (red streak extending across isobaths). In the first snapshot the particle cluster is mainly near the surface and dispersed around the nascent filament. As time progresses, and the filament's circulation intensifies (Fig. 4.9), the particles are converged onto the cyclonic vorticity line, and very rapidly downwelled (top right and bottom left Fig. 4.9); note that the entire time-span of the sequence is 16 hours. Once the particles have been downwelled, they are dispersed and are transported by larger-scale flows at depth (Fig. 4.9, bottom right).

Fig. 4.10 illustrates an analogous example of the latter process, but for an along-shore aligned structure, very close to shore (within a span of nearshore sites). In this example the majority of the particles in the first panel are in their initial positions as the time coincides with a particle release. Here, as in Fig. 4.9, the particles quickly converge and downwell into the submesoscale structure that results in particles transported down to below 20 m only 7 hours after their initialization.

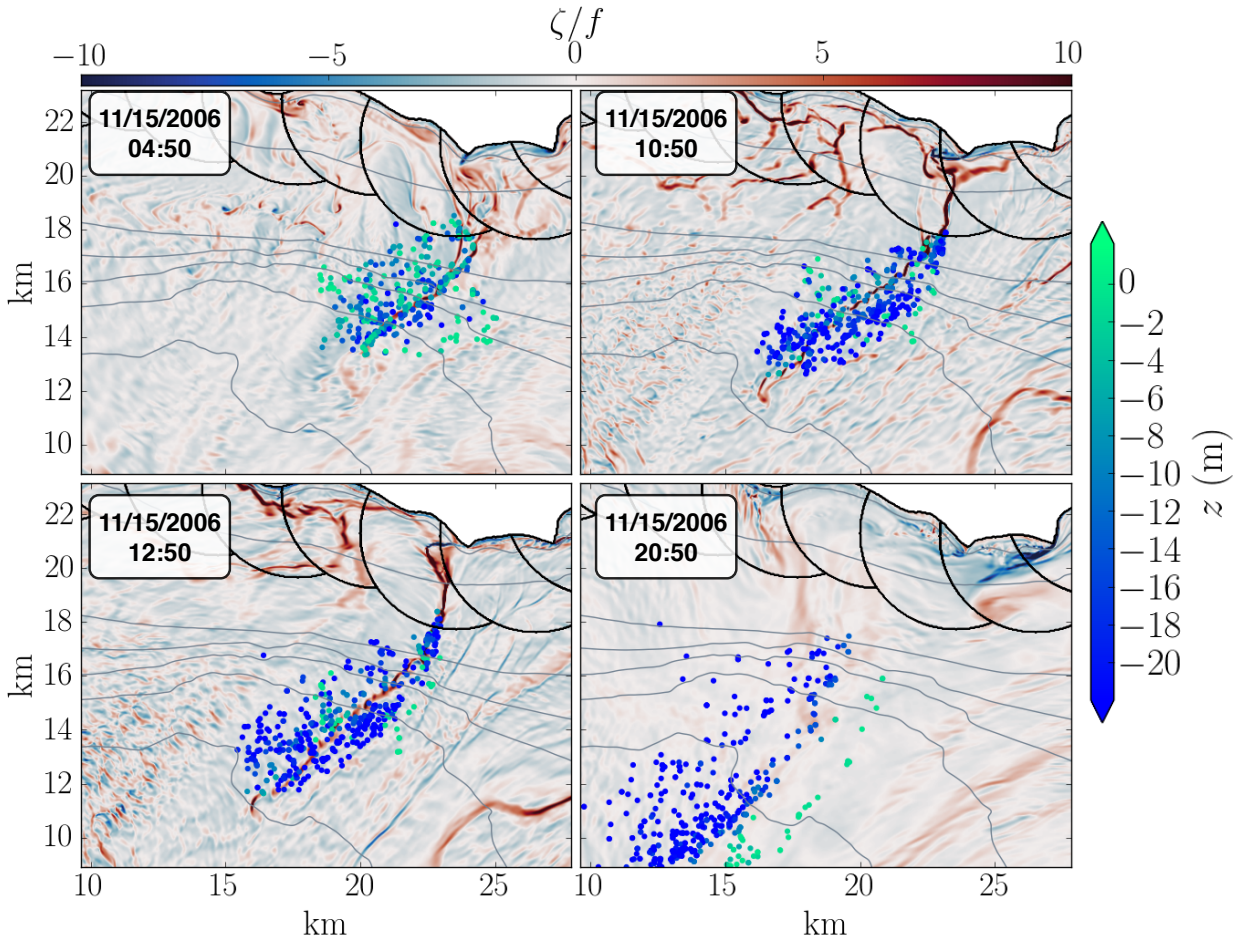

Figure 4.9: Snapshot sequence illustrating extremely fast surface convergence and downwelling of a selected batch of particles by a cyclonic submesoscale structure off the Isla Vista headland. Surface relative vorticity is indicated by the colored contours, and particle depth is colored onto each particle corresponding to the colorbar on the right. The sequence begins on 11/15/2006 04:50 (local time) with the time for each snapshot indicated in the upper-right hand corner of each panel. Note the increased depth of nearly all particles after convergence along the feature (11/15/2006 12:50), a consequence of ageostrophic, downwelling secondary circulation of the submesoscale feature. Similarly, note the increased dispersal in the final frame after downwelling, once particles are released at depth from the convergent secondary circulation structure.

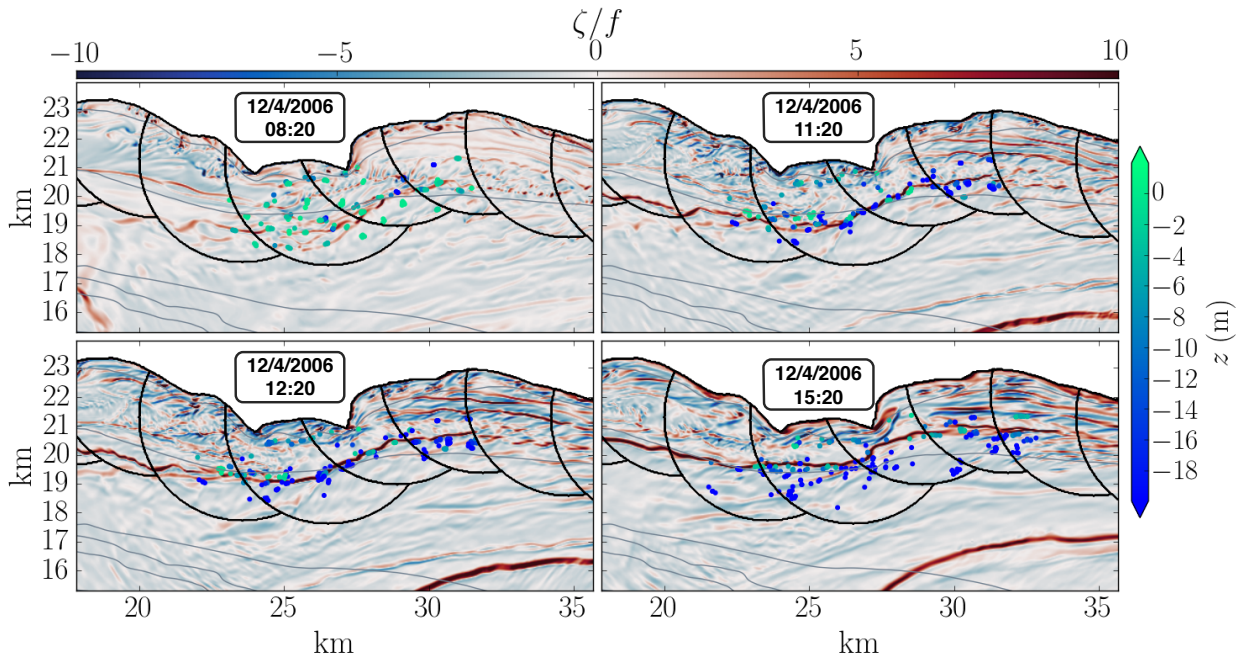

Figure 4.10: As in Fig. 4.9 but for a separate batch of particles close to their initialization time. Surface relative vorticity is indicated by the colored contours, and particle depth is colored onto each particle corresponding to the colorbar on the right. The sequence begins on 12/4/2006 08:50 (local time) with the time for each snapshot indicated in each panel. As in Fig. 4.9, the particles are downwelled to below 20 m over a fast time-period (5-6 hours) by a cyclonic, convergent submesoscale current, in this case, aligned in a along-shore direction.

4.4.2 Importance of nearshore submesoscale dynamics

Figures 4.9 and 4.10 provide anecdotal evidence of rapid transport (importantly in the vertical) by submesoscale currents on the shelf. In this aspect they are analogous to illustrations in the open-ocean [*Gula et al.*, 2014]. Here, we present statistical evidence that these spontaneously formed, small-scale, turbulent currents are responsible for the majority of downwelling of near-surface particles in the first hours after their release by conditionally sampling particles that go to depth quickly after release (Fig. 4.11).

Fig. 4.11 isolates particles that make connections from nearshore sites 1, 3, 4, 5, 6, 9, 12, 15 to

any other potential site with arrival times of 1 to 10 days (analogous to Fig. 4.7) that also have depths below 20 m by a time 24 hours after their release. We separate particles that fit these latter arrival and depth criteria into those that are initialized by at least a distance of 750 m offshore (Fig. 4.11, solid lines), and those that start closer to the shoreline (Fig. 4.11, dashed lines). Particle-averaged vorticity (Fig. 4.11a), divergence (Fig. 4.11b), depth (Fig. 4.11c), and along- and cross-shore displacement (Fig. 4.11d) in a time-frame relative to particle release allow the inference of controlling dynamical regimes.

Figure 4.11a,b indicates a systematic, early time, control on material transport by ephemeral shallow-water submesoscale currents (for particles that go to depth: Fig. 4.11c). Particles that are initialized away from the shoreline (*i.e.,* away from lateral shear at the coastal boundary), that also make it to 20 m or deeper after 24 hours, are (on average), immediately trapped into cyclonic ($\zeta/f > 0$) and convergent ($\delta/f < 0$) currents on time-scales of 4-6 hours after release (Fig. 4.11a,b solid lines). The cyclonic, convergent signal, a signature of submesoscale front and filament circulations, confirms that the process illustrated in Fig. 4.10 is generic for nearshore material transport on the shelf in higher-resolution simulations.

For trajectories starting closer to shore (Fig. 4.11a,b dashed lines), due to a primarily westward mean flow, the particles start in an anticyclonic shear flow that is also convergent with down-welling. In the shallow-water close to shore, the direction of the mean flow is fairly uniform with depth and generates a bottom Ekman current that transports water offshore with downwelling resulting from mass conservation. Conversely to the particles further offshore that only feel the cyclonic vorticity for ≈ 6 hours, the particles closer to shore remain in the anticyclonic flows for approximately one day. This is indicative of along-shore transport that hugs the shoreline within the anticyclonic shear zone. Regardless of initial particle distance to the shoreline, the particles on average remain in a weakly convergent flow 48 hours after release.

Figure 4.11d quantifies the along- and cross-shore displacement of these particles. Agreeing with the anisotropic findings of *Romero et al.* [2013], the along-shore displacements are greater than

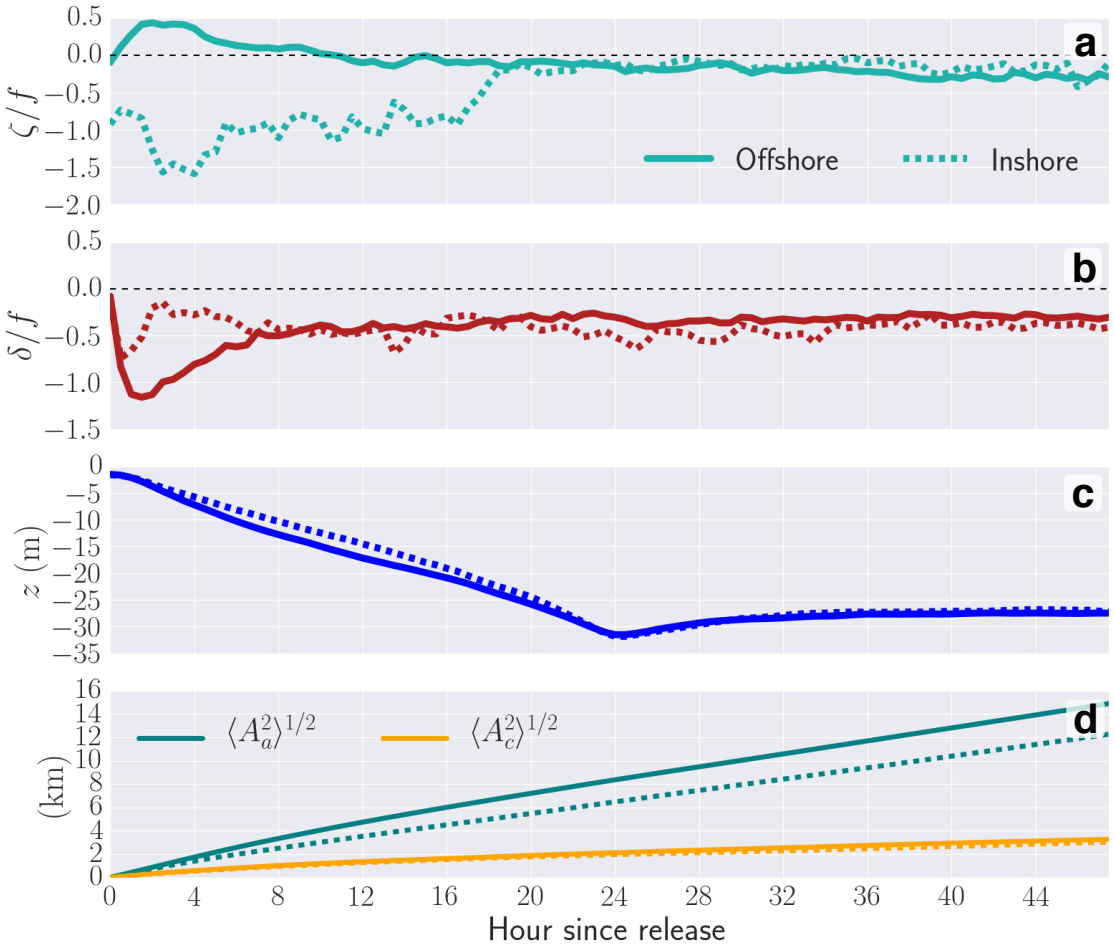

Figure 4.11: Two-day time-series of interpolated (a) relative vorticity (b) divergence, (c) depth and (d) along- (A_a, teal) and cross-shore (A_c, orange) displacement (plotted as $\sqrt{A^2}$) for conditionally sampled particles in the R36m solution that have depths greater than 20m 24 hours after release. We separate these particles into those that are initialized (solid) offshore (13% of total particles released at indicated sites) and (dashed) inshore of 750m from the shoreline (4% of total particles released at indicated sites). The time-series are generated for particles sourced at nearshore sites 1,3,4,5,6,9,12,15 that make along-shore connections to any other potential nearshore site (0 to 18). Only particles that meet the depth criteria and make connections between time periods of 1 to 10 days after release are sampled (with arrivals sampled at 4 hour intervals). Hour 0 corresponds to the release time of the particles, and the time-series are plotted for 2 days of advection time. Note the cyclonic and convergent signal for offshore particles (panels (a) and (b) solid lines) in the early time after release, an indication of immediate control and downwelling by nearshore submesoscale circulations.

cross-shore for all the particles sampled here. Both displacement curves follow ballistic trajectories ($A \sim t$) 0-2 days after release, indicating control by the short-time persistence of initial velocities. Particles that begin closer to the shoreline (Fig. 4.11d, dashed) experience less along-shore displacement than those that are initialized further away from shore (Fig. 4.11c, solid).

These results indicate that particles making trips between nearshore sites can be heavily influenced by submesoscale (with Ro $\sim \zeta/f, \delta/f > 1$) currents at the outset of release near the surface ($z = -2$ m). Particles that are initialized away from the shoreline can be clustered into cyclonic, convergent submesoscale fronts and filaments (*e.g.,* Fig. 4.10) and downwelled, with respective clusters ballistically advected by larger-scale (dominantly along-shore) flows at depth in the day after downwelling. The analogous metric, as in Fig. 4.11 for R100m and R300m (not shown for brevity), displays similar behavior, indicating that this mechanism is partially resolved in those simulations. This is also indicated by the general agreement in the depth-displacement scatter plots in Fig. 4.7, right. As the resolution decreases, the respective early time peaks of particle-averaged vorticity and divergence become flatter, and more prolonged.

4.5 3-D vs. Surface 2-D Trajectories

In many studies of Lagrangian trajectories [*Poje et al.*, 2010; *Haza et al.*, 2012] it is common to take a two-dimensional view of Lagrangian transport in line with theoretical turbulence frameworks [*Babiano et al.*, 1990; *LaCasce*, 2008]. Understanding 2-D transport of buoyant coastal materials has utilitarian importance as well (*e.g.,* plastic and oil dispersal, or search and rescue operations). Here, we explore the differences in 3-D and 2-D trajectories in the R36m simulation to assess the difference in connectivity, individual trajectories, and relative dispersion. As described in Section 4.2 in the 2-D case, particles are advected only by the horizontal velocities at $z = -2$ m (*i.e.,* the initialization depth of the 3-D case).

4.5.1 Connectivity

Figure 4.6 illustrates both similarities and differences in connectivity for 2-D (black dashed) and 3-D (black solid) calculations. For short-distance connections (Fig. 4.6a,b) there is little to no difference in connectivity. This is an expected outcome as these connections occur on short time-scales ($\sim$ 1 day) when vertical displacements are small and the 2-D and 3-D trajectories are similar. At longer-distance, differences arise in the 2-D and 3-D answers. Again, the magnitude of the the eastward connections (Fig. 4.6d) is relatively small, and the primary focus is on the westward long-distance connections (Fig. 4.6c). Here, the 2-D solution exhibits stronger connectivity that peaks later and for longer distances, than the 3-D answer. A simple interpretation of the difference is that a fraction of the 3-D particles are advected downward and are not as strongly influenced by the mean, surface-intensified westward current near the surface, not as strongly as are the 2-D particles. This results in more delivery of 2-D particles to the west, while 3-D particles (specifically those further from the shoreline, where the current direction is not depth-uniform) can be advected in different directions by currents at depth.

4.5.2 Difference in submesoscale-controlled transport

To quantify how differences in 2-D and 3-D trajectories grow with time, individual particles in the 2-D case are compared with those that correspond to the particles in the 3-D case that are advected below 20 m after 24 hours for particles initialized at least 750 m away from the shoreline (*i.e.*, the particles sampled for the ensemble averages in Fig. 4.11, solid lines). Figure 4.12 shows the particle averaged relative vorticity and divergence for these 2-D particles (Fig. 4.12) as well as the ensemble average of along- and cross-shore separation between individual 3-D and 2-D particles (Fig. 4.12). In this manner, we isolate the difference in horizontal trajectory due to vertical transport, which is shown in Section 4.4.2 to primarily be driven by rapid convergence into submesoscale fronts and filaments on the shelf.

Both the 3-D and 2-D particles are rapidly drawn into fronts and filaments by the ageostrophic secondary circulations as indicated by the early time cyclonic ($\zeta/f > 0$) and convergent ($\delta/f < 0$) signals in both ensemble averages (Fig. 4.12a). However, whereas the 3-D particles lose the cyclonic, convergent signal as they are advected to depth over $\sim$ 24 hours (Fig. 4.12a, thin lines), the cyclonic, convergent signal for 2-D particles grows to a larger magnitude and remains strong for multiple days (Fig. 4.12a, thick lines), indicating that 2-D particles remain converged within front and filament circulations.

The separation in 3-D and 2-D Lagrangian trajectories for particles advected into submesoscale currents is quantified in Fig. 4.12b with an ensemble average of along- and cross-shore separation S_a, S_c between individual 3-D and 2-D trajectories. Here, a separation distance is computed as $\boldsymbol{S}(t) = \boldsymbol{x}_{3D}(t) - \boldsymbol{x}_{2D}(t)$, where $\boldsymbol{x}$ is the particle position at time t. After 3 days, trajectories differ, on average, by approximately 13 and 5 km in the along- and cross-shore directions, respectively. This represents a substantial difference in 3-D and 2-D Lagrangian trajectories in an active nearshore submesoscale regime, with 2-D trajectories more persistently controlled by front and filament circulations compared to their 3-D counterparts.

4.5.3 Relative dispersion

Relative dispersion for an ensemble of particle pairs in both cases gives a more bulk quantification of differences in 2-D and 3-D transport. Each particle in a pair has an absolute displacement defined as $\boldsymbol{A}(t) = \boldsymbol{x}(t) - \boldsymbol{x}_0$. The relative dispersion is calculated for a particle pair with trajectories $\boldsymbol{A}_1$ and $\boldsymbol{A}_2$ initially separated by a distance $\boldsymbol{R}_0$ [*Babiano et al.*, 1990]:

$$\boldsymbol{R}(t, \boldsymbol{R}_0) = \boldsymbol{R}_0 + \boldsymbol{A}_1 - \boldsymbol{A}_2 \ . \tag{4.2}$$

From the relative dispersion, a relative diffusivity can be calculated:

$$\kappa(t) = \frac{1}{2}\frac{d}{dt}\boldsymbol{R}^2(t, \boldsymbol{R}_0) \ . \tag{4.3}$$

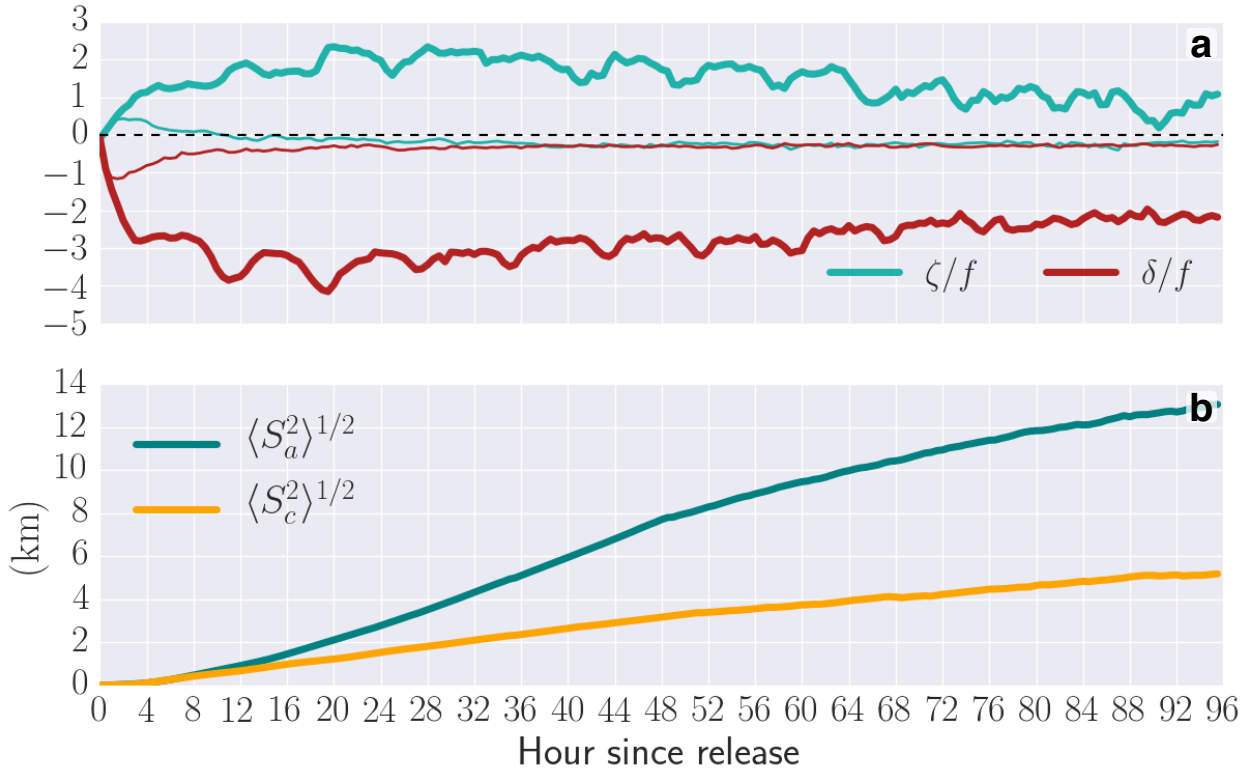

Figure 4.12: Particle averaged (a) relative vorticity (cyan) and divergence (dark red) for the 2-D advected particles in the R36m solution (thick curves). The particle ensemble average in (a) is calculated over the 2-D particles that correspond to the 3-D particles in Fig. 4.11, solid lines: particles that are advected below 20 m in 24 hours after release that are initialized at least 750 m away from the shoreline. For visual reference, the analogous signal for the 3-D particles is plotted in the thin lines. In (b) we illustrate the difference in horizontal trajectory that arises due to vertical transport with along- (teal) and cross-shore (orange) separation (S_a, S_c) between individual 3-D and 2-D particle positions in R36m (plotted as $(S^2)^{1/2}$).

As in 4.3.2, dispersion and diffusivity are rotated in along- and cross-shore directions following *Romero et al.* [2013]. The ensemble of particle pairs in the 3-D and 2-D cases is made separately for particle pairs in each case that have initial separations between 50 m and 450 m, and only for pairs in which both particles remain at least 250 m away from the shoreline for the duration of dispersion calculation (to avoid shoreline influenced dispersion signals). The number of particle pairs for the ensemble over a 5 day period relative to particle release is 197,144 and 162,249 for the 3-D and 2-D cases, respectively. *Romero et al.* [2013] demonstrates that there is a dependency in the dispersive behavior (rate of dispersion and along-shore vs. cross-shore differences) relative to

the distance from the shoreline. We find similar results here, but do not repeat a demonstration. Rather we present the general differences in 2-D vs. 3-D dispersion and relate these differences back to a physical mechanism.

As expected, and in agreement with *Romero et al.* [2013], along-shore dispersion is larger than cross-shore (Fig 4.13a,b). The dispersion and diffusivity curves for both 3-D and 2-D fall between regimes indicative of "diffusion" ($R^2 \sim t^2, \kappa \sim t$) [*Batchelor*, 1950] and "flights" ($R^2 \sim t^3, \kappa \sim t^2$) [*Solomon et al.*, 1993]. "Lévy flights" are random walks where each step is derived from a heavy-tailed distribution of random increments resulting in trajectories that can exhibit long excursions not characteristic of a "diffusive" random walk (where each step is derived from a Gaussian distribution).

At early time, the dispersion is more diffusive (*i.e.,* ballistic) ($R^2 \sim t^2$), influenced by the initial velocity memory. However, at later time, and especially in the 3-D case, dispersion scales towards t^3, indicative of longer flights of particle groups (*e.g.,* Fig. 4.8). The main result here is that 3-D dispersion is stronger (and more closely tends to t^3 at later time) than the 2-D dispersion with vertical transport leading to stronger along- and cross-shore lateral stirring.

The result that dispersion in 3-D is stronger than 2-D is somewhat counter-intuitive to the idea that dispersion is larger with the stronger current speeds at the surface than at depth. *Poje et al.* [2010] show that for purely 2-D surface trajectories, pair separation is enhanced with an increase in (and scales well with) the Okubo-Weiss parameter ($Q = S^2 - \zeta^2$, where S the lateral strain rate, defined in Chapter 2). The magnitude of Q will generally increase with a more active submesoscale regime, but a purely 2-D metric is less relevant. Here we relate the 3-D dispersion behavior displayed in Fig. 4.13 to the local circulations associated with submesoscale fronts and filaments.

A fraction of the dispersion on short time-scales is directly controlled by the secondary circulation of submesoscale fronts and filaments that converges in and elongates particle distributions

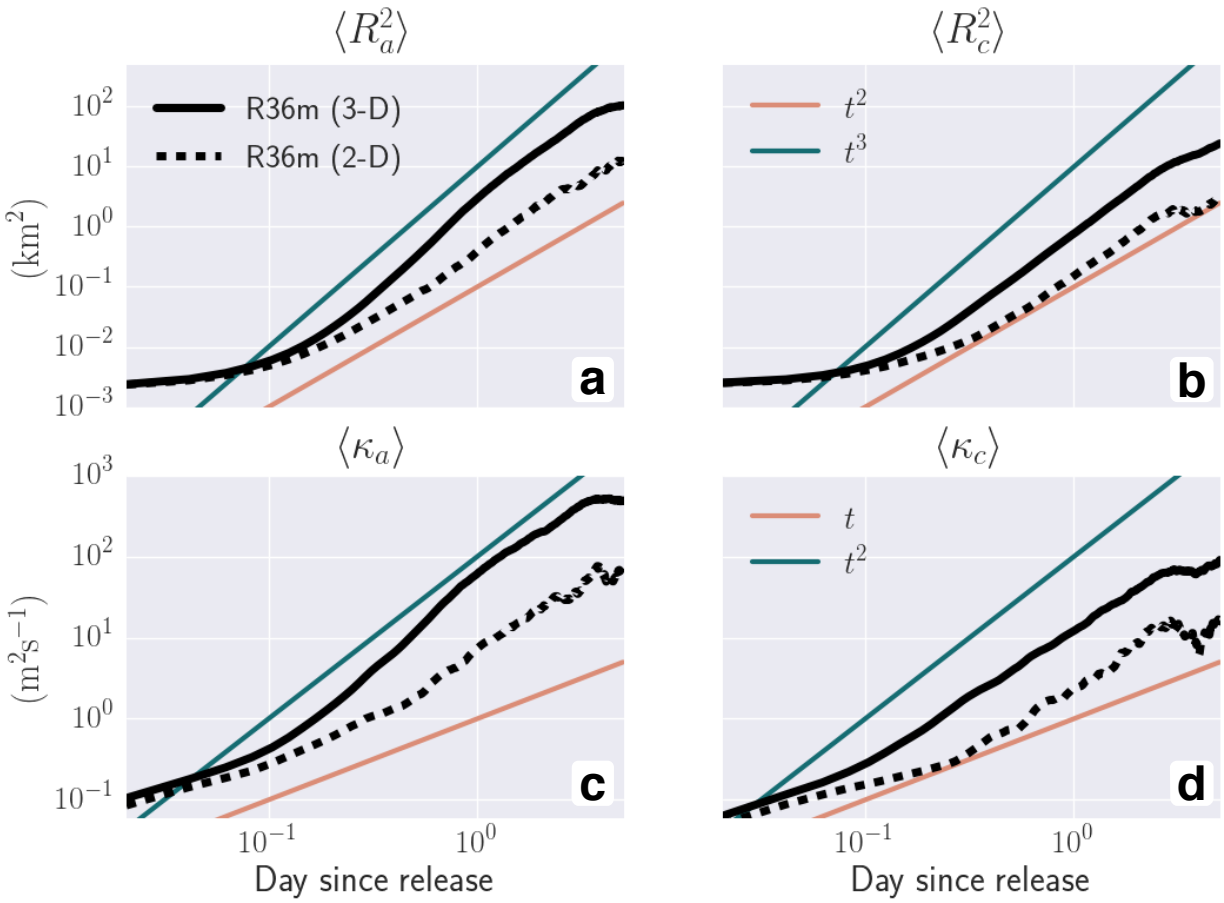

Figure 4.13: Relative dispersion (a,b) and diffusivity (c,d) in the (a) along- and (b) cross-shore directions for particle pairs advected by 3-D (solid) and 2-D (dashed) velocities in R36m. The dispersion and diffusivity is plotted as an ensemble average ($\langle R^2_{i=a,c} \rangle$) over all possible particle pairs that have an initial horizontal separation between 50 m and 450 m. A particle pair is only used in the ensemble if both particles remain (laterally) 250 m away from the shoreline for the duration of the dispersion calculation (5 days). Power law scalings for "diffusion" ($R^2 \sim t^2$, $\kappa \sim t$; pink) and "flights" ($R^2 \sim t^3$, $\kappa \sim t^2$; teal) are indicated for comparison.

along a surface maximum in horizontal density gradient. This convergence and elongation is illustrated in the early time for the 3-D trajectories given in Fig. 4.10. While the 2-D trajectories are maintained within the fronts and filaments near the surface for multiple days (Fig. 4.12, thick curves), the 3-D trajectories are immediately downwelled by the ageostrophic secondary circulation (Fig. 4.11c). Once downwelled, particle pairs initially drawn into a front or filament can be

dispersed by currents at depth. The increased dispersion in 3-D vs. 2-D particle pairs in Fig. 4.13 indicates that this dispersion at depth is larger and grows faster than dispersion driven by purely near-surface currents, where a population of submesoscale fronts and filaments are continuously trapping particle pairs and holding them for multiple days.

4.6 Discussion and Conclusions

In this study we present new conceptions for material transport in the nearshore and illustrate that there is a resolution sensitivity to simulated Lagrangian trajectories along the coast with a hierarchy of realistic ROMS simulation of the SBC. At higher resolution ($\Delta x \lessapprox 100$ m, R36m and R100m in this study), previously unresolved classes of coastal variability (submesoscale fronts and filaments, topographic wakes, and narrow along-shore jets) open up transport pathways on the shelf that allow for rapid along-shore and vertical material fluxes. In general, a coarser-resolution simulation ($\Delta x \approx 1$ km) will underestimate along- and cross-shore fluxes in and out of nearshore regions. A symptom of this underestimation is a retentive bias in (short-distance) along-shore connectivity. Analogous metrics (not shown) indicate that coarser-resolution simulations will similarly underestimate cross-shore displacements. This underestimation results in little to no horizontal displacement in waters inshore of approximately 1 km and an under-representation of downwelling of near-surface material due to an absence of fine-scale currents (*e.g.,* shelf fronts and filaments).

While some past studies have investigated statistical descriptions of coastal dispersion [*Romero et al.*, 2013], here we have focused on transport mechanism, with illustration and statistical confirmation of control by submesoscale dynamics to paint a lifecycle picture for transport of near-surface material along the coast. Material can be rapidly transported in narrow along-shore jets, exhibiting trajectories commensurate with sustained "flights" [*Solomon et al.*, 1993; *Brown and Smith*, 1991] (*e.g.,* Fig. 4.8) . The fast downwelling of near-surface material, exhibited in the

higher-resolution simulations, is primarily due to the secondary circulations of submesoscale fronts and filaments populating the shelf; these rapidly evolving, turbulently manifested, currents will laterally trap and subsequently downwell material on the shelf on the time-scale of hours. Coastal 3-D dispersion is larger than 2-D dispersion, due to a difference in submesoscale control on particle pairs; 2-D surface particles will remain trapped within fronts and filaments for days while analogous 3-D particles will be rapidly downwelled by the same fronts and filaments and dispersed at depth within hours.

Our results caution biophysical studies that attempt to simulate large-scale connectivity of biological material (sourced in the nearshore) utilizing circulation models with $\Delta x \gtrapprox 1$ km, previously perceived as 'high-resolution' [*Wood et al.*, 2014; *Cowen et al.*, 2006]. In these studies a random walk or isotropic turbulent diffusivity is added to particle trajectories in attempt to capture subgrid scale motions [*Paris et al.*, 2013]. However, this isotropic implementation is likely not apt for nearshore submesoscale features that exhibit anisotropic orientation relative to bathymetry [*Dauhajre et al.*, 2017; *Romero et al.*, 2013].

Analogously, the lack of nearshore variability in a coarser-resolution simulation presents a computational hurdle for future biophysical modeling studies. Often, answers to ecological questions necessitate data on seasonal or yearly time-scales which limits resolution due to computational feasibility. In these investigations some form of (3-D) stochastic variability will need to be formulated and added to these models; this variability should reflect the anisotropy of shelf currents. Starting points for this parameterized variability include 2-D parameterized submesoscale Lagrangian transport [*Haza et al.*, 2012] and implementation of along- and cross-shore diffusivities derived from short-time, higher-resolution simulations as in *Romero et al.* [2013].

In the high-resolution simulations, the fast time-scales (O(hours-days)) of connectivity variability (Fig. 4.6), the large horizontal and vertical displacements of particles inshore of 1 km (Fig. 4.7), and the fine-scale transport mechanisms responsible for material delivery to along-shore sites (*e.g.,* Fig. 4.8) offer an additional conception of transport on the shelf. The "coastal bound-

ary layer" of *Nickols et al.* [2012] and "sticky water" of *Wolanski and Spangol* [2000] and [*Restrepo et al.*, 2014] analogously hypothesize weak currents and consequently, small material displacement in regions inshore of $\approx$ 1 km. These views can stem from time- and depth-averaged observations [*Nickols et al.*, 2012] and 2-D modeling [*Wolanski and Spangol*, 2000] that may be diluting or not capturing the high variability of 3-D flow structures that inhabit the shelf. However, "sticky" water can also be due to surface wave and tidal dynamics in very shallow water O(10 m) from shore [*Restrepo et al.*, 2014] that can not be examined in our simulations that have no waves and give an artificial signal of local retention bias within Δx of the shoreline (Section 4.3.2).

Absent in all of our simulations are surface gravity waves and their effects on the Eulerian velocity fields [*Uchiyama et al.*, 2010]. These effects can be categorized into shelf and surf zone effects. In the surf zone (waters extending from the shoreline to $\approx$ 200-300 m across-shore), cross-shore transport can be induced by 3-D transient rip currents [*Kumar and Feddersen*, 2017], which is not represented in our simulations. Such eddying circulations will be responsible for a large fraction of horizontal diffusivity in the surf zone and ultimately control exchanges with inner-shelf waters. In this study we have restricted our primary mechanistic interpretations to areas at least 200 - 300 m offshore; that is, the effects of nearshore submesoscale currents investigated here generally exist offshore of a potential surf zone.

On the shelf (*i.e.,* outside the surf zone), the effects of surface gravity waves on currents is an active area of research with many open questions, specifically on submesoscale front and filament circulations. Wave-effects on front and filament circulations are dependent on the strength of boundary layer turbulence and swell direction, making for complicated functional dependencies in (even) idealized settings [*McWilliams*, 2018]. Present studies are beginning to simulate shelf currents in an active wave field that interacts with a three-dimensional surf zone. These investigations will close the gap between the surf zone and shelf, shed light on wave effects on currents, and resolve the degree of nearshore "stickiness" in future realistic simulations.

CHAPTER 5

Summary and Prospects

This work introduces submesoscale dynamics to the coastal oceanographic community. Similarly, it is an addition to the growing literature on submesoscale currents, historically investigated in the open-ocean. Realistic, coastal ocean simulations with resolutions of $\Delta x \lessapprox 100$ m paint a new picture of continental shelf dynamics where spontaneously formed, short-lived submesoscale fronts, filaments, and vortices populate the nearshore region and coexist with tidal flows, internal waves, and wind-driven and buoyant coastal currents.

5.1 Summary

A characterization of the coastal submesoscale regime (Chapter 2) illustrates ubiquity and evidences bathymetric control on generation and spatial orientation of nearshore submesoscale currents: vorticity generation at headlands con dominate submesoscale activity in a bay, and shelf fronts and filaments will preferentially align parallel to isobaths. Local analysis of isolated fronts and filaments shows that submesoscale circulations on the shelf share similarities with their open-ocean analogs: Ro $>>$ 1, surface convergence, downwelling, and cyclonic shear with the low-frequency circulation dynamically described by a TTW momentum balance. Shallow-water front and filament secondary circulations drive a restratifying heat flux that can compete with the opposite signed heat flux of a breaking internal wave.

A diurnal oscillation of front and filament circulations, previously unknown to exist, can be substantial, with a ≈ 50 % change in circulation strength (Chapter 3). The underlying physics controlling this change are quite simple in the form of 1-D Ekman layer dynamics that are not captured by a TTW diagnostic. This dynamical interpretation of the diurnal phasing is applicable to both the open-ocean and shelf. The 1-D, non-dimensonal model given in Chapter 3 allows mechanistic interpretation of the controlling dynamics and accurately predicts the diurnal phasing of front and filament circulations in realistic, primitive equation simulations (*e.g.,* in the Gulf of Mexico as in [*Bracco et al.*, 2019]) given a latitude, daily-averaged boundary layer depth, and bulk change in vertical diffusivity.

Chapter 4 demonstrates that submesoscale currents on the shelf can control the fate and transport of material. Failure to sample these currents results in predictions of stronger material retention and an under-representation of vertical transport. Lagrangian trajectories exhibit rapid along-shore transport and downwelling in regions ≈ 0.3 - 1 km offshore that is not predicted by previous nearshore dynamical conceptions, *e.g.,* the 'coastal boundary layer' [*Nickols et al.*, 2012]. Downwelling of surface material in the nearshore is primarily driven by the ageostrophic secondary circulation of shelf fronts and filaments. This downwelling can ultimately influence the fate of surface material via dispersion of larger-scale flows at depth. It is clear from this work that submesoscale variability needs to be included (parameterized or resolved) in any attempts to simulate or measure coastal transport.

5.2 Prospects for Future Study

The results and interpretations in this dissertation stem exclusively from numerical models, mostly regional simulations of Southern California. There are certain to be differences in the manifestation of submesoscale variability on the shelf in other regions with different topography and atmospheric forcing, *e.g.,* the heavily studied, gently sloped, colder Martha's Vineyard

shelf [*Ganju et al.*, 2011]. Future simulations can demonstrate the degree of regional variability of coastal submesoscale currents. Similarly, the development of new coastal observational networks should aim to sample submesoscale variability in the nearshore. Though, given the complex 3-D structure and short life-cycles of submesoscale currents, this development will likely require new measurement technologies and strategies: *e.g.,* large ensembles of small, Lagrangian, autonomous instruments equipped with an array of sensors that can be perpetually trapped in and out of fronts and filaments by maintaining themselves within the surface boundary layer. It is impossible to sample all types of coastal variability with a single instrument or even network; however, it is clear from this work that submesoscale fronts and filaments are relevant enough in the nearshore to motivate observational developments.

This work focuses on physical variability, however, there are sure to be imprints or interactions of physical submesoscale variability on coastal biogeochemistry and ecology; this remains an open question ripe for future study. How much does the rapid along-shore transport and vertical fluxes induced by submesoscale currents on the shelf control ecosystem functioning through larval or nutrient delivery? Similarly, how does the manifestation of turbulent nearshore currents change with biologically-sourced, physical drag, *e.g.,* nearshore O(100 m) patches of giant kelp that densely populate the Santa Barbara Channel [*Cavanaugh et al.*, 2014].

These questions aim to build our predictive skill of coastal ecosystems by resolving as much of reality as possible. However, present computational storage limitations hinder our ability simulate the full-spectrum of reality for time periods greater than O(months). This limitation calls for the development of a nearshore parameterization of submesoscale fluxes (which induce fast material transport in the nearshore, Chapter 4) that takes into account the anisotropy and 3-D characteristics of these currents.

Dynamically, a more comprehensive analysis of nearshore heat budgets can fully reveal how stratification is set on the shelf: submesoscale advective restratification versus the stratification induced by breaking internal waves. Similarly, the reliability of KPP in modulating the manifesta-

tion of submesoscale currents in a turbulent boundary layer is not fully known and will benefit from more comparisons with LES as in [*Sullivan and McWilliams*, 2017]. The most interesting future work, however, is likely concerned with the inclusion of additional shelf dynamics not included in the present simulations: non-hydrostatic effects and surface gravity waves. Realistic, non-hydrostatic simulations at $\Delta x \approx \mathcal{O}(100\text{ m})$ is a frontier in realistic oceanic modeling that aims to close a dynamical gap with Large Eddy Simulations. Recent algorithmic developments [*Guillaume et al.*, 2017] give us the opportunity to simulate a non-hydrostatic, realistic coastal ocean with improved representation of processes such as internal wave breaking and convection, though, the expectation for the full range of dynamical outcomes remains uncertain. Additionally, as mentioned in Chapter 4, inclusion of surface waves in future simulations [*Uchiyama et al.*, 2010] will provide a novel set of realistic realizations to explore wave effects on currents, three-dimensional surf-zone dynamics, exchanges between the surf-zone and shelf, and perhaps, dynamical interactions not presently expected.

References

Austin, J., and S. Lentz (2002), The inner shelf response to wind-driven upwelling and downwelling, *J. Phys. Oceanogr.*, *32*, 2171–2193, doi:10.1175/1520-0485(2002)032,2171:TISRTW.2.0.CO;2.

Babiano, A., C. Basedevant, P. Roy, and R. Sadourny (1990), Relative Dispersion in Two-Dimensional Turbulence, *J. Fluid Mech.*, *214*, 535–557, doi:10.1017/S0022112090000258.

Barkan, R., K. Winters, and S. L. Smith (2015), Energy cascades and loss of balance in a reentrant channel forced by wind stress and buoyancy fluxes, *J. Phys. Oceanogr.*, *45*, 272–293, doi:10.1175/JPO-D-14-0068.1.

Bassin, C., and L. Washburn (2005), Sub-mesoscale coastal eddies observed by high frequency radar: A new mechanism for delivering nutrients to kelp forests in the Southern California Bight, *Geophys. Res. Lett.*, *32*, 1–4, doi:10.1029/2005GL023017.

Batchelor, G. (1950), The application of the similarity theory of turbulence to atmospheric diffusion, *Quart. J. Roy. Meteor. Soc*, *76*, 133–146.

Benthuysen, J., L. Thomas, and S. Lentz (2015), Rapid Generation of Upwelling at a Shelf Break Cause By Buoyancy Shutdown, *J. Phys. Oceanogr.*, *45*, 294 – 312, doi:10.1175/JPO-D-14-0104.1.

Berti, S., F. D. Santos, G. Lacorata, and A. Vulpiani (2011), Lagrangian Drifter Dispersion in the Southwestern Atlantic Ocean, *J. Phys. Oceanogr.*, *41*, 1659–1672, doi:10.1175/2011JPO4541.1.

Boccaletti, G., R. Ferrari, and B. Fox-Kemper (2006), Mixed layer instabilities and restratification, *J. Phys. Oceanogr.*, *37*, 2228–2250, doi:10.1175/JPO3101.1.

Boehm, A., B. Sanders, and C. Winant (2002), Cross-Shelf Transport at Huntington Beach Implications for the Fate of Sewage Discharged through an Offshore Ocean Outfall, *Environ. Sci. Technol.*, *36*, 1899–1906, doi:10.1021/es0111986.

Bracco, A., J. Choi, K. Joshi, H. Luo, and J. McWilliams (2016), Submesoscale currents in the northern Gulf of Mexico: Deep phenomena and dispersion over the continental slope, *Ocean Modelling*, *101*, 43–58, doi:10.1016/j.ocemod.2016.03.002.

Bracco, A., D. Sun, R. Barkan, J. Choi, G. Liu, D. Dauhajre, M. Berta, M. Molemaker, J. McWilliams, and A. Griffa (2019), Diurnal Cycling of Submesoscale Dynamics: Lagrangian Implications in Model Simulations of the Northern Gulf of Mexico, *J. Phys. Oceanogr.*, *submitted*.

Brown, M., and K. Smith (1991), Ocean stirring and chaotic low-order dynamics, *Physics of Fluids A: Fluid Dynamics*, *3*, 1186–1192, doi:10.1063/1.858047.

Buijsman, M., Y. Uchiyama, J. McWilliams, and C. Hill-Lindsay (2012), Modeling semidiurnal internal tide variability in the Southern California Bight, *J. Phys. Oceanogr.*, *42*, 62–77, doi:10.1175/2011JPO4597.1.

Callies, J., R. Ferrari, J. M. Klymax, and J. Gula (2015), Seasonality in submesoscale turbulence, *Nature Communications*, *6*, 6862–6870, doi:10.1038/ncomms7862.

Callies, J., G. Flierl, R. Ferrari, and B. Fox-Kemper (2016), The role of mixed-layer instabilities in submesoscale turbulence, *J. Fluid Mech.*, *788*, 5–41, doi:10.1017/jfm.2015.700.

Capet, X., J. McWilliams, M. Molemaker, and A. Shchepetkin (2008a), Mesoscale to submesoscale transition in the California Current System. Part III: Energy balance and flux, *J. Phys. Oceanogr.*, *38*, 2256–2269, doi:10.1175/2008JPO3810.1.

Capet, X., J. McWilliams, M. Molemaker, and A. Shchepetkin (2008b), Mesoscale to submesoscale transition in the California Current System. Part II: Frontal processes, *J. Phys. Oceanogr.*, *38*, 44–64, doi:10.1175/2007JPO3672.1.

Capet, X., E. Campos, and A. Paiva (2008c), Submesoscale activity over the Argentinian shelf, *Geophys. Res. Lett.*, *35*, 1–5, doi:10.1029/2008GL034736.

Capet, X., J. McWilliams, M. Molemaker, and A. Shchepetkin (2008d), Mesoscale to submesoscale transition in the California Current System. Part I: Flow structure, eddy flux, and observational tests, *J. Phys. Oceanogr.*, *38*, 29–43, doi:10.1175/2007JPO3671.1.

Castorani, M. C., D. Reed, F. Alberto, T. Bell, R. Simons, K. Cavanaugh, D. Siegel, and P. Raimondi (2015), Connectivity structures local population dynamics: A long-term empirical test in a large metapopulation system, *Ecology*, *96*, 3141–3152, doi:10.1890/15-0283.1.

Castorani, M. C., D. Reed, P. Raimondi, F. Alberto, T. Bell, K. Cavanaugh, D. Siegel, and R. Simons (2017), Fluctuations in population fecundity drive variation in demographic connectivity and metapopulation dynamics, *Proc. R. Soc. B.*, *284*, 2016–2086, doi:10.1098/rspb.2016.2086.

Cavanaugh, K., D. Siegel, P. Raimondi, and F. Alberto (2014), Patch definition in metapopulation analysis: a graph theory approach to solve the mega-patch problem, *Ecology*, *95*, 316–328.

Chapman, D. (1986), A simple model of the formation and maintenance of the shelf/slope front in the Middle Atlantic Bight, *J. Phys. Oceanogr.*, *16*, 1273–1279, doi:10.1175/1520-0485(1994)024<1464:TOACDF>2.0.CO;2.

Chapman, D. (1987), Application of wind-forced, long, coastal-trapped wave theory along the California coast, *J. Geophys. Res.*, *92*, 1798–1816, doi:10.1029/JC092iC02p01798.

Chapman, D. (2000), Boundary layer control of buoyant coastal currents and the establishment of a shelfbreak front, *J. Phys. Oceanogr.*, *30*, 2941–2955, doi:10.1175/1520-0485(2001)031<2941:BLCOBC>2.0.CO;2.

Chapman, D., and R. Beardsley (1989), On the origin of shelf water in the Middle Atlantic Bight, *J. Phys. Oceanogr.*, *19*, 384–291, doi:10.1175/1520-0485(1989)019<0384:OTOOSW>2.0.CO;2.

Chapman, D., and S. Lentz (1994), Trapping of a coastal density front by the bottom boundary layer, *J. Phys. Oceanogr.*, *24*, 1464–1479, doi:10.1175/1520-0485(1994)024<1464:TOACDF>2.0.CO;2.

Chapman, D., and S. Lentz (2005), Acceleration of a stratified current over a sloping bottom, driven by an alongshelf pressure gradient, *J. Phys. Oceanogr.*, *35*, 1305–1317, doi:10.1175/JPO2744.1.

Chen, C., and R. Beardsley (1995), A Numerical Study of Stratified Tidal Rectification over Finite-Amplitude Banks. Part I: Symmetric Banks, *J. Phys. Oceanogr.*, *25*, 2090–2110, doi:10.1175/1520-0485(1995)025<2090:ANSOST>2.0.CO;2.

Chen, C., R. Beardsley, P. Franks, and J. Keuren (2003), Influence of diurnal heating on stratification and residual circulation of Georges Bank, *J. Geophys. Res.*, *108*, 1–21, doi:10.1029/2001JC001245.

Chen, K., and R. He (2009), Numerical Investigation of the Middle Atlantic Bight Shelfbreak Frontal Circulation Using a High-Resolution Ocean Hindcast Model, *J. Phys. Oceanogr.*, *40*, 949–964, doi:10.1175/2009JPO4262.1.

Cowen, R., C. Paris, and A. Srinivasan (2006), Scaling of Connectivity in Marine Populations, *Science*, *311*, 522–527, doi:10.1126/science.1122039.

Cudaback, C., and L. Washburn (2005), Subtidal inner-shelf circulation near Point Conception, California, *J. Geophys. Res.*, *110*, doi:10.1029/2004JC002608.

Dale, A., D. Ullman, J. Barth, and D. Hebert (2003), The front on the Northern Flank of Georges Bank in spring: 1. Tidal and subtidal variability, *J. Geophys. Res.*, *108*, 1–18, doi:10.1029/2002JC001327.

D'Asaro, E., C. Lee, L. Rainville, R. Harcourt, and L. Thomas (2011), Enhanced turbulence and energy dissipation at ocean fronts, *Science*, *332*, 318–322, doi:10.1126/science.1201515.

Dauhajre, D., and J. McWilliams (2018), Diurnal evolution of submesoscale front and filament circulations, *J. Phys. Oceanogr.*, *48*, 2343–2361, doi:10.1175/JPO-D-18-0143.1.

Dauhajre, D., and J. McWilliams (2019), Nearshore Lagrangian Connectivity, *J. Geophys. Res: Oceans*, *submitted*.

Dauhajre, D., J. McWilliams, and Y. Uchiyama (2017), Submesoscale Coherent Structures on the Continental Shelf, *J. Phys. Oceanogr.*, *47*, 2949 – 2976, doi:10.1175/JPO-D-16-0270.1.

Dever, E. (1996), Wind-forced cross-shelf circulation on the Northern California Shelf, *J. Phys. Oceanogr.*, *27*, 1566–1580, doi:10.1175/1520-0485(1997)027<1566:WFCSCO>2.0.CO;2.

DiGiacomo, P., and B. Holt (2001), Satellite observations of small coastal ocean eddies in the Southern California Bight, *J. Geophys. Res.*, *106*, 22,521–22,543, doi:10.1029/2000JC000728.

Dong, C., J. McWilliams, and A. Shchepetkin (2007), Island Wakes in Deep Water, *J. Phys. Oceanogr.*, *37*, 962–981, doi:10.1175/JPO3047.1.

Durski, S., S. Glenn, and D. Haidvogel (2004), Vertical mixing schemes in the coastal ocean: Comparison of the level 2.5 Mellor-Yamada scheme with an enhanced version of the k profile parameterization, *Geophys. Res. Lett.*, *109*, 1–23, doi:10.1029/2002JC001702.

Egbert, G., A. Bennet, and M. Foreman (1994), TOPEX/Poseidon tides estimated using a global inverse model, *J. Geophys. Res.*, *99*, 24,821–24,852, doi:10.1029/94JC01894.

Feddersen, F. (2014), The Generation of Surfzone Eddies in a Strong Alongshore Current, *J. Phys. Oceanogr.*, *44*, 600–617, doi:10.1175/JPO-D-13-051.1.

Feddersen, F., R. Guza, S. Elgar, and T. Herbers (1998), Alongshore momentum balances in the nearshore, *J. Geophys. Res.*, *103*, 15,667–15,676, doi:10.1029/98JC01270.

Federiuk, J., and J. Allen (1996), Model studies of near-inertial waves in flow over the Oregon continental shelf, *J. Phys. Oceanogr.*, *26*, 2053–2075, doi:10.1175/1520-0485(1996)026,2053:MSONIW.2.0.CO;2.

Fujimura, A., A. Reniers, C. Paris, A. Shanks, J. MacMahan, and S. Morgan (2017), Numerical simulations of onshore transport of larvae and detritus to a steep pocket beach, *Marine Ecology Progress Series*, *582*, 33–43, doi:10.3354/meps12331.

Furukawa, K., and E. Wolanski (1998), Shallow-water frictional effects in island wakes, *Estuariane, Coastal and Shelf Science*, *46*, 599–608, doi:10.1006/ecss.1997.0301.

Ganju, N., S. Lentz, A. Kirincich, and J. Farrar (2011), Complex mean circulation over the inner shelf south of Martha's Vineyard revealed by observations and a high-resolution model, *J. Geophys. Res.*, *116*, doi:10.1029/2011JC007035.

Garrett, C., and J. Loder (1981), Dynamical aspects of shallow sea fronts, *Phil. Trans. R. Soc. Lond.*, *302*, 563–581, doi:10.1098/rsta.1981.0183.

Gaylord, B., and S. Gaines (2000), Temperature or transport? Range limits in marine species mediated solely by flow, *The American Naturalist*, *155*, 769–789, doi:10.1086/303357.

Geyer, W., and R. Signell (1990), Measurements of tidal flow around a headland with a shipboard acoustic doppler current profiler, *J. Geophys. Res.*, *95*, 3189–3197, doi:10.1029/JC095iC03p03189.

Guillaume, R., M. Molemaker, D. Nicolas, and D. Thomas (2017), Compact symmetric Poisson equation discretization for non-hydrostatic sigma coordinates ocean model, *Ocean Modelling*, *118*, 107–117, doi:10.1016/j.ocemod.2017.09.001.

Gula, J., M. Molemaker, and J. McWilliams (2014), Submesoscale cold filaments in the Gulf Stream, *J. Phys. Oceanogr.*, *44*, 2617–2643, doi:10.1175/JPO-D-14-0029.1.

Haller, G. (2015), Lagrangian Coherent Structures, *Annu. Rev. Fluid Mech.*, *47*, 137–162, doi:10.1146/annurev-fluid-010313-141322.

Hally-Rosendahl, K., and F. Feddersen (2016), Modeling surfzone to inner-shelf tracer exchange, *J. Geophys. Res.*, *121*, 4007–4025, doi:doi.org/10.1002/2015JC011530.

Haza, A., T. Ozgokmen, A. Griffa, Z. Garraffo, and L. Piterbarg (2012), Parameterization of particle transport at submesoscales in the Gulf Stream region using lagrangian subgridscale models, *Ocean Modelling*, *42*, 31–49, doi:10.1016/j.ocemod.2011.11.005.

Hickey, B., E. Dobbins, and S. Allen (2003), Local and remote forcing of currents and temperature in the central Southern California Bight, *J. Geophys. Res.*, *108*, 1–26, doi:10.1029/2000JC000313.

Hill, A., I. James, P. Linden, J. Matthews, D. Prandle, J. Simpson, E. Gmitrowicz, D. Smeed, K. Lwiza, R. Durazo, A. Fox, and D. Bowers (1993), Dynamics of tidal mixing fronts in the North Sea, *Phil. Trans. R. Soc. Lond.*, *343*, 431–446, doi:10.1098/rsta.1993.0057.

Hoskins, B. (1982), The mathematical theory of frontogenesis, *Ann. Rev. Fluid Mech.*, *14*, 131–151, doi:10.1146/annurev.fl.14.010182.001023.

Jackson, G., and R. Strathmann (1981), Larval mortality from offshore mixing as a link between precompetent and competent periods of development, *The American Natrualist*, *118*, 16–26.

Kim, S., B. Cornuelle, E. Terrill, B. Jones, L. Washburn, M. Moline, J. Paduan, N. Garfield, J. Largier, G. Crawford, and P. Kosro (2013), Poleward propagating subinertial alongshore surface currents off the U.S. West Coast, *J. Geophys. Res.*, *118*, 6791–6806, doi:10.1002/jgrc.20400.

Kirincich, A. (2016), The occurrence, drivers, and implications of submesoscale eddies on Martha's Vineyard inner shelf, *J. Phys. Oceanogr.*, *46*, 2645–2662, doi:10.1175/JPO-D-15-0191.1.

Kirincich, A., S. Lentz, and J. Barth (2009), Wave-driven inner-shelf motions on the Oregon coast, *J. Phys. Oceanogr.*, *39*, 2942–2956, doi:10.1175/2009JPO4041.1.

Kumar, N., and F. Feddersen (2017), A new offshore transport mechanism for shoreline-released tracer induced by transient rip currents and stratification, *Geophys. Res. Lett.*, *44*, 2843–2851, doi:10.1002/2017GL072611.

Kumar, N., F. Fedddersen, Y. Uchiyama, J. McWilliams, and W. O'Reilly (2015), Midshelf to surfzone coupled roms-swan model data comparison of waves, currents, and temperature: Diagnosis of subtidal forcings and response, *J. Phys. Oceanogr.*, *45*, 1464–1490, doi:10.1175/JPO-D-14-0151.1.

Kumar, N., F. Fedddersen, S. Suanda, Y. Uchiyama, and J. McWilliams (2016), Mid- to inner-shelf coupled roms-swan model data comparison of currents and temperature: Diurnal and semidiurnal variability, *J. Phys. Oceanogr.*, *46*, 841–862, doi:10.1175/JPO-D-15-0103.1.

LaCasce, J. (2008), Statistics from lagrangian observations, *Progress in Oceanography*, *77*, 1–29, doi:10.1016/j.pocean.2008.02.002.

Large, W., J. McWilliams, and S. Doney (1994), Oceanic vertical mixing: A review and a model with a nonlocal boundary layer parameterization., *Rev. Geophys.*, *32*, 363–403, doi:10.1029/94RG01872.

Lemarie, F., J. Kurian, A. Shchepetkin, M. Molemaker, F. Colas, and J. McWilliams (2012), Are there inescapable issues prohibiting the use of terrain-following coordinates in climate models?, *Ocean Modelling*, *42*, 57–79, doi:10.1016/j.ocemod.2011.11.007.

Lentz, S., and D. Chapman (2004), The importance of nonlinear cross-shelf momentum flux during wind-driven coastal upwelling, *J. Phys. Oceanogr.*, *34*, 2444–2457.

Lentz, S., and M. Fewings (2012), The wind- and wave-driven inner-shelf circulation, *Annu. Rev. Mar. Sci.*, *4*, 317–343, doi:10.1146/annurev-marine-120709-142745.

Lentz, S., and C. Winant (1986), Subinertial currents on the Southern California Shelf, *J. Phys. Oceanogr.*, *16*, 1737–1750, doi:10.1175/1520-0485(1986)016,1737:SCOTSC.2.0.CO;2.

Lerczak, J., M. Hendershott, and C. Winant (2001), Observations and modeling of coastal internal waves driven by a diurnal sea breeze, *J. Geophys. Res.*, *106*, 19,715–19,729, doi:10.1175/JPO2644.1.

Lerczak, J., C. Winant, and M. Hendershott (2003), Observations of the semidiurnal internal tide on the Southern California slope and shelf, *J. Geophys. Res.*, *108*, 1–13, doi:10.1029/2001JC001128.

Levy, M., R. Ferrari, P. Franks, A. Martin, and P. Riviere (2012), Bringing physics to life at the submesoscale, *Geophys. Res. Lett.*, *39*, 1–13, doi:10.1029/2012GL052756.

Linder, C., and G. Gawarkiewicz (1998), A climatology of the shelfbreak front in the Middle Atlantic Bight, *J. Geophys. Res.*, *103*, 18,405–18,423, doi:10.1029/98JC01438.

Loder, J., K. Drinkwater, N. Oakey, and E. Horne (1993), Circulation, hydrographic structure and mixing at tidal fronts: The view from Georges Bank, *Phil. Trans. R. Soc. Lond.*, *343*, 447–460, doi:10.1038/ncomms7862.

Lumpkin, R., and S. Elipot (2010), Surface drifter pair spreading in the North Atlantic, *J. Geophys. Res.*, *115*, 1–20, doi:10.1029/2010JC006338.

Maddock, L., and R. Pingree (1978), Numerical simulation of the Portland tidal eddies, *Estuarine and Coastal Marine Science*, *6*, 353–363, doi:10.1016/0302-3524(78)90127-5.

Mahadevan, A. (2016), The impact of submesoscale physics on primary productivity of plankton, *Annu. Rev. Mar. Sci.*, *8*, 161–184, doi:10.1016/j.ocemod.2006.05.005.

Mahadevan, A., and A. Tandon (2006a), An analysis of mechanisms for submesoscale vertical motion at ocean fronts, *Ocean Modelling*, *14*, 241–256, doi:10.1016/j.ocemod.2006.05.006.

Mahadevan, A., and A. Tandon (2006b), Modeling vertical motion at ocean fronts: Are nonhydrostatic effects relevant at submesoscales?, *Ocean Modelling*, *14*, 222–240, doi:10.1016/j.ocemod.2006.05.005.

Mason, E., J. Molemaker, A. Shchepetkin, F. Colas, J. McWilliams, and P. Sangra (2010), Procedures for offline grid nesting in regional ocean models, *Ocean Modelling*, *35*, 1–15, doi:10.1016/j.ocemod.2010.05.007.

Mayorga-Adame, C., H. Batchelder, and Y. Spitz (2017), Modeling Larval Connectivity of Coral Reef Organisms in the Kenya-Tanzania Region, *Front. Mar. Sci.*, *4*, 92, doi:10.3389/fmars.2017.00092.

McWilliams, J. (2016), Submesoscale currents in the ocean, *Proc. Roy. Soc. A*, *472*, 1–32, doi:10.1098/rspa.2016.0117.

McWilliams, J. (2017), Submesoscale surface fronts and filaments: secondary circulation, buoyancy flux, and frontogenesis, *J. Fluid Mech.*, *823*, 391 – 432, doi:10.1017/jfm.2017.294.

McWilliams, J. (2018), Surface wave effects on submesoscale fronts and filaments, *J. Fluid Mech.*, *843*, 479–517, doi:10.1017/jfm.2018.158.

McWilliams, J., F. Colas, and J. Molemaker (2009a), Cold filamentary intensification and oceanic surface convergence lines, *Geophys. Res. Lett.*, *36*, 1–5, doi:10.1029/2009GL039402.

McWilliams, J., M. Molemaker, and E. Olafsdottir (2009b), Linear Fluctuation Growth during Frontogenesis, *J. Phys. Oceanogr.*, *39*, 3111 – 3129, doi:10.1175/2009JPO4186.1.

McWilliams, J., E. Huckle, and A. Shchepetkin (2009c), Buoyancy Effects in a Stratified Ekman Layer, *J. Phys. Oceanogr.*, *39*, 2581 – 2599, doi:10.1175/2009JPO4130.1.

McWilliams, J., J. Gula, J. Molemaker, L. Renault, and A. Shchepetkin (2015), Filament frontogenesis by boundary layer turbulence, *J. Phys. Oceanogr.*, *45*, 1988–2005, doi:10.1175/JPO-D-14-0211.1.

Michalakes, J., J. Dudhia, D. Gill, J. Klemp, and W. Skamarock (1998), Design of a next-generation regional weather research and forecast model, *Proceedings of the Eighth Workshop on the Use of Parallel Processors in Meteorology. European Center for Medium Range Weather Forecasting, Reading, United Kingdom*, pp. 117–124.

Mitari, S., D. Siegel, J. Watson, C. Dong, and J. McWilliams (2009), Quantifying connectivity in the coastal ocean with application to the Southern California Bight, *J. Geophys. Res.*, *114*, 1–21, doi:10.1029/2008JC005166.

Molemaker, M., J. McWilliams, and W. Dewar (2015), Submesoscale instability and generation of mesoscale anticyclones near a separation of the California Undercurrent, *J. Phys. Oceanogr.*, *45*, 613–629, doi:10.1175/JPO-D-13-0225.1.

Munk, W., L. Armi, K. Fischer, and F. Zachariasen (2000), Spirals on the sea, *Proc. R. Soc. Lond.*, *456*, 1217–1280, doi:10.1098/rspa.2000.0560.

Nagai, T., A. Tandon, and D. Rudnick (2006), Two-dimensional ageostrophic secondary circulations at ocean fronts due to vertical mixing and large-scale deformation, *J. Geophys. Res.*, *111*, doi:10.1029/2005JC002964.

Nam, S., and U. Send (2012), Resonant diurnal oscillations and mean alongshore flows driven by sea/land breeze forcing in the coastal Southern California Bight, *J. Phys. Oceanogr.*, *43*, 616–630, doi:10.1175/JPO-D-11-0148.1.

Nickols, K., B. Gaylord, and J. Largier (2012), The coastal boundary layer: predictable current structure decreases alongshore transport and alters scales of dispersal, *Marine Ecology Progress Series*, *464*, 17–34, doi:10.3354/meps09875.

Noble, M., B. Jones, P. Hamilton, J. Xu, G. Robertson, L. Rosenfeld, and J. Largier (2009), Cross-shelf transport into nearshore waters due to shoaling internal tides in San Pedro Bay, CA, *Continental Shelf Research*, *29*, 1768–1785, doi:10.1016/j.csr.2009.04.008.

Ohlmann, J., J. LaCasce, L. Washburn, A. Mariano, and B. Emery (2012), Relative dispersion observations and trajectory modeling in the Santa Barbara Channel, *J. Geophys. Res.*, *117*, C05,040, doi:10.1029/2011JC007810.

Ohlmann, J., M. Molemaker, B. Baschek, B. Holt, G. Marmorino, and G. Smith (2017), Drifter observations of submesoscale flow kinematics in the coastal ocean, *Geophys. Res. Lett.*, *44*, 330–337, doi:10.1002/2016GL071537.

Paris, C., J. Helgers, E. van Sebille, and A. Srinivasan (2013), Connectivity Modeling System: A probabilistic modeling tool for the multi-scale tracking of biotic and abiotic variability in the ocean, *Environmental Modelling and Software*, *42*, 47–54, doi:10.1016/j.envsoft.2012.12.006.

Poje, A., A. Haza, T. Ozgokmen, M. Magaldi, and Z. Garraffo (2010), Resolution dependent relative dispersion statistics in a hierarchy of ocean models, *Ocean Modelling*, *31*, 36–50, doi:10.1016/j.ocemod.2009.09.002.

Poje, A., T. Ozgokmen, B. Lipphardt, B. Haus, E. Ryan, A. Haza, G. Jacobs, A. Reniers, M. Olascoaga, G. Novelli, A. Griffa, F. Beron-Vera, S. Chen, E. Coelho, P. Hogan, A. Kirwan, H. Huntley, and A. Mariano (2014), Submesoscale dispersion in the vicinity of the Deepwater Horizon spill, *Proc. Natl. Acad. Sci. (USA)*, *111*, 12,693–12,698, doi:10.1073/pnas.1402452111.

Price, J., R. Weller, and R. Pinkel (1986), Diurnal Cycling: Observations and Models of the Upper Ocean Response to Diurnal Heating, Cooling, and Wind Mixing, *J. Geophys. Res.*, *91*, 8411–8427, doi:10.1029/JC091iC07p08411.

Renault, L., M. Molemaker, J. McWilliams, and A. Shchepetkin (2016), Modulation of Wind Work by Oceanic Current Interaction with the Atmosphere, *J. Phys. Oceanogr.*, *46*, 1685–1704, doi:10.1175/JPO-D-15-0232.1.

Renault, L., J. McWilliams, A. Jousse, C. Deutsch, H. Frenzel, F. Kessouri, and R. Chen (2019), The Physical Structure and Behavior of the California Current System, *J. Phys. Oceanogr.*, *submitted*.

Restrepo, J., S. Venkataraman, and C. Dawson (2014), Nearshore sticky waters, *Ocean Modelling*, *80*, 49–58, doi:10.1016/j.ocemod.2014.06.003.

Robinson, I. (1981), Tidal vorticity and residual circulation, *Deep-Sea Research*, *28*, 195–212, doi:10.1016/0198-0149(81)90062-5.

Romero, L., Y. Uchiyama, J. Ohlmamn, J. McWilliams, and D. Siegel (2013), Simulations of nearshore particle-pair dispersion in Southern California, *J. Phys. Oceanogr.*, *43*, 1862–1879, doi:10.1175/JPO-D-13-011.1.

Romero, L., D. Siegel, J. McWilliams, Y. Uchiyama, and C. Jones (2016), Characterizing storm water dispersion and dilution from small coastal streams, *In Prep.*, *J. Geophys. Res.*

Shakespeare, C., and J. Taylor (2013), A generalized mathematical model of geostrophic adjustment and frontogenesis: uniform potential vorticity, *J. Fluid Mech.*, *736*, 366 – 413, doi:10.1017/jfm.2013.526.

Shchepetkin, A., and J. McWilliams (2005), The Regional Oceanic Modeling System (ROMS): A split-explicit, free-surface, topography-following-coordinate ocean model, *Ocean Modell.*, *9*, 347–404, doi:10.1016/j.ocemod.2004.08.002.

Shchepetkin, A., and J. O'Brien (1996), A Physically Consistent Formulation of Lateral Friction in Shallow-Water Equation Ocean Models, *Mon. Wea. Rev.*, *124*, 1285–1300, doi:10.1175/1520-0493(1996)124<1285:APCFOL>2.0.CO;2.

Shcherbina, A., E. D'Asaro, C. Lee, J. Klymak, M. Molemaker, and J. McWilliams (2013), Statistics of vertical vorticity, divergence, and strain in a developed submesoscale turbulence field, *Geophys. Res. Lett.*, *40*, 4706 – 4711, doi:10.1002/grl.50919.

Shroyer, E., J. Moum, and J. Nash (2010), Vertical heat flux and lateral mass transport in nonlinear internal waves, *Geophys. Res. Lett.*, *37*, 1–5, doi:10.1029/2010GL042715.

Siegel, D., B. Kinlan, B. Gaylord, and S. Gaines (2003), Lagrangian descriptions of marine larval dispersion, *Mar. Ecol. Prog. Ser.*, *260*, 83–96, doi:10.3354/meps260083.

Simpson, J. (1981), The shelf-sea fronts: implications of their existence and behavior, *Phil. Trans. R. Soc. Lond.*, *302*, 531–546, doi:10.1038/250404a0.

Simpson, J., and J. Hunter (1974), Fronts in the Irish Sea, *Nature Communications*, *250*, 404–406, doi:10.1038/250404a0.

Solomon, T., E. Weeks, and H. Swinney (1993), Observation of Anomalous Diffusion and Levy Flights in a Two-Dimensional Rotating Flow, *Physical Review Letters*, *71*, 3975–3978, doi:10.1103/PhysRevLett.71.3975.

Spydell, M. (2016), The suppression of surfzone cross-shore mixing by alongshore currents, *Geophys. Res. Lett.*, *43*, 9781–9790, doi:10.1002/2016GL070626.

Srinivasan, K., J. McWilliams, and L. Renault (2017), Topographic and Mixed Layer Submesoscale Currents in the Near-Surface Southwestern Tropical Pacific, *J. Phys. Oceanogr.*, *47*, 1221 – 1242, doi:10.1175/JPO-D-16-0216.1.

Suanda, S., F. Feddersen, M. Spydell, and N. Kumar (2018), The Effect of Barotropic and Baroclinic Tides on Three-Dimensional Coastal Dispersion, *Geophys. Res. Lett.*, *45*, doi:10.1029/2018GL079884.

Sullivan, P., and J. McWilliams (2017), Frontogenesis and frontal arrest for a dense filament in the oceanic surface boundary layer, *J. Fluid Mech.*, *837*, 341 – 380, doi:10.1017/jfm.2017.833.

Thomas, L., A. Tandon, and A. Mahadevan (2008), Submesoscale Processes and Dynamics, *Ocean Modeling in an Eddying Regime, Geophysical Monograph Series*, *177*, 17–38, doi:10.1029/177GM04.

Tilburg, C. (2003), Across-shelf transport on a continental shelf: Do across-shelf winds matter?, *J. Phys. Oceanogr.*, *33*, 2675–2688, doi:10.1175/1520-0485(2003)033<2675:ATOACS>2.0.CO;2.

Tomczak, M. (1988), Island wakes in deep and shallow water, *J. Geophys. Res.*, *93*, 5153–5154, doi:10.1029/JC093iC05p05153.

Uchiyama, Y., J. McWilliams, and A. Shchepetkin (2010), Wave-current interaction in an oceanic circulation model with a vortex-force formalism: Application to the surf zone, *Oceanogr. Meteorol.*, *34*, 16–35, doi:10.1016/j.ocemod.2010.04.002.

Uchiyama, Y., E. Idica, J. McWilliams, and K. Stolzenbach (2014), Wastewater effluent dispersal in Southern California Bays, *Cont. Shelf Res.*, *76*, 36–52, doi:10.1016/j.csr.2014.01.002.

Ullman, D., A. Dale, D. Hebert, and J. Barth (2003), The front on the Northern Flank of Georges Bank in spring: 2. Cross-frontal fluxes and mixing, *J. Geophys. Res.*, *108*, 1–14, doi:10.1029/2002JC001328.

Wenegrat, J., and M. McPhaden (2016a), Wind, waves and fronts: Frictional effects in a generalized Ekman model, *J. Phys. Oceanogr.*, *46*, 371–394, doi:10.1175/JPO-D-15-0162.1.

Wenegrat, J., and M. McPhaden (2016b), A simple analytical model of the diurnal Ekman layer. In Review, *J. Phys. Oceanogr.*, *46*, 2877–2894, doi:10.1175/JPO-D-16-0031.1n.

Wenegrat, J., and L. Thomas (2017), Ekman transport in balanced currents with curvature, *J. Phys. Oceanogr.*, *47*, 1189 – 1203, doi:10.1175/JPO-D-16-0239.1.

Wiel, B. V. D., A. Moene, G. Steeneveld, P. Baas, F. Bosveld, and A. Holtslag (2010), A conceptual view on inertial oscillations and nocturnal low-level jets, *J. Atmos. Sci.*, *67*, 2679 – 2689, doi:10.1175/2010JAS3289.1.

Wolanski, E., and M. Kingsford (2014), Oceanographic and behavioural assumptions in models of the fate of coral and coral reef fish larvae, *J. R. Soc. Interface*, *11*, doi:10.1098/rsif.2014.0209.

Wolanski, E., and S. Spangol (2000), Sticky Waters in the Great Barrier Reef, *Estuar. Coast. Shelf Sci.*, *50*, 27–32, doi:10.1006/ecss.1999.0528.

Wolanski, E., J. Imberger, and M. Heron (1984), Island wakes in shallow coastal waters, *J. Geophys. Res.*, *89*, 10,533–10,569, doi:10.1029/JC089iC06p10553.

Wood, S., C. Paris, A. Ridgewell, and E. Hendy (2014), Modelling dispersal and connectivity of broadcast spawning corals at the global scale, *Global Ecol. Biogeogr.*, *23*, 1–11, doi:10.1111/geb.12101.

Xue, H., L. Incze, D. Xu, N. Wolff, and N. Pettigrew (2008), Connectivity of lobster populations in the coastal Gulf of Maine Part I: Circulation and larval transport potential, *Ecological Modelling*, *210*, 193–211, doi:10.1016/j.ecolmodel.2007.07.024.

Zhang, W., and G. Gawarkiewicz (2015), Length scale of the finite-amplitude meanders of shelf-break fronts, *J. Phys. Oceanogr.*, *45*, 2598–2620, doi:10.1175/JPO-D-14-0249.1.

Zhang, Y., and Z. Tan (2002), The diurnal wind variation in a variable eddy viscosity semi-geostrophic Ekman boundary-layer model: Analytical study, *Meteorology and Atmospheric Physics*, *81*, 207–217, doi:10.1007/s00703-001-0542-6.